London Centre for Nanotechnology
Department of Mechanical Engineering

Time-Dependent Mechanics of Living Cells

Emadaldin Moeendarbary

Dissertation submitted for the degree of

Doctor of Philosophy

University College London

September 2012

Declaration

I, Emadaldin Moeendarbary confirm that the work presented in this thesis is my own. Where information has been derived from other sources, I confirm that this has been indicated in the thesis.

پروردگارا، سپاس گزارم که به من نیروی اندیشیدن دادی.

تقدیم به:

پدر و مادرم که همواره مرا در دانش آموختن یاری کرده اند،

و

همسرم ژانت که همراه و پشتیبان من در به پایان رسانیدن این کار بود.

Acknowledgements

I am sincerely grateful to my main supervisor Dr. Guillaume Charras and second advisor Dr. Eleanor Stride for their kind guidance and continuous support over the past three years. I would particularly like to thank Dr. Charras for offering me this project, welcoming me to carry out this research in his lab and introducing me to biological techniques. I would also like to extend my grateful appreciation to Prof. L. Mahadevan for providing great insights on poroelasticity and his valuable inputs to this work.

I appreciate very much the helps of Dr. Marco Fritzsche, Dr. Andrew Harris, Dr. Carl Leung, and Dr. Richard Thorogate from London Centre for Nanotechnology. I gratefully acknowledge support of Prof. Nicos Ladommatos and Dr. William Suen from Department of Mechanical Engineering. I am thankful to our collaborators Prof. Adrian Thrasher and Dr. Dale Moulding from Institute of Child Health.

I would like to acknowledge the financial support from the Engineering and Physical Sciences Research Council (EPSRC) through the prestigious Dorothy Hodgkins Postgraduate Award.

Thank you my friends, Marco, Alireza, Andrew, Cesar and Miia. You are always so helpful and encouraging.

Thank you, Judy and Guy Whitmarsh for your kind supports.

And many many thanks to my teachers and professors from elementary, junior and high school to university, who encouraged me to continuously learn and provided me with the foundations for my academic career.

Abstract

Cells sense and generate both internal and external forces. They resist and transmit these forces to the cell interior or to other cells. Moreover a variety of cellular responses are excited and influenced by transducing mechanical stimulations into chemical signals that lead to changes in cellular behaviour. The cytoplasm represents the largest part of the cell by volume and hence its rheology sets the maximum rate at which any cellular shape change can occur.

To date, the cytoplasm has generally been modelled as a single-phase viscoelastic material; however, recent experimental evidence suggests that its rheology can be described more effectively using a poroelastic formulation in which the cytoplasm is considered to be a biphasic system constituted of a porous elastic solid meshwork (cytoskeleton, organelles, macromolecules) bathing in an interstitial fluid (cytosol). In this framework, a single parameter, the poroelastic diffusion constant D_p, sets cellular rheology scaling as $D_p \sim E\xi^2 / \mu$ with E the elastic modulus, ξ the hydraulic pore size, and μ the cytosolic viscosity. Though this poroelastic view of the cell is a conceptually attractive model, direct supporting evidence has been lacking. In this work, such evidence is presented and the concept of a poroelastic cell is validated to explain cellular rheology at physiologically relevant time-scales.

In this work, the functional form of stress relaxation in response to rapid application of a localised force by atomic force microscopy microindentation is examined in detail and it is shown that at short time-scales cellular relaxations are poroelastic. Then, D_p is measured in cells by fitting experimental stress relaxation curves to the theoretical model.

Next, using indentation tests in conjunction with osmotic perturbations, the validity of the predicted scaling of D_p with pore size is qualitatively verified. Using chemical and genetic perturbations, it is shown that cytoplasmic rheology depends strongly on the integrity of the actin cytoskeleton but not on microtubules or intermediate filaments. Finally, comparison of scaling of viscoelastic and poroelastic models suggests that short-time scale viscoelasticity might be due to water redistribution within the cytoplasm and a simple scaling relating cytoplasmic viscosity to cellular microstructure is provided.

Contents

List of Figures

List of tables

Supplementary video

Effects of osmotic shock on the movement of microinjected PEG-passivated quantum dots in HeLa cell.

Movement of PEG-passivated quantum dots microinjected in a HeLa cell in isoosmotic conditions (left) and in hyperosmotic conditions (right). Both movies are 120 frames long totalling 18 s and are single confocal sections. In isoosmotic conditions, quantum dots move freely (left); whereas in hyperosmotic conditions, quantum dots are immobile because they are trapped within the cytoplasmic mesh (right). Scale bars = 5 μm.

Chapter 1

Introduction

Equation Chapter (Next) Section 1

1.1 A Microscopic view: biological structure of cell

Living cells, the elementary units of life, all carry out similar basic functions and they display a common architecture despite their various shapes, sizes and internal complexities (Figure 1-1). In addition to basic functions such as proliferation, protein synthesis, molecule transport and energy conversion, cells may also perform more specialised roles that pertain to the organs that they are part of. Prokaryotic cells, such as bacteria, lack membrane-bounded nuclei while eukaryotic cells contain membrane-bounded compartments (including nuclei and other organelles) that perform specific metabolic activities and energy conversion. Plant and animal cells are eukaryotes and are typically larger (~ 5 to 100 μm) and more complex than prokaryotic cells (~ 1 to 10 μm). The internal and external environments of the eukaryotic cells are separated by a plasma membrane which is a selectively-permeable barrier consisting of a lipid bilayer with

embedded proteins. The work described in this thesis is focused on the animal cell whose fluid-like plasma membrane cannot alone adopt complex cellular morphologies [1, 2]). The material inside the cell membrane, excluding the nucleus, is generally referred to as the cytoplasm which consists of a liquid phase, the cytosol (water, salts, small proteins), and a solid phase (cytoskeleton, organelles, ribosomes, etc). A general diagram of animal cell organisation is given in Figure 1-1B.

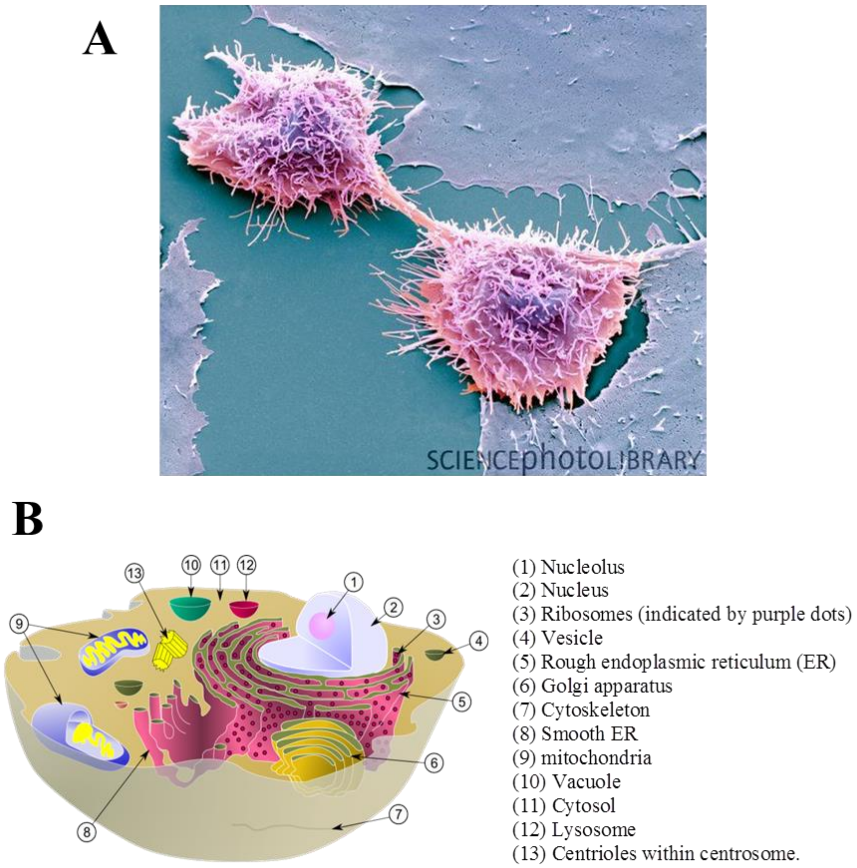

Figure 1-1 Living cells

(A) Coloured scanning electron micrograph (SEM) of a HeLa cancer cell undergoing cell division. Source: http://www.sciencephoto.com/media/137830/enlarge. (B) Schematic showing the generic cytoplasm organisation and nucleus of an animal cell. The main cellular structures and organelles are listed in the right panel. Source: http://en.wikipedia.org/wiki/File:Biological_cell.svg.

The cellular skeleton (cytoskeleton) is a complex network of three major types of polymeric fibre of varying size and rigidity extending throughout the cytoplasm. It consists of cable-like actin filaments with diameters of ~ 7 nm, rope-like intermediate filaments with diameters of ~ 10 nm and pipe-like microtubules with diameters of ~ 20 nm [1-3] (see Figure 1-2). The cytoskeleton is responsible for maintenance of cell shape, cell migration, resistance to externally applied mechanical forces, and cell division. Furthermore it controls and facilitates the transport of intracellular particles and organization of cell contents.

Actin filaments are known to be the most important polymer network for the mechanics of the cytoskeleton. They are organized in a variety of structures such as networks of filaments within the cytoplasm, the cortex under the plasma membrane, the lamellipodia at the cell edges, the filopodia and contractile stress fibres. The subunit of an actin filament (F-actin) is a globular actin protein (G-actin) which accounts for about 5-10 percent of the total cellular protein content [4, 5]. A typical actin filament has a longitudinal elasticity of ~ 2 GPa and a persistence length of ~ 15 μm which is larger than its typical contour length of ~ 2 μm. Actin filaments have a distinct polarity originating from the structural asymmetry of G-actin and filaments exhibit a faster polymerisation rate at one end (plus barbed-end) compared to the other end (minus pointed-end).

αβ tubulin heterodimers organize into long hollow cylinders to form microtubules which are the second major constituent of the cytoskeleton [4]. Similar to F-actin, microtubules are polar filaments because of the structural arrangement of their subunits [2]. Microtubules are straight and rigid with turnovers on the order of minutes [6], and they play a key role in chromosomal distribution during cell division. They typically radiate randomly from the centrosome (which is a microtubule organizing centre (MTOC) near the nucleus) towards the periphery of the cell with their (–) ends proximal to the MTOC and their (+) ends directed away from the MTOC. The tubular structure of microtubules gives rise to a higher bending stiffness than actin filaments despite their similar effective longitudinal Young's moduli [2]. The persistence length of microtubules is ~ 5 mm which

is ~ 1000 fold larger than their typical length ~ 5 μm and the typical length of a cell: ~ 50 μm. Microtubules are known to be the most significant compressive-load bearing elements of the cytoskeleton [7].

As the most abundant cytoskeletal filaments, intermediate filaments are located both inside the cytoplasm and the nucleus and form a large and more diverse family of highly α-helical proteins. Unlike actin filaments and microtubules subunit proteins, these α-helical proteins integrate into more diverse sequences with greatly varying molecular weights to form different types of intermediate filaments such as: keratins that are abundant in epithelial cells, lamins that are involved in the formation of a structure called the lamina which is located underneath nuclear membrane and helps stabilise the nuclear envelope, and vimentin filaments that are expressed mainly in mesenchymal cells [3]. Intermediate filaments, typically have a diameter of ~ 10 nm which is in between the diameter of actin filaments (7 nm) and microtubules (25 nm).They have a persistence length of ~ 1 μm that is smaller /comparable to their length giving them more flexibility. Intermediate filaments extend out from around the nucleus throughout the cytoplasm and it is thought that they are mechanically incorporated with other parts of cytoskeleton through specialised crosslinking proteins to reinforce the integrity of the cell [8]. Intermediate filaments are more stable than actin filaments and microtubules (for instance keratin filaments have a turnover of ~ 30 min [9]) and play a major role in cell-cell attachments in epithelial tissue [10].

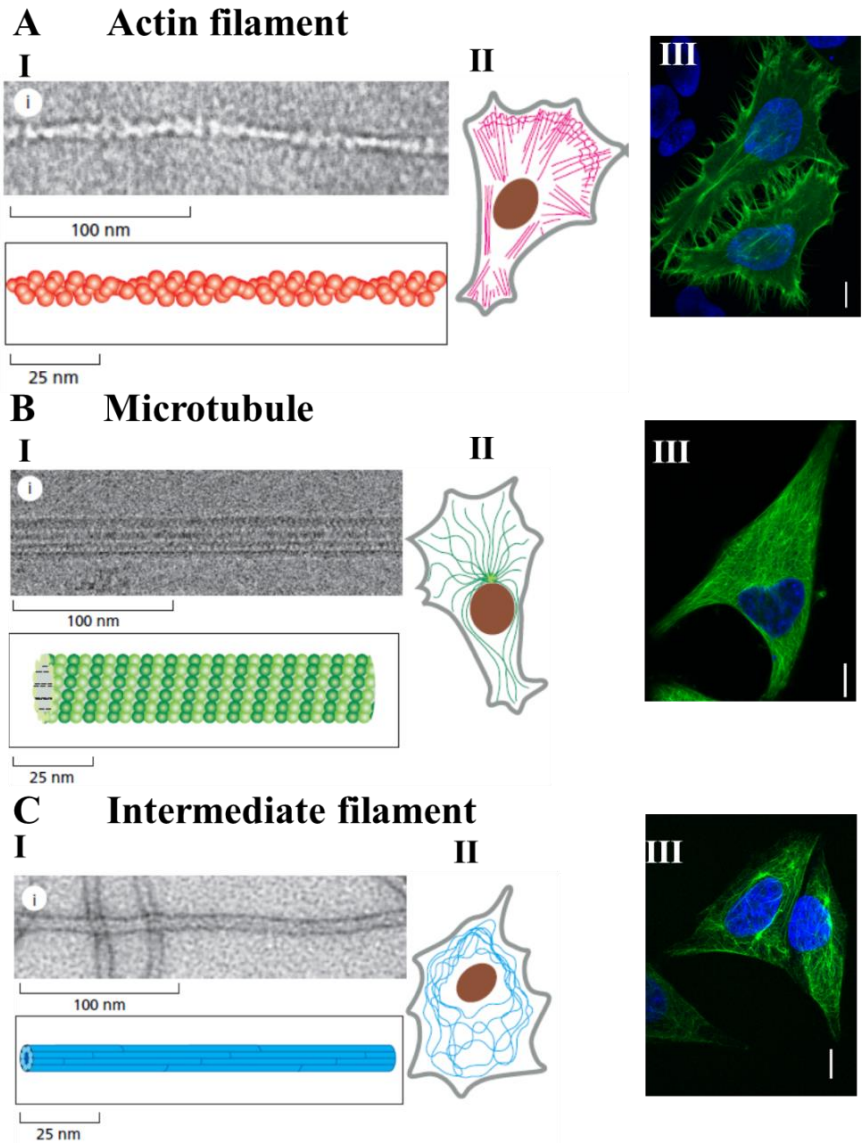

Figure 1-2 The three major types of filaments that constitute the cytoskeleton.

(A,B,C -I): The electron micrographs and lattice structure of filaments: source:[3] (A,B,C –II): Schematic of spatial distribution of cytoskeleton filaments. (A,B,C –III): Distribution of cytoskeletal constituents in live HeLa cells. All images are maximum projections of confocal stacks. Green indicates the localisation of the GFP-tagged construct. The nucleus is shown in blue in all images. (A-III) F-actin was enriched in cell protrusions but was also present in the cell body. (B-III) GFP-α-tubulin was homogenously localised in the cell body. A-III & B-III were acquired by L. Valon. (C-III) Intermediate filaments (keratin 18) were homogenously distributed in the cell body. Scale bars = 10 μm.

As briefly described in the previous paragraphs, each cytoskeletal filament is constructed from specific protein subunits. There exists a continual flux of constituent subunits onto/from both ends of filament which results in polymerisation/depolymerisation. In the steady state, polymerisation and depolymerisation are balanced and as a result the filament maintains a given length, a phenomenon known as treadmilling (see Figure 1-3C-III for actin filament). Under normal conditions, the rate of this polymerisation/depolymerisation (turnover) is different for each of the three major types of cytoskeletal filament. For instance, intermediate filaments have a much slower rate of turnover (~ tens of minutes) than actin filaments (~ tens of seconds). Many active features in the cell such as force generation are in part due to these energy consuming turnover processes. For instance, actin polymerization [11-13] constructs the leading edge of the cell, a two dimensional sheet-like structure called the lamellipodium, that drives cell protrusion (see Figure 1-1 and Figure 1-3).

The above three major filament types are the key parts of the cytoskeleton. To build the cytoskeletal network architecture and define the mechanics of the cell, these primary filaments interact with one another, cross-link and bind with themselves and connect to other parts of cytoplasm (plasma/nuclear membrane, organelles, etc) through various types of linking proteins and molecular motors. Motor proteins convert the energy released by ATP hydrolysis into mechanical work to dynamically interact with the cytoskeleton and to facilitate many different cellular functions such as force generation and locomotion, cell division and intracellular transport. For instance during cell movement, myosin II motor proteins move along cytoskeletal filaments and generate contractile forces necessary for contraction of the cell rear (see Figure 1-3D and Figure 1-4). Crosslinking proteins organize cytoskeletal filaments into entangled and bundled complex scaffolds. Hence, they help determine the network architecture leading to different cellular mechanical functions [14]. For example, the crosslinking protein α-actinin is one of the most abundant acting binding proteins and it crosslinks actin filaments into bundles to provide contractility in cytoskeletal assemblies such as stress

fibres [15] and the contractile ring [16] (Figure 1-4). Other crosslinkers, such as filamin, organise actin filaments into a crosslinked gel-like network (Figure 1-4).

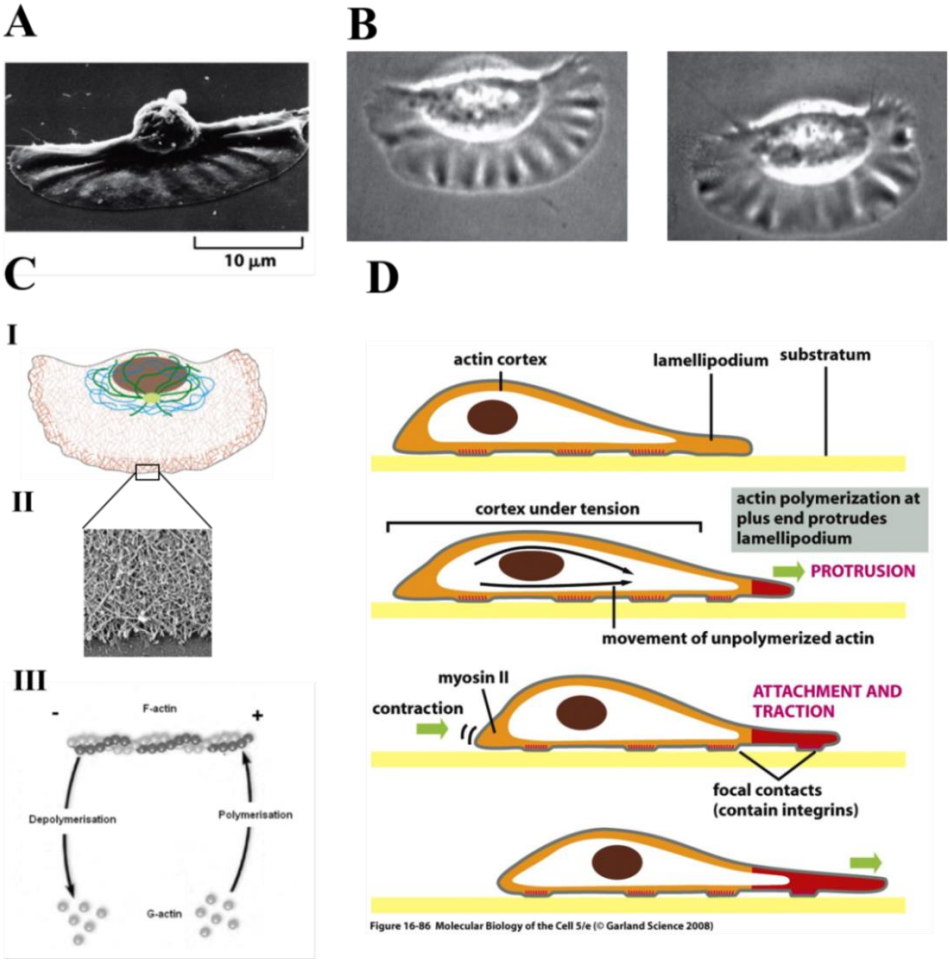

Figure 1-3 Generation of force in the actin-rich cortex moves a cell.

(A) Scanning electron microscope image of a fish keratocyte. (B) Phase-contrast image of the keratocyte moving downward with a speed of ~ 15 µm.s^{-1}. (C-I) Distribution of cytoskeletal filaments with actin fillaments in brown, microtubules in green and intermediate filaments in blue. (C-II) Electron micrograph of the F-actin network in the lamellipodium. (C-III) Treadmilling: polymerisation/depolymerisation of actin filaments by reversible addition of actin subunits to the free ends of the filament. One end of the filament elongates (plus end) while the other end shrinks (minus end). At steady state, addition and loss are balanced. (D) Schematic diagram of how cells move forward. Actin polymerisation at the leading edge of the cell extends a protrusion in the direction of movement. The leading edge adheres to the substrate in front and adhesions at the rear of the cell are detached. The contractile forces generated by the acto-myosin at the cell rear push the whole cell body forward. Source:[3].

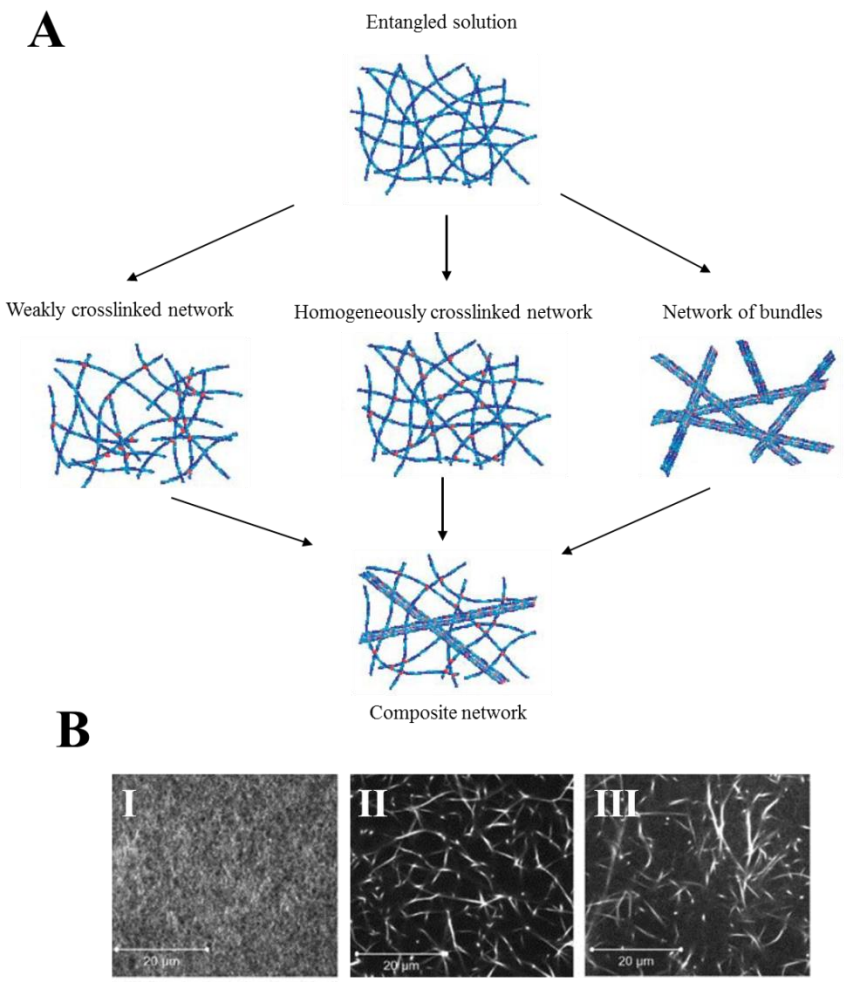

Figure 1-4 Binding proteins induce structural phase transitions to polymerised solution of purified filaments. (A) Addition of binding proteins with different properties such as type, organisation and concentration results in the formation networks with different microstructural organisations. Adapted from [17]. (B) Effects of crosslinkers and myosin II thick filaments on the network topology of actin filaments. (B-I) Entangled network of purified actin filaments. (B-II) Addition of α-actinin crosslinker proteins changes the shape and architecture of the actin filament network. (C) Addition of myosin II ,motor proteins leads to further contraction and rearrangement of the crosslinked F-actin network. Source: [18].

1.2 The role of mechanics in cell function

Living cells sense their environment and generate internal and external forces [19]. They resist and transmit these forces to the cell interior or other cells through chemical and physical signals. Complex sensory machineries located on different cellular sites such as primary cilia, stretch-gated ion channels and focal adhesions are responsible for sensing mechanical stimulations (arising from application of different types of forces such as tensional, compressional, pressure and shear forces) generated internally or applied externally on different parts of the cell and eventually transducing these cues into biochemical signals (see Figure 1-5A) [20, 21]. More fascinatingly, in a closed-loop feedback manner these mechanosensed biochemical signals trigger energy-consuming chemical processes relying on ATP hydrolysis that cells employ to modify their own behaviour and generate forces to respond to and resist the initial mechanical cues.

Mechanotransductory processes greatly influence and control a variety of cellular responses that lead to changes in cellular behaviour and function such as changes in cell morphology, lineage and fate [22, 23]. For example, in the musculoskeletal system, actin and myosin molecular motors produce active contraction in muscle cells in response to external electrical stimuli such as nerve influxes. Inner hair cells transduce the fluid oscillation generated in the cochlea by sound waves into electrical signals that are transmitted to the brain. Vascular endothelial cells bear hemodynamic forces, such as blood flow shear stress and pressure, and convert these applied stresses into intracellular signals that influence cellular functions such as proliferation, migration, permeability, and gene expression [24]. More interestingly, fluid shear stresses can modulate endothelial structure and function (see Figure 1-5B). Indeed endothelial cells, through rearrangement of their cytoskeletal structures and active remodelling processes, change their shape and align themselves with the direction of the flow to control the magnitude of shear forces they are exposed to [24]. One outstanding challenge in cell biology is to understand how

mechanical cues can be transduced into biochemical cues and how biochemical changes in the cell can give rise to changes in cellular mechanics or the forces applied by cells.

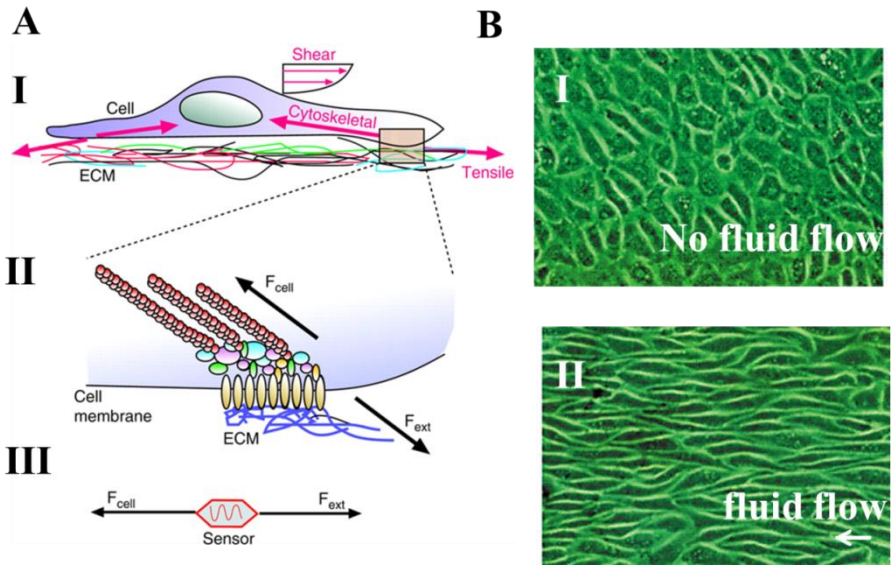

Figure 1-5 Cells sense and respond to application of forces.

(A-I) Application of different types of forces on cell such as shear forces induced by fluid flow over the cell, tensile forces arising from the extracellular matrix (ECM) and internal compressional or tensional forces induced and borne by the cellular cytoskeleton. (A-II) Diagram of a mechanosensor at the focal adhesions. At the focal adhesion site, the internal cytoskeletal forces are balanced by external forces distributed on the ECM (blue). On the external side of the cell membrane, ECM is attached to focal adhesions (multicolored array of proteins) through integrins (brown). On the internal side of the cell, membrane actin microfilaments (red) are anchored into focal adhesions. (III) The internal and external forces are passed through the mechanosensory site where forces can be sensed, controlled and regulated in a closed-loop feedback. Source: [20] (B) Endothelial cell morphology transformed by longterm exposure to fluid shear stress. Increasing the level of shear stress from 0 to > 1.5 Pa causes alignment of bovine aortic endothelial cells (shown under static culture conditions in I) in the direction of fluid flow after 24 hours (shown in II).Source: [25].

Entanglement (physical) and crosslinking (biochemical) of filamentous polymer networks inside cells maintain cell shape and govern cellular mechanical properties such as elasticity. Molecular motors and crosslinkers contract the cytoskeletal polymer network

and induce pre-stresses. Active mechanical forces generated from chemical reactions (such as active polymerisation of filaments or molecular motors) enforce morphogenetic changes such as cell rounding, cytokinesis, cell spreading, or cell movement. During these gross morphogenetic changes the cytoskeleton provides the force for morphogenesis but the maximal rate at which shape change can occur is dictated by the rate at which the whole cell can be deformed. Hence, the dynamic mechanical properties (rheology) of cytoplasm, which are poorly understood and are the main topic of this work, play a major role in setting the rate at which any morphogenetic event can occur. Furthermore, cells detect, react, and adapt to external mechanical stresses by regulation of microscopic processes that changes their mechanics. However, in the absence of an in depth understanding of cell rheology, the transduction of external stresses into intracellular mechanical changes is poorly understood, making the identification of the physical parameters that are detected biochemically largely speculative.

Although the correlation between the mechanical properties of tissues and diseases has been recognized quite widely for a long time, the connection between the mechanics of living cells (at single cell level) and disease is poorly understood. Indeed, the cell phenotype in health or disease can be affected by the rheology of the cell. One clinical example suggests that changes in cell rheology can have consequences for the health of patients: some patients with a low neutrophil count exhibit a constitutively active mutation in the Wiskott Aldrich syndrome protein (CA-WASp) that results in over-activation of actin polymerisation through dysregulated activation of the Arp2/3 complex, leading to delays in several stages of mitosis [26, 27]. This overabundance of cytoplasmic F-actin increases cellular apparent viscosity resulting in delays in all phases of mitosis and causing kinetic defects in mitosis (Moulding et al, Blood, 2012). Further to this example, there are other reports that identified different mechanical properties for cancerous cells compared to those of normal cells [28-31] which illustrate the importance of studying cell rheology. The ultimate goal is to combine theoretical, experimental and

computational approaches to construct models for a realistic description of the various types of cellular mechanical behaviours based on their microscopic cytoskeletal arrangement, something necessary to enable a true physical understanding of the stress fields present and generated in tissues and developing embryos during physiological functions.

1.3 Experimental techniques for measuring cellular mechanical properties

Depending on the length scale of the cellular structure under investigation and the required spatial and temporal resolution, many experimental techniques have been utilized to measure the mechanical properties of the different cellular components. In general, most methods measure the static/dynamic response of the cellular structure to the application of controlled forces or deformations. Other techniques track the motion of endogenous or embedded particles of various sizes to study the rheology of the cell. The important point is that due to the heterogeneity and complexity of the cell and the cytoskeleton, the submicrometre-scale measurement techniques can lead to considerably different evaluations of mechanical properties compared to bulk (several micrometre scale) measurement techniques. One of the main challenges is to find a universal framework under which the measured macroscopic properties can be interpreted to obtain realistic information about the dynamics of the microstructure of the cell or vice versa, i.e. to estimate the bulk rheological properties from the measured microscopic properties [32].

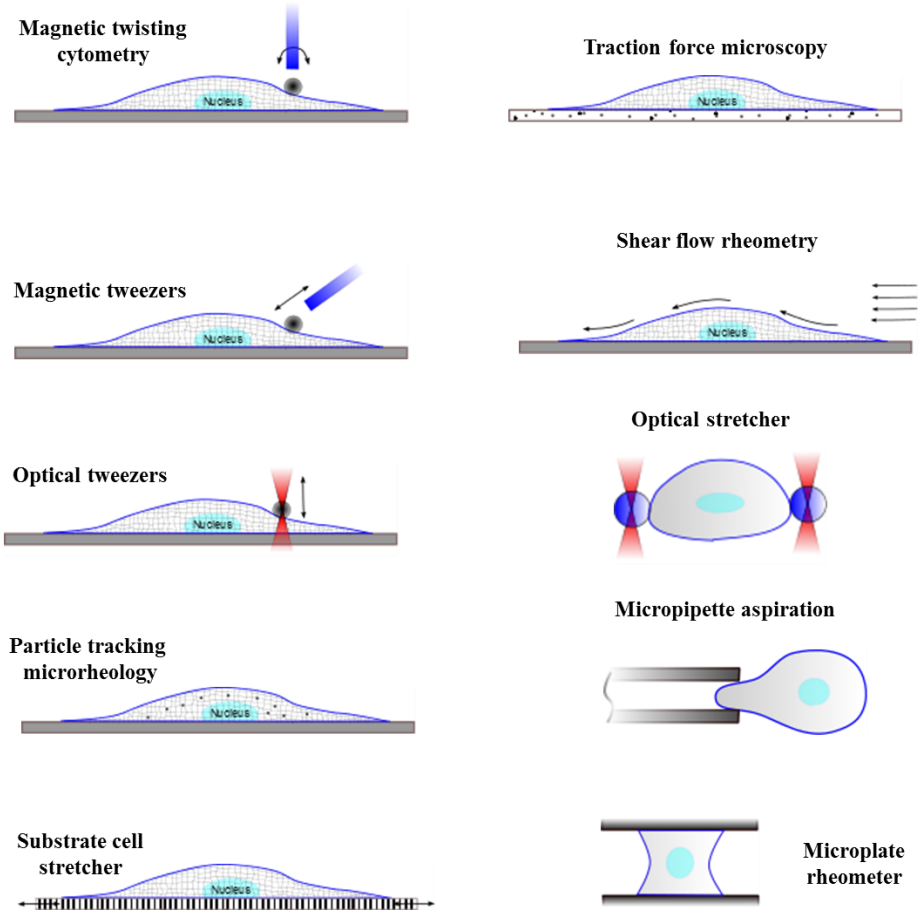

Figure 1-6 Common experimental techniques for measurement of cell rheology.

Several experimental methods such as magnetic twisting cytometry [33, 34], magnetic tweezers [35], optical tweezers [36], substrate cell stretchers [37, 38], shear flow rheometry [39, 40] (see Figure 1-6) and atomic force microscopy (AFM) (see the following paragraph and Figure 1-7) have been utilized to perturb small regions of the cell or deform an entire cell to investigate cell rheology. An alternative technique is the use of passive methods, such as traction force microscopy that involves quantification of cellular traction forces using different detection mechanisms such as micropillar arrays [41] or substrate-embedded beads [42]. One more recently applied technique is particle-

tracking microrheology that tracks motion of embedded or attached tracer particles present within the system to extract cellular mechanical properties [43]. Depending on the cell type, the experimental condition and the probing technique diverse ranges of cellular rheological properties have been reported and various mechanical models (some of which are described in the following sections) were applied to interpret quantitative measurements of cell mechanical properties. Further to the need for significant improvement in mechanical models, the experimental methods also required to be improved to measure local/global mechanical properties of single cells more accurately. Some of these important features include: the ability to impose/measure deformations and forces on micro and nano scales, perform dynamic experiments, integrate with other experimental tools such as confocal microscopy and maintain cell viability for a sufficient period of time [4, 44-46].

1.3.1 Atomic force microscopy

In my studies, I utilized the Atomic force microscope (AFM), a very high resolution form of scanning probe microscope that was invented in 1986 [47] and has emerged rapidly as a versatile tool to study biological samples over the past two decades [48]. This allowed me to acquire topographic images of cells (Figure 1-7D), probe rigidity [49] and characterisation of viscoelastic properties of different cell lines (Moulding et al, Blood, 2012) and extracellular gel matrices (Calvo et al, Nature Cell Biology, under review). Topographic AFM measurements involve a tip connected to a micro-fabricated cantilever being scanned over the surface of a sample in a series of horizontal sweeps (see Figure 1-7A). A laser beam from a solid state diode is reflected off the back of the cantilever and collected by photodiodes. Perturbations in the movement of the tip due to surface topography result in changes in bending of the cantilever and consequently of the reflection path of the laser beam which is sensed via photodiodes. A piezo-electric ceramic in a feedback loop is used to move the cantilever up and down to maintain a constant bending of the cantilever. In contact mode, the tip is touching the surface while

sweeping across it. As the deflection of the cantilever is kept constant, the surface topography is reconstructed in 3D from the piezo movement and the planar trajectory of the cantilever (see Figure 1-7A). The cantilever vertical and lateral deflections provide information about the sample height changes and can map the surface distribution of different chemical functionalities [50].

In addition to high resolution imaging of biological structures, AFM has been used extensively to assess the mechanical properties of biological materials such as elasticity and viscoelasticity [51-54]. As will be explained later in Chapter 3.7, AFM indentation was employed in this thesis to characterise the rheological properties of cytoplasm. Furthermore AFM can be integrated with other techniques such as defocusing microscopy to investigate stress propagation inside cells and this idea will be described in the last chapter.

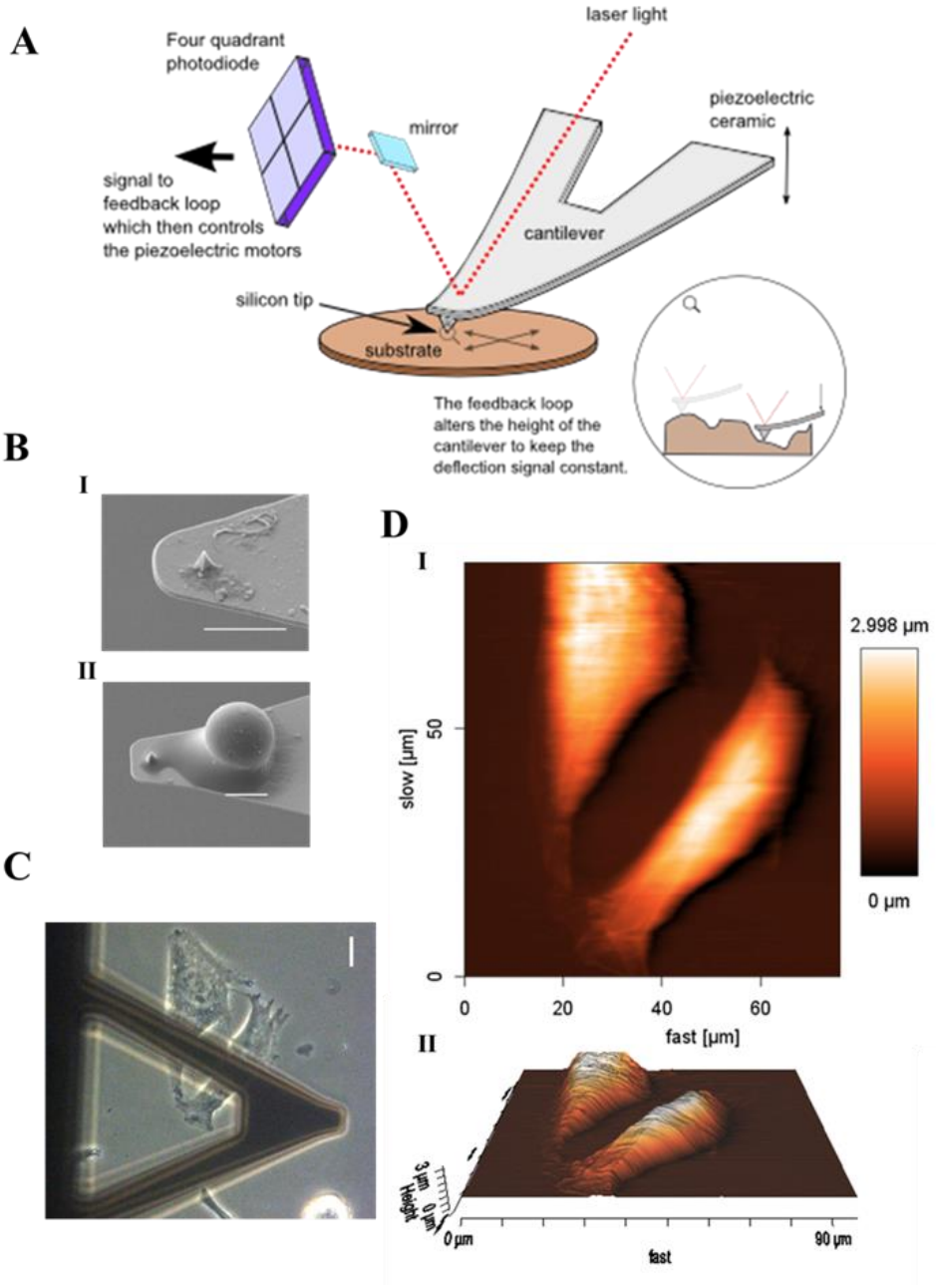

Figure 1-7 Atomic force microscopy imaging of the cell surface.

(A) Schematic diagram of an AFM cantilever tip scanning a surface. Vertical cantilever motion is controlled by a piezoelectric ceramic through a feedback loop. Bending of the cantilever alters the laser beam reflection path which is sensed by photodiodes. (B-I,II) SEM images of AFM cantilevers with pyramidal (I) and glued spherical (I) tips. In (II) a glass microbead was glued onto the cantilever. (C) Phase contrast image of an AFM cantilever probing HeLa cells cultured on a glass coverslip. (D-I) Contact mode image of HeLa cells shown in (C), imaged in cell culture medium with a pyramid tipped cantilever. (D-II) Three dimensional reconstruction of cell topography. Scale bars = 10 µm.

1.4 Cell mechanics and rheology

1.4.1 The origin of cellular mechanical and rheological properties

As a first step to studying cellular mechanical and rheological properties, the cell can be simply considered as a conventional engineering material [55]. Simple conventional materials exhibit very simple frequency-dependent responses: for normal solids the shear modulus is independent of frequency and for liquids it is simply proportional to frequency. However, materials (including cells) with more complex hierarchical structures and a high degree of heterogeneity can exhibit a variety of complex responses depending on strength, frequency and spatial application of deformations and forces. Being such a complex material, the cell displays viscoelasticity, i.e. it behaves like an elastic solid over short time scales with a finite shear modulus whereas it acts as a viscous liquid at long time scales [56, 57]. In intermediate regimes, both the storage and shear moduli govern the mechanical response of the cell. At different hierarchical levels, individual microstructural elements of the cytoskeleton are perturbed by application of force and deformed at microscopic scales to accommodate macroscopic deformations. Furthermore, processes such as continuous turnover of cytoskeletal fibres, association/dissociation of crosslinkers and activity of molecular motors mean that the cell is an active biological material [56] that exhibits astonishing rheological behaviours by coupling active and passive biochemical and mechanical processes. Indeed, time-dependent measurements of cellular properties reveal a spectrum of relaxation times which are strongly influenced by the size, stability, geometry, and flexibility of cross-linkers, active motions, and changes in filament structure due to turnover [45].

1.4.2 Cell as a continuum media

Experiments on cells have shown that the cytoskeleton is the main determinant of cellular mechanical properties. Hence, much effort has concentrated on describing cytoskeletal rheology. As will be described in the following, wide ranges of top-down and bottom-up

theoretical models have been proposed to describe the rheology of the cytoskeleton and the cellular environment. A robust model is one that can incorporate the minimum necessary information about internal structure, spatial granularity, heterogeneity and the active features unique to cells to predict long-wavelength and long-timescale redistribution of stress [46, 56]. However the search for such a comprehensive model is still ongoing. Indeed, even a description of the cell as a multi-layered composite (such as an elastic membrane tightly bound to the subcortical actin gel, a more granular gel-like inner layer, a more fluid layer in the cell interior and a stiff nucleus) without incorporating the internal complexity of each layer and active processes still remains a very complex system to investigate. Indeed, experimentally measured rheological properties are highly dependent on the size of the probe as well as its connectivity and interaction with the cellular structures [58]. For example, during microindentation experiments with a micron-sized bead, the induced deformations on the cell are significantly larger than the mesh size of the cytoskeletal network such that continuum viscoelastic models can be safely used without concern for the heterogeneous distribution of filamentous proteins in the cytoskeleton. Therefore, operating at sufficiently large length scales, cells can be considered as continuum media in which the contribution of the microarchitecture can be coarse-grained through constitutive laws. Despite the limited ability of continuum models to explain complex cytoskeletal structures, to date they are still the most efficient means of describing experimental observations on the micrometre scale and to model stress/strain transmission through the cell. These models are particularly useful when associated with coarse-grained relations giving scaling between continuum level rheology and cellular microstructure. Considering the cell as a single phase material, several types of viscoelastic models have been employed to predict the biomechanical behaviour of cells [44]. On the other hand, multiphasic models such as biphasic poroelasticity have been applied to investigate the effects of the different constitutive phases on cell rheology [4, 59].

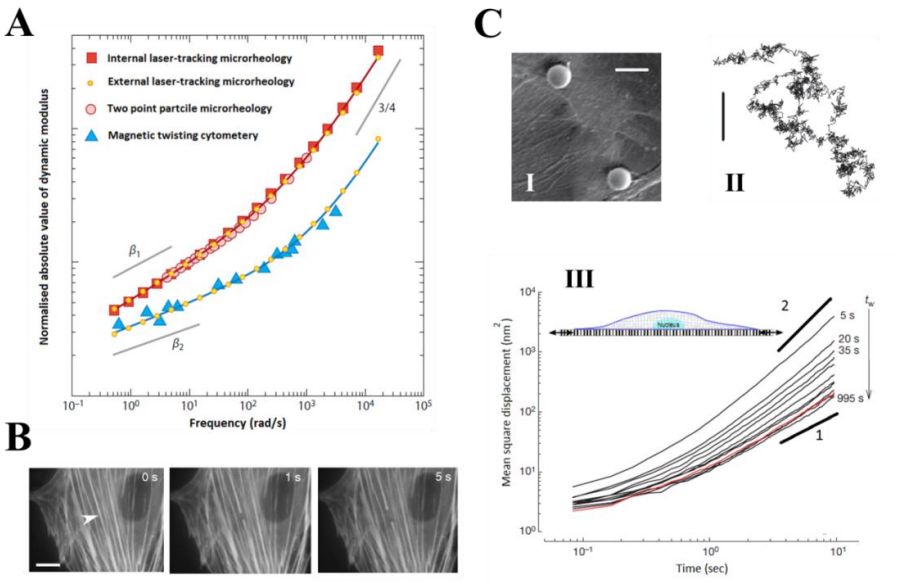

Figure 1-8 Universal phenomenological behaviours of the cell and models of cell rheology.
(A) The frequency response of cells measured with several measurement techniques. Two master curves were obtained after rescaling the results from different rheological measurements. Adapted from: [58]. (B) Spontaneous retraction of a single actin stress fibre upon severing with a laser nanoscissor shows existence of prestress in the cytosketal bundles. Scale bar = 2 µm .Source:[60]. (C) Anomalous diffusion and response of the cell to stretch. Spontaneous movements of beads attached firmly to the cell (C-I, II) show intermittent dynamics. Adapted from [61]. (C-III) The mean square displacement (MSD) of a bead anchored to the cytoskeleton exhibits anomalous diffusion dynamics (subdiffusive at short time intervals and superdiffusive at longer time intervals). Red curve indicates the MSD of the bead for a non-stretched cell and other curves show the MSD of the bead in response to a global stretch measured at different waiting times (t_w) after stretch cessation. Scale bars = 10 µm. Source: [62].

1.4.3 Universality in cell mechanics

Cell mechanical studies over the years have revealed a rich phenomenological landscape of rheological behaviours that are dependent upon probe geometry, loading protocol and loading frequency [58, 63, 64]. More recent mechanical measurements on eukaryotic cells agree on the presence of four universal cellular phenomenological behaviours [65]: 1) Cell rheology is scale free: plots of the frequency response of many cell types on log-log scale display the same shape and follow a weak power law spanning several decades

of frequency [58]. 2) Cells are prestressed: mechanical stresses generated continuously by the internal activity of actomyosin or applied externally on the cell are counterbalanced by the tensional/compressional state of the cytoskeleton [66]. 3) The fluctuation dissipation theorem (FDT) breaks down and diffusion is anomalous [61]: The spontaneous motion of endogenous particles or embedded/attached beads present within the system does not follow the Stokes-Einstein relationship (see section 1.4.4.2 for explanation of this relationship). 4) Stiffness and dissipation are altered by stretch: Application of stretch significantly perturbs the rheological properties of the cell and depending on the experimental condition the cell can exhibit different behaviours such as stress stiffening, fluidisation and rejuvenation [62]. See Figure 1-8 for brief illustration of these universal behaviours.

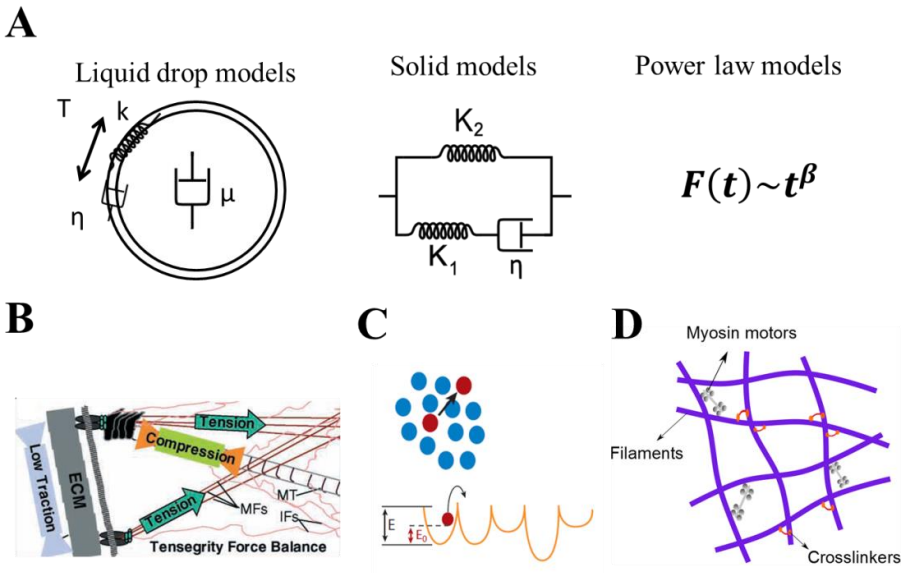

Figure 1-9 Schematic representation of four different models of cell rheology.

(A) Examples of linear viscoelastic models. (B) Tensegrity [66] (C) Soft glassy rheology [67]. (D) Network of semiflexible filaments models (with or without effects of crosslinkers and molecular motors).

Several top-down (linear viscoelasticity, tensegrity, soft glassy rheology) and bottom-up (networks of semiflexible polymers) theoretical models (see Figure 1-9) have been successfully applied to explain the observed phenomenological universal behaviours [64]. However there is still no unifying theory to explain the physical mechanisms that govern these observed universal cellular behaviours. As will be described briefly in the following sections, linear viscoelasticity, immobilized colloids/ soft glasses and the network of semiflexible polymers are the most widely used models that have been proposed to study cell mechanics.

1.4.4 Top-down approaches to studying cell rheology

1.4.4.1 Linear viscoelastic models

Elastic and viscoelastic constitutive laws have been applied to study the response of the whole cell to external forces and to investigate the stress and strain distribution inside the cytoplasm. Whereas the static mechanical properties of cells (elasticity) have been studied in depth, the time-dependent mechanical properties of cells have received significantly less attention. The majority of the work to date utilises an empirical viscoelastic description of cells that assumes the cytoplasm is a single phase homogenous material [32, 53, 68, 69]. The fundamental properties of simple elastic and viscoelastic materials are explained briefly in Chapter 2. The most commonly used viscoelastic models consider the whole cell or part of it as a homogeneous continuum, where the smallest length scale is significantly larger than the dimensions of the microstructural constituents. Examples of such models are cortical shell-liquid core, elastic/viscoelastic solid, and power-law models [44, 64]. The cortical shell-liquid core and elastic/viscoelastic solid models can generate good fits to experimental data by introducing a finite number of elastic and viscous elements (springs and dashpots) coupled in series or parallel leading to exponential decay functions with a finite number of relaxation times [44]. One example of such a model used to fit stress

relaxation is illustrated in Chapter 2.2.2. In contrast to spring-dashpot models, power law models do not have any characteristic relaxation time and cannot be easily described using mechanical analogs. Power law structural damping models have been applied more widely in recent microrheological experiments that measure the viscoelastic response of the cells over a broader range of frequencies and times. Despite their widespread use, the major limitation of these models is that they are not mechanistic, fail to relate the measured rheological properties to structural or biological parameters within the cell, and thus cannot predict changes in rheology due to microstructural changes.

1.4.4.2 Cell as a soft glassy material: macromolecular crowding and anomalous diffusion

A large body of more recent research has found that some of the cellular rheological behaviours are empirically similar to the rheology of soft materials such as foams, emulsions, pastes, and slurries. Following some experimental observations, it was proposed that cells could be considered as soft glassy materials [67]. Indeed, measuring the fluctuations of particles within the cytoplasm revealed that in many cases they exhibit a larger random amplitude of fluctuations than expected and a greater degree of directionality than could be developed solely from thermal fluctuations [70]. In a normal diffusion process (Brownian motion), the mean squared displacement (MSD) of a particle with size a evolves linearly in time t, $\langle r^2 \rangle = 6D_T t$, where D_T is the particle translational diffusion coefficient (D_T can be calculated using the Stokes-Einstein relationship $D_T = k_B T / 6\pi\mu a$ where μ is the viscosity of the medium). However, a semi-empirical equation $\langle r^2 \rangle \sim t^\alpha$ can be used to describe particle fluctuations when it exhibits non-Brownian behaviour as is frequently observed in cellular environments [71, 72]. This deviation from the Stokes-Einstein relationship has been attributed to reaction forces from active cytosketal processes [73] and crowding of a large number of macromolecules inside the cytoplasm such as mobile intracellular globular proteins and

other fixed obstacles like cytoskeletal filaments and organelles [74, 75] that reduce the available solvent volume and provide barriers to particle Brownian motion [76-78].

Based on these observations, it was proposed that the high concentration of different proteins in the cytoplasm can lead to liquid crystal and colloidal behaviours that can be interpreted in terms of the ‘‘soft glassy rheology’’(SGR) model [67]. Crowded colloidal suspensions or soft glasses exhibit a weak power-law rheology corresponding to a continuous spectrum of relaxation times. Similar to this, the dynamic modulus of cells scales with frequency as a weak power law valid over a wide spectrum of time [33, 79]. This semi-empirical SGR behaviour is in contrast to the rheology of semiflexible network of filaments that generally predict a frequency independent dynamic modulus at low frequencies [58].

As a conceptual model, SGR explains how macroscopic rheological responses are linked to localized structural rearrangements originating from structural disorder and metastability. Briefly, the SGR system consists of particles that are trapped in energy landscapes arising from their interactions with surrounding neighbours if there exists sufficient crowding. In such a system, thermal energy is not sufficient to drive structural rearrangement and as a consequence out of equilibrium trapping occurs. With time remodelling/rearrangement (micro-reconfiguration) happens when particles escape the energy barriers of their neighbours and jump from one metastable state to another reaching a more stable state with relaxation rates slower than any exponential process [61]. In such a system, injecting agitational energy sourced from non-thermal origins (such as mechanical shear or ATP-dependent conformational changes of proteins [62]) liberates particles from the energy cages in which they are trapped and facilitates structural rearrangements causing the material to flow.

1.4.5 A bottom up approach: The cell as a dynamic network of polymers

At very short time scales (high frequencies), the cellular viscoelastic dynamic modulus scales with frequency with a universal exponent of 0.75 [80]. This behaviour is analogous to the observed rheology of semiflexible polymer networks [81-84]. This analogy as well as the physical picture of the cell constituted of cytosketal filaments (Figure 1-10A) suggest that the viscoelastic cellular properties originate mainly from the entropic and enthalpic interactions between cytoskeletal structures which largely depend on the architecture and mechanical properties of the constituent cytoskeletal filaments [85].

The flexibility of polymers can be characterised by two length scales, the persistence length l_p and the contour length L [86]. The persistence length or the length of thermal flexibility l_p is the length scale over which thermal bending fluctuations become appreciable and can change the direction of the filament, $l_p = E_f I_f / k_B T$ where $\kappa = E_f I_f$ is the bending modulus of a single filament (or flexural rigidity defined by single filament elastic modulus E_f and its cross-sectional second moment of inertia I_f) and $k_B T$ the thermal energy. A filament is called rigid when $L << l_p$ and flexible when $L >> l_p$ (Figure 1-10B). However, most cytoskeletal gels are networks of semiflexible biopolymer chains with the persistence length of individual chains comparable to their contour length $L \sim l_p$. In such networks, the elastic and dissipative properties originate from entropic (where energy is stored entropically due to the reduction of the number of accessible chain spatial configurations in the network [87]) and enthalpic (where energy is stored in extensional and bending modes of filaments) processes that involve filaments and also the interaction of filaments with the viscous fluid that they are bathed in [86, 88-90]. Furthermore, crosslinking of these semiflexible filaments by specialised (rigid or flexible) proteins at very short distances l_c along the length of each individual filament significantly perturbs the network rheology. Indeed, depending on the properties of

crosslinkers such as length, flexibility and concentration different nonlinear elastic effects can be observed [64].

For purified gels of cytoskeletal filaments such as actin gels, based on a microscopic picture of a network of entangled and crosslinked semiflexible filaments, various mechanical models have introduced different scaling relationships relating viscoelastic properties to microstructural parameters. The persistence length l_p, geometric mesh size λ and a characteristic length L_{ch} have been shown to determine the viscoelasticity of these purified gels. For an actin gel with an actin concentration c_A and a monomeric actin size a, the geometrical mesh size (a measure of the nearest distance between two neighbouring monomers forming part of different filaments) is given by $\lambda \sim 1/\sqrt{ac_A}$ [91]. In dense network regimes ($a << \lambda << l_p$) the elastic modulus scales as $E \sim k_B T \lambda^{-2} l_p^2 l_e^{-3}$ where l_e is the entanglement length (the confining length scale that restrict topological motion of neighbouring filaments). In this entangled network the characteristic length $L_{ch} = l_e$ is the entanglement length l_e and the physical effect of crosslinking from entanglements is to constrain the motion of filaments to a tube-like region, with a diameter $d_e \sim l_e^{3/2} l_p^{-1/2}$, surrounded by other filaments (Figure 1-10C-I). On the other hand for a densely crosslinked gel, the mesh size (scales the same as the entanglement length) is the characteristic length of the network $L_{ch} = l_e \sim \lambda$ (Figure 1-10C-II) and the elastic modulus scales as $E \sim k_B T \lambda^{-5} l_p^2$.

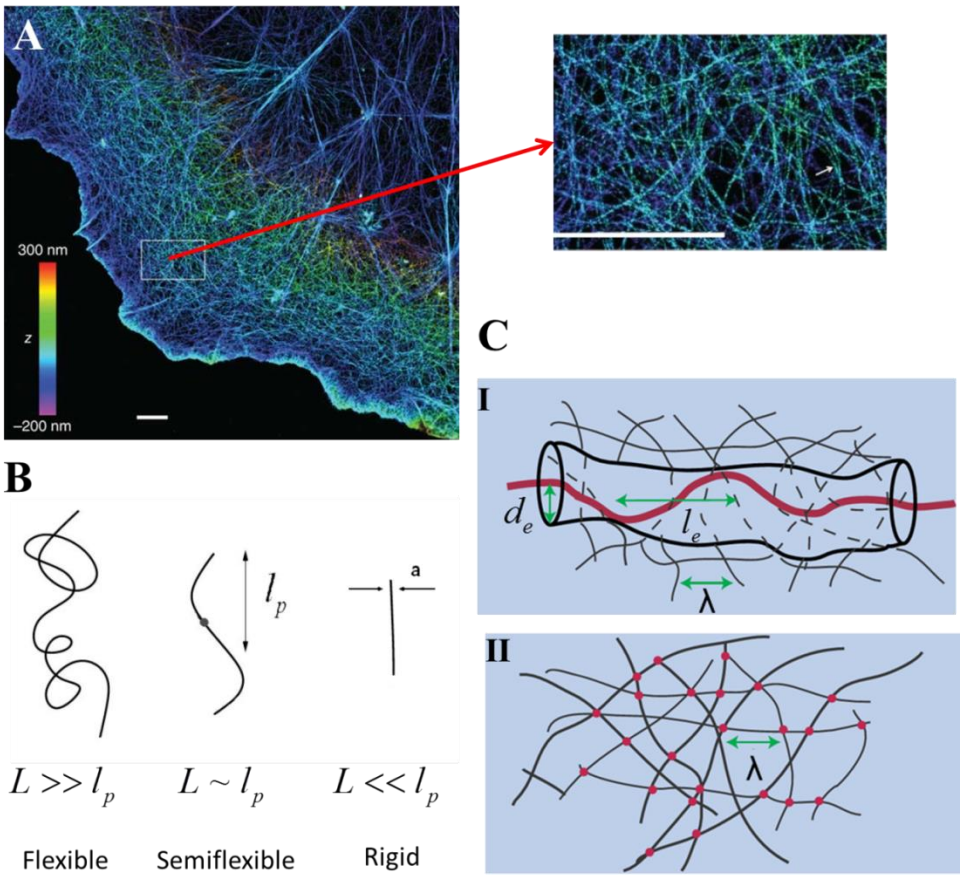

Figure 1-10 Dynamic network of filaments determine the cell rheology.

(A) Image of actin filaments stained with Alexa Fluor 647 phalloidin in a COS-7 cell taken by dual stochastic optical reconstruction microscopy (STORM). The z-position from the substrate is colour coded with respect to the scaling shown in the colour scale bar. Scale bars = 2 μm. Source: [92]. (B) The contour length L of a polymer compared to its persistence length l_p changes the dynamics of polymer networks from flexible to semiflexible and rigid regimes (from left to right respectively). (C) Schematic representation of minimal models for the dynamics of networks of polymers. Semiflexible polymer chains such as actin filaments exhibit complex dynamics under steric entanglements or crosslinks. (C-I) Tube picture of polymer dynamics. Two length scales, λ the mesh size and l_e the entanglement length (or d_e the tube diameter), set the network dynamics. (C-II) For densely crosslinked polymers the mesh size λ or entanglement length $l_e \sim \lambda$ sets the dynamics of network. Source: [32].

The experimentally determined elastic moduli of cells were found to be several orders of magnitude larger than those measured in *in vitro* studies of stress-free F-actin gels and this suggested that the main elastic properties of cells could not result solely from semiflexible networks in a stress free state, such as networks of filamentous actin [93]. This was explained by the fact that unlike most conventional materials, the viscoelastic response of semiflexible networks of biopolymers is highly nonlinear (tension or deformation-dependent) and thus the prestressed state of filaments in the cytoskeleton could result in the high measured elasticities for cells [94]. In addition to the external application of tensional forces, active intracellular processes such as contraction mediated by myosin motor proteins could also generate this prestress. The prestress is transmitted through the cytoplasm by the actin cytoskeleton and balanced by adjacent cells and the extracellular matrix. Furthermore as suggested in the tensegrity model [66, 95], the prestress distribution inside the cytoplasm might be partly balanced by compression of other cytoskeletal filaments such as microtubules.

Considering the cytoskeletal network as a physical gel of purified cytoskeletal filaments is a first step for studying mechanical properties of the cell but yet too simplistic. Indeed cytoskeletal filaments and proteins continuously consume energy released from ATP hydrolysis that turns the system into a non-equilibrium state. This ATP energy is involved in filament polymerisation/depolymerisation, active association/dissociation of crosslinkers and the activity of molecular motors. New theoretical models have been recently proposed to study such non-equilibrium systems [57, 96]. One category of models considers the detailed dynamics of filaments and their interactions with molecular motors and builds up mechanical properties of the filamentous system using microscopic equations and numerical simulations [97]. Alternatively hydrodynamic models describe the behaviour of the mixture by establishing phenomenological relations between a few coarse-grained variables [96, 98].

1.4.6 Biphasic models of cells: a coarse-grained bottom up approach

Considering a cell to be a single phase material is counterintuitive given that more than 60 percent of the cellular content is water. In mammalian cells, most studies view water solely as a solvent and an adaptive component of the cell that engages in a wide range of biomolecular interactions [99]. However less attention has been given to the significance of water in the dynamics of the cytoskeleton, its role in cellular morphology, and motility. Recent experimental work showed the presence of transient pressure gradients inside cells and suggested that these could be explained by the biphasic nature of cytoplasm [100-103]. As a consequence, a biphasic description of cells was proposed based on poroelasticity (or biphasic theory), in which the cytoplasm is biphasic consisting of a porous elastic solid meshwork (cytoskeleton, organelles, macromolecules) bathed in an interstitial fluid (cytosol) [100, 101, 103-105]. In this framework, the viscoelastic properties of the cell are a manifestation of the time-scale needed for redistribution of intracellular fluids in response to applied mechanical stresses and the response of the cell to force application depends on a single experimental parameter: the poroelastic diffusion constant D_p [106], with larger poroelastic diffusion constants corresponding to more rapid stress relaxations. A minimal scaling law $D_p \sim E\xi^2 / \mu$ relates the diffusion constant to the drained elastic modulus of the solid matrix E, the pore size of the solid matrix ξ, and the viscosity of the cytosol μ [100]. Therefore, contrary to viscoelastic models, the dynamics of cellular deformation in response to stress derived from poroelasticity can be described using measurable cellular parameters, allowing changes of rheology with E, ξ, and μ to be predicted which makes this framework particularly appealing conceptually.

1.5 Aims and motivation

One of the most striking features of eukaryotic cells is their capacity to change shape in response to environmental or intrinsic cues driven in large part by their actomyosin cytoskeleton. In studies of cellular morphogenesis, the cytoplasm is generally viewed as an innocuous backdrop enabling diffusion of signalling proteins. This view fails to account for the fact that the time-dependent mechanical properties (or rheology) of the cell are determined by the cytoplasm because it forms the largest part of the cell by volume. During gross morphogenetic changes such as cell rounding, cytokinesis, cell spreading, or cell movement, the cytoskeleton provides the force for morphogenesis but the maximal rate at which shape change can occur is dictated by the rate at which the cytoplasm can be deformed. Using a combination of techniques from molecular cell biology and nanotechnology, my aim is to investigate the biphasic nature of animal cells and its implications for cell rheology. I examine the contribution of intracellular water redistribution to cellular rheology at time-scales relevant to cell physiology (0.5-10s) and investigate how the cytoskeleton and macromolecular crowding interact to set cellular rheology.

Experimental measurements of cellular viscosity are generally interpreted with models that either consider the cell as a single phase homogenous material or describe cell rheology with a continuous spectrum of relaxation times. These models lack predictive power because rheological parameters cannot be related to cellular structural and constitutive parameters. Recent studies [100-102, 107] suggest that water plays an important role in cellular mechanical properties. Based on the physical nature of cytoplasm, it was suggested that cells are like fluid-filled sponges. One very interesting implication of the fluid-sponge model is that cellular rheology depends on only one parameter, the poroelastic diffusion constant, that scales with three structural and constitutive parameters: the sponge elasticity, the sponge pore size, and the viscosity of

the interstitial fluid. Though this is a conceptually attractive model, direct experimental evidence to validate this model has been lacking.

In this thesis, such evidence is presented and I seek to study cell rheology within the framework of poroelasticity. I ask whether cell rheology exhibits a poroelastic behaviour similar to well characterised poroelastic materials such as hydrogels and then I investigate the validity of a poroelastic scaling law by perturbing cellular parameters that are important in setting poroelastic properties. To study cell rheology two experimental approaches were optimised: AFM micro-indentation stress-relaxation tests and whole cell swelling/shrinking experiments. Cellular stress relaxations were measured by rapidly applying a localized force onto cells via an AFM cantilever and monitoring the ensuing stress relaxation over time (Figure 3-2). As an alternative approach, the ability of the poroelastic theory to predict the swelling/shrinking kinetics of the cells was investigated by applying sudden osmotic perturbations and monitoring associated dynamics by defocusing microscopy (Figure 4-7).

1.6 Outline of the following chapters

In Chapter 2, the basic principles of elastic, viscoelastic and poroelastic continuum mechanical theories are introduced. In particular in relation to indentation experiments, Hertzian contact mechanics is briefly overviewed. The theory of linear isotropic poroelasticity is explained more comprehensively followed by the solutions of some fundamental problems useful in interpreting the presented experimental measurements.

In Chapter 3, the techniques and methodologies employed to determine the poroelastic properties of cells are presented. These include cell preparation, chemical and genetic treatments, AFM indentation experiments, particle tracking as well as fluorescent and brightfield microscopy.

In Chapter 4, the ability of the poroelastic theory to describe cellular stress relaxation in response to rapid application of a localised force by AFM are investigated. The cellular force-relaxation curves are compared with stress relaxation curves acquired on well characterised poroelastic hydrogels and the functional form of these curves is discussed in detail. Also in this chapter, the kinetics of cell swelling/shrinking is studied by employing poroelasticity to describe the dynamics of cell volume changes induced via sudden osmotic perturbations and monitored by defocusing microscopy.

In Chapter 5, using indentation tests in conjunction with osmotic perturbations, the validity of the predicted scaling of D_p with pore size is verified qualitatively. Also using chemical and genetic perturbations, the dependence of cytoplasmic rheology on the cytoskeleton is explored. In this chapter, the significance and the implications of the experimental results for understanding the biological determinants of cellular rheology are discussed.

In Chapter 6, the conclusions from this work are summarised and the implications of poroelasticity for cell mechanics are discussed further. Also, prospective work and further experiments that can be performed in the future are presented, including other experimental techniques to investigate time-dependent mechanical properties of cells.

Chapter 2

Theoretical overview of continuum mechanical theories for living cells

Equation Chapter (Next) Section 1

2.1 Theory of linear isotropic elasticity

The elastic framework is the simplest continuum formulation that provides the relationship between deformations/strains and forces/stresses. Linear elasticity is the very simplified version of finite strain theory in which the material strains (ε strain tensor) are considered to be infinitesimal (small deformations) and have a linear relationship with imposed stresses (σ stress tensor). From Newton's second law, the equation of motion for such material transforms into

$$\operatorname{div}\boldsymbol{\sigma} + \rho\mathbf{B} = \rho\ddot{\mathbf{u}} \tag{2.1}$$

where ρ is the density of material, $\mathbf{B}$ body force per unit mass, $\mathbf{u}$ is the vector of solid displacement for small deformations:

$$\varepsilon = 0.5 \ \ \nabla \mathbf{u} + \nabla \mathbf{u}^T \ \ . \tag{2.2}$$

The div and ∇ designate the divergence and gradient operators, respectively. For an isotropic and homogeneous material, the stress-strain relationship is expressed through the constitutive equations:

$$\sigma = 2\mu\,\varepsilon + \lambda\,\mathrm{tr}(\varepsilon)\ \mathbf{I} \tag{2.3}$$

where μ and λ are Lamé's constants, $\mathbf{I}$ the identity tensor and tr the trace operator. The first Lame constant μ is equivalent to the shear modulus G. The following equations define the relationships between Lame's constants , the elastic Young's modulus E and the Poisson ratio ν [108]

$$\begin{aligned} \mu &= \frac{E}{2(1+\nu)}, \\ \lambda &= \frac{2\mu\nu}{1-2\nu}. \end{aligned} \tag{2.4}$$

Using equations (2.1), (2.2), and (2.3), the stress field can be computed from a prescribed displacement field and boundary conditions. On the other hand, compatibility conditions [108] are required to derive a unique displacement field knowing the components of the stress tensor. Typically in most materials, including cells, the body forces and inertial terms can be neglected and thus the equation (2.1) transforms into equilibrium equation, $\mathrm{div}\,\sigma = 0$.

2.1.1 Hertzian contact mechanics: Indentation of elastic material

Here the Landau and Lifshitz [109] approach is presented for studying the contact problem for spherical linear isotropic elastic bodies which is known as Hertz's contact problem. It can be shown that when two smooth surfaces contact each other without deformation (Figure 2-1A) their separation in the z direction h can be expressed in terms of their principal relative radii of curvature. For the contact of two spheres with radii of R_1 and R_2, the separation takes the form:

$$h \approx \frac{1}{2}\left(\frac{1}{R_1} + \frac{1}{R_2}\right)(x^2 + y^2) = \frac{(x^2 + y^2)}{2R^*}, \tag{2.5}$$

where x and y are coordinates lying on the tangent plane of the contact with the contact point as the origin and $R^* = R_1 R_2 / \ R_1 + R_2$ the relative radius of curvature. Now let us apply a total compressive load of F to the touching spheres such that the centres of the two spheres approach one another by an amount $\delta = \delta_1 + \delta_2$. The separation distance between two bodies at a given height z, can be calculated from geometrical considerations shown in Figure 2-1B:

$$h' = h - \delta + (w_1 + w_2) \tag{2.6}$$

where $w_1(x, y)$ and $w_2(x, y)$ are the elastic deformations for surface points on each body respectively. It is trivial that within the contact area $h' = 0$ and outside the contact area $h' > 0$ so that the surfaces do not overlap.

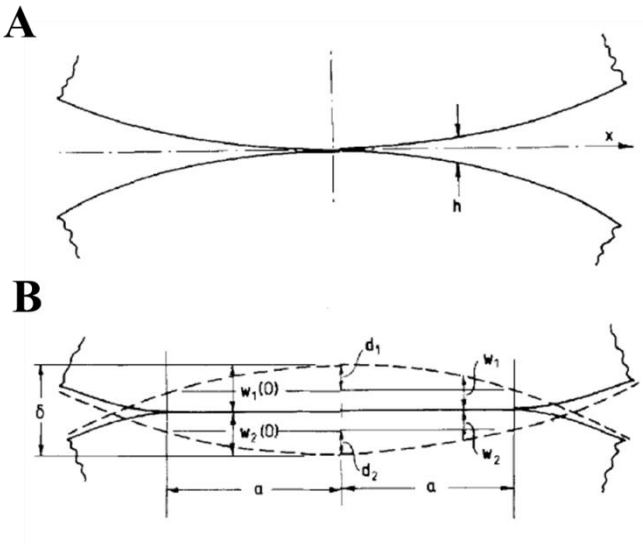

Figure 2-1 The geometry of contact of non-conforming bodies.
(A) Unloaded case where the curved objects are just touching. (B) Loaded case where the curved objects are pressed into each other. Source: [110].

Considering the Hertzian conditions (i.e. continuous, non-conforming and frictionless surfaces, small elastic strains where the radius of contact circle a is much smaller than the relative radius of curvature $a << R^*$ and that each sphere can be considered as an

elastic half-space), the normal displacement of each surface $w_1(x,y)$ or $w_2(x,y)$, can be written in terms of the normal component of pressure p on the surface:

$$w(x,y) = \iint \frac{1-\nu}{2\pi\mu} \frac{p(x',y')}{\sqrt{(x-x')^2+(y-y')^2}} dx'dy'. \tag{2.7}$$

Within the contact area, $h' = 0$, substituting the above equation into the geometrical relationship (2.6) yields:

$$\begin{aligned} \frac{1}{2\pi}\left(\frac{1-\nu_1}{\mu_1}+\frac{1-\nu_2}{\mu_2}\right)\iint \frac{p(x',y')}{\sqrt{(x-x')^2+(y-y')^2}} dx'dy' \\ = \delta - \frac{1}{2}\left(\frac{1}{R_1}+\frac{1}{R_2}\right)(x^2+y^2). \end{aligned} \tag{2.8}$$

Solving (2.8) by applying potential theory [109], results in the following relationships for the pressure field distribution and the contact radius

$$p(r) = \frac{3}{2} p_m \sqrt{1-\left(\frac{r}{a}\right)^2}, \tag{2.9}$$

$$a = \frac{3\pi}{8}\left(\frac{1-\nu_1}{\mu_1}+\frac{1-\nu_2}{\mu_2}\right)\left(\frac{R_1R_2}{R_1+R_2}\right)p_m \tag{2.10}$$

where $r = x^2 + y^2$ and p_m is the average pressure over the contact area

$$F = \int_0^a p(r) 2\pi r dr = p_m \pi a^2. \tag{2.11}$$

Substituting the pressure field $p(r)$ into equation (2.7), we find the normal displacement:

$$w(r) = \frac{1-\nu}{\mu^*}\frac{3\pi p_m}{4a}\left(2a^2 - r^2\right), \tag{2.12}$$

with the equivalent shear modulus μ^* defined as:

$$\frac{1}{\mu^*} = \frac{1-\nu_1}{\mu_1} + \frac{1-\nu_2}{\mu_2}. \tag{2.13}$$

Using above the equation and substituting equations (2.5) and (2.12) into equation (2.6) one can obtain the following relationship within the contact area:

$$\frac{3\pi p_m}{16a\mu^*}\ 2a^2 - r^2\ = \delta - \frac{r^2}{2R^*} \tag{2.14}$$

from which the mutual approach of the distant points in the two solids can be derived:

$$\delta = \frac{3\pi p_m a}{8\mu^*}. \tag{2.15}$$

All parameters can be expressed in terms of total load F as in practice this parameter is specified:

$$F = \frac{8}{3}\frac{\mu^*}{R^*}a^3 = \frac{8}{3}\mu^*\sqrt{R^*}\delta^{3/2}, \tag{2.16}$$

where $a = \sqrt{R^*\delta}$. One special case of the Hertz contact problem which is of interest to us is where one sphere is rigid ($\mu_1 \to \infty$) and of finite radius R_1 and the other sphere is elastic μ_2 but $R_2 \to \infty$. This is the case of indentation of a semi-infinite domain and for this case the force-indentation relationship is

$$F = \frac{8\mu_2}{3(1-\nu_2)}\sqrt{R_1}\delta^{3/2}. \tag{2.17}$$

2.2 Linear viscoelasticity

A viscoelastic material undergoing deformation simultaneously stores and dissipates mechanical energy. Viscoelasticity is the phenomenological theory which describes the time-dependent response of such material. In this framework regardless of the microstructure of the material, the relaxation processes are represented by exponential or power law functions of time. In models based on exponential relaxation processes, stress or strain functions can be represented by combining spring and dashpot elements. In such models, the resultant exponential functions can have a single relaxation time if there is only one dashpot element or a distribution of relaxation times if there are several. On the other hand, another type of relaxation model that cannot be represented by simple mechanical analogues but is encountered experimentally widely in the dynamics of complex materials is power law relaxation.

2.2.1 Storage and loss moduli

The stress-strain relationship for a linear viscoelastic isotropic material can be expressed in the time domain as:

$$\sigma = 2\int_{-\infty}^{t} \mu(t-\tau)\frac{\mathrm{d}\varepsilon}{\mathrm{d}\tau}\,\mathrm{d}\tau + \int_{-\infty}^{t} \lambda(t-\tau)\{\mathrm{tr}\ \frac{\mathrm{d}\varepsilon}{\mathrm{d}\tau}\}\mathbf{I}\,\mathrm{d}\tau = \int_{-\infty}^{t} G_{\alpha}(t-\tau)\frac{\mathrm{d}\varepsilon}{\mathrm{d}\tau}\,\mathrm{d}\tau, \qquad (2.18)$$

where $\mathrm{d}\varepsilon/\mathrm{dt}$ is the shear rate and $G_{\alpha}(t-\tau)$ is the relaxation modulus designating the deviatoric and the dilational part of the stress-strain relationship by $\alpha = 1$ and $\alpha = 2$ respectively [111]. This equation implies that small changes in strain can be integrated over time to yield the total stress.

The response of a material under oscillatory excitations is a typical way of measuring shear viscoelastic properties. Let us assume that the material is subjected to an oscillatory strain with amplitude ε_0 and frequency ω. Substituting a strain of the form $\varepsilon(t) = \varepsilon_0 \sin\omega t$ (with the corresponding strain rate of $\mathrm{d}\varepsilon/\mathrm{dt} = \omega\varepsilon_0\cos\omega t$) into equation (2.18) and performing some algebra gives the stress-strain relationship:

$$\begin{aligned}\sigma(t) &= \varepsilon_0\left[\omega\int_0^{\infty} G(\tau)\sin\omega\tau\,\mathrm{d}\tau\right]\sin\omega t + \varepsilon_0\left[\omega\int_0^{\infty} G(\tau)\cos\omega\tau\,\mathrm{d}\tau\right]\cos\omega t \\ &= \varepsilon_0 G'\sin\omega t + \varepsilon_0 G''\cos\omega t = G'\varepsilon + \frac{G''}{\omega}\frac{\mathrm{d}\varepsilon}{\mathrm{dt}},\end{aligned} \qquad (2.19)$$

where $G' = \omega\int_0^{\infty} G(\tau)\sin\omega\tau\,\mathrm{d}\tau$ is the shear storage modulus and $G'' = \omega\int_0^{\infty} G(\tau)\cos\omega\tau\,\mathrm{d}\tau$ the shear loss modulus. The physical meaning of the storage and loss moduli can be explained as follows: if the material response is purely elastic then the storage modulus G' is the non-vanishing term in equation (2.19). In this case G' appears as the frequency-dependent shear modulus similar to a simple elastic material where the stress is in phase with the strain: $\sigma \sim \mu\varepsilon$. On the other hand, for a purely viscous material $G' = 0$ and the loss modulus G'' is the only non-vanishing term. This results in a stress-response that has a phase lag of $\pi/2$ with strain and G''/ω acts as the

frequency-dependent dynamic viscosity (similar to Newtonian fluid behavior $\sigma \sim \eta \, d\varepsilon / dt$, where η is the viscosity). Unlike purely elastic or purely viscous materials, viscoelastic materials exhibit a mixed behaviour with a phase lag of φ $(0 < \varphi < \pi/2)$ between the applied strain and the resultant stress.

From an experimental point of view, one way to determine the viscoelastic properties of a material is to measure the stress response of the material in response to an applied oscillatory strain of the form $\varepsilon(t) = \varepsilon_0 \sin \omega t$. Let us consider the measured stress-response to have the form $\sigma(t) = \sigma_0 \sin \ \omega t + \varphi$ where σ_0 is the amplitude of stress oscillations. Using equation (2.19), the following relationships can be used to calculate the frequency-dependent storage and loss moduli of the material:

$$\begin{aligned} G' &= \frac{\sigma_0}{\varepsilon_0} \cos \varphi, \\ G'' &= \frac{\sigma_0}{\varepsilon_0} \sin \varphi. \end{aligned} \tag{2.20}$$

2.2.2 Standard linear solid model

In this section the standard linear solid model (also known as the Zener model) which has been widely used to describe the time-dependent behaviours of biomaterials such as living cells [51, 53, 54] (see Figure 2-2A) is presented. The differential equation describing this model is:

$$\eta \frac{d\sigma}{dt} + K_1 \sigma = \eta \ \ K_1 + K_2 \ \ \frac{d\varepsilon}{dt} + K_1 K_2 \varepsilon. \tag{2.21}$$

Applying a sudden constant strain $\varepsilon = \varepsilon_0 H(t)$ (where $H(t)$ is the Heaviside step function) or a sudden constant stress $\sigma = \sigma_0 H(t)$ on a Zener viscoelastic material results in a stress-relaxation or creep response :

$$\sigma = \varepsilon_0 \left(K_2 + K_1 e^{-\frac{K_1}{\eta} t} \right), \text{ Figure 2-2B,} \tag{2.22}$$

$$\varepsilon = \frac{\sigma_0}{K_2}\left(1 - \frac{K_1}{K_1 + K_2} e^{-\frac{K_1 K_2}{K_1 + K_2}\frac{t}{\eta}}\right), \text{ Figure 2-2C.} \tag{2.23}$$

Performing some mathematical substitutions, equation (2.21) can be solved to obtain the dynamic response of a Zener material to an oscillatory load with G' and G'' taking the form (as plotted in Figure 2-2D):

$$\begin{aligned} G' &= \frac{{K_1}^2 K_2 + (K_2 + K_1)\eta^2\omega^2}{{K_1}^2 + \eta^2\omega^2}, \\ G'' &= \frac{{K_1}^2 \eta\omega}{{K_1}^2 + \eta^2\omega^2} \end{aligned} \tag{2.24}$$

2.2.3 Power law models

One of the most surprising features of a wide range of soft materials is that they display a power law behaviour in which their relaxation spectrum lacks any characteristic time scale. It is surprising because materials (including living cells) with very different microstructural organization exhibit the same empirical behaviour. The creep and stress relaxation responses of such power-law material can be written in the form:

$$\begin{aligned} \varepsilon(t) &= \sigma_0 / K_0 \left(\frac{t}{t_0}\right)^{\beta} \\ \sigma(t) &= K_0 \varepsilon_0 \left(\frac{t}{t_0'}\right)^{-\beta} \end{aligned} \tag{2.25}$$

where K_0 is the parameter characterizes the softness or compliance of the material and t_0 and t_0' are the normalization timescales that can be chosen arbitrary [64]. In other words, K_0 is the ratio of stress to unit strain measured at an arbitrary chosen time t_0 [112]. The timescale invariant behavior of power law functions comes from the fact that changing t_0 or t_0' does not affect the value of β. This equation can describe linear elastic and Newtonian viscous behavior for β = 0 and β = 1 respectively. Using this equation, non-exponential relaxation processes can be described in a very economical way with a small number of parameters. Considering equations (2.19) and (2.25), the response of the

material to dynamic loading also follow a power law with the same exponent β, $G', G'' \sim \omega^{\beta}$ [113, 114].

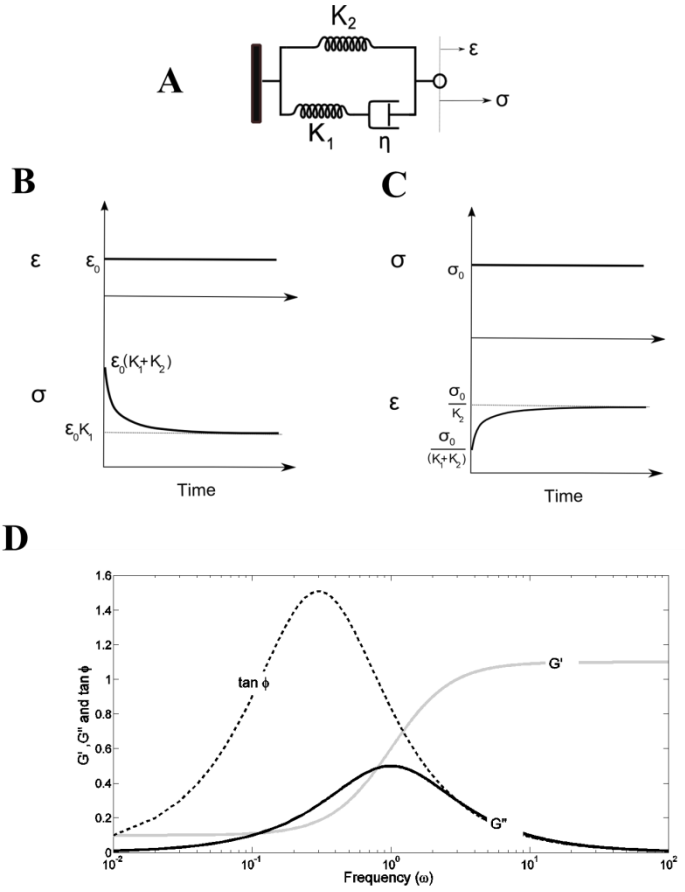

Figure 2-2 The standard linear solid viscoelastic model.

(A) The standard linear solid model consists of a spring K_2 in parallel with a spring K_1 in series with a dashpot η. (B) Stress-relaxation: the stress relaxes exponentially over time in response to application of a sudden constant strain. (C) Creep: in response to application of a sudden constant stress, the strain increases instantaneously until it reaches its final value. (D) Dynamic response of Zener model (with $K_1 = 1$ pa, $K_2 = 0.1$ pa and $\eta = 1$ pa.s): plot of the storage and loss moduli as a function of applied frequency.

2.3 Poroelasticity

The theory of poroelasticity studies the behaviour of a porous medium consisting of an elastic solid matrix infiltrated by an interconnected network of fluid saturated pores.

2.3.1 Theory of linear isotropic poroelasticity

In this section the governing equations for a linear isotropic poroelastic material are presented [115]. The constitutive equations are an extension of linear elasticity to poroelastic materials first introduced by Biot [116]. Alternatively one can use the biphasic model [117] that has been extensively applied in modelling the mechanics of articular cartilage and other soft hydrated tissues. Biot's formulation can be simplified when poroelastic parameters assume their limiting values. Under the "incompressible constituents" condition, the material exhibits its strongest poroelastic effect and the Biot poroelastic theory can be mathematically transformed to the biphasic model.

Constitutive law Let us consider the quasistatic deformation of an isotropic fully saturated poroelastic medium with a constant porosity. The constitutive equation relates the total stress tensor σ to the infinitesimal strain tensor ε of the solid phase and the pore fluid pressure p:

$$\sigma = 2G_s\varepsilon + \frac{2G_s\nu_s}{(1-2\nu_s)}\,\mathrm{tr}(\varepsilon)\ \mathbf{I} - p\mathbf{I}, \tag{2.26}$$

where G_s and ν_s are the shear modulus and the Poisson ratio of the drained network respectively, and $\theta = \mathrm{tr}\ (\varepsilon)$ the variation in fluid content. This equation is similar to the constitutive governing equation for conventional single phase linear elastic materials. However the time dependent properties are incorporated through the pressure term that acts as an additional external force on the solid phase.

Equilibrium equation In the absence of body forces and neglecting the inertial terms, the local stress balance results in the equilibrium equation

$$\operatorname{div}\boldsymbol{\sigma} = 0. \tag{2.27}$$

Darcy transport law Darcy's law considers fluid transport through the non-deformable porous medium

$$\mathbf{q} = -K\nabla p \tag{2.28}$$

where $\mathbf{q}$ is the filtration velocity and K the hydraulic permeability.

Continuity equation Neglecting any source density, the mass conservation of a fluid yields:

$$\operatorname{div}\mathbf{q} = -\frac{\partial\theta}{\partial t}. \tag{2.29}$$

2.3.2 Diffusion equation

Combining the continuity equation and Darcy's law results in

$$\frac{\partial\,\theta}{\partial t} = K\nabla^2 p. \tag{2.30}$$

Applying the equilibrium condition to the constitutive law, one can obtain the Navier equations

$$G_s\nabla^2\mathbf{u} + \frac{G_s}{(1-2\nu_s)}\nabla\ \operatorname{div}\mathbf{u}\ - \nabla p = 0, \tag{2.31}$$

where $\mathbf{u}$ is the vector of solid displacement for small deformations $\boldsymbol{\varepsilon} = 0.5\ \nabla\mathbf{u} + \nabla\mathbf{u}^T$, and ∇^2 designates the Laplacian operator.

The diffusion equation for $\theta = \operatorname{tr}(\boldsymbol{\varepsilon})$ is obtained by combining equations (2.30) and (2.31)

$$\frac{\partial\,\theta}{\partial t} = D_P\nabla^2\theta \tag{2.32}$$

where D_p is the poroelastic diffusion coefficient:

$$D_p = \frac{2G_s(1-\nu_s)}{(1-2\nu_s)}K \tag{2.33}$$

Equation (2.32) is the fundamental equation in the theory of consolidation which deals with the time dependent settlement of porous materials. Derivation of the diffusion equation implies that under the assumptions made in this section, there are three independent sets of parameters (G_s, ν_s and K) that characterize the mechanical properties of a poroelastic medium.

2.3.3 Scaling law between poroelastic properties and microstructural parameters

One important consequence of considering a poroelastic cytoplasm is that the measured macroscopic mechanical properties of the cell can be related to some coarse-grained cellular microstructural parameters and the hydraulic pore size ξ of the cytoplasm can be determined as a first step to understanding the microstructure of the cell. Considering a simple Poiseuille flow inside a tube of radius r, the relationship between the flow rate Q and the pressure gradient ∇p is given by

$$Q = \frac{\pi r^4}{8\mu}\nabla p, \tag{2.34}$$

where μ is the viscosity of the fluid. For a porous body that contains n straight tubes per unit area with porosity $\varphi = n\pi r^2$ the filtration velocity is

$$q = nQ = -\frac{n\pi r^4}{8\mu}\nabla p = -\frac{\varphi r^2}{8\mu}\nabla p. \tag{2.35}$$

Taking into account irregularities, interconnectivities and tortuosities of the pores in a real porous matrix the above relationship reads:

$$q = -\frac{\varphi r^2}{4\mu\kappa}\nabla p, \tag{2.36}$$

where κ is the Kozney constant [118]. Considering equation (2.36) and a simple analogy between the described Poiseuille flow and the flow through the porous matrix with an

average pore size ξ (Darcy's law) leads to the following relationship for the hydraulic permeability K

$$K = \frac{\varphi}{4\kappa}\frac{\xi^2}{\mu}, \tag{2.37}$$

Substituting this equivalent expression for the hydraulic permeability into equation (2.33) results in:

$$D_p = \left(\frac{(1-\nu_s)}{(1+\nu_s)(1-2\nu_s)}\frac{\varphi}{4\kappa}\right)\frac{E_s\xi^2}{\mu}. \tag{2.38}$$

As a first approximation all of the parameters inside the parenthesis are assumed to be a constant α and the functional dependence of all parameters with respect to the porosity of the structure φ is neglected. Therefore a fundamental scaling law for poroelastic cytoplasm takes the form:

$$D_p \sim \frac{E\xi^2}{\mu}, \tag{2.39}$$

where μ is interpreted as the interstitial fluid viscosity, and $E = 2G_s\ 1+\nu_s$ the average elasticity of the constituent solid network.

2.3.4 Poroelastic swelling/shrinking of gels under osmotic stress

The fundamental poroelastic equations for swelling/shrinking of gels under osmotic perturbation are very similar to the ones presented in section 2.3.1 with a redefinition of some parameters such as pore pressure and fluid flux [119]. Let us consider the initial state of the gel to be homogeneous and free from mechanical load with C_0 the initial concentration of solvent inside the gel and μ_0 the initial chemical potential of the gel. Equation (2.29) rewritten in terms of the concentration of the solvent in the gel is:

$$\operatorname{div}\mathbf{q} = -\frac{\partial C}{\partial t}. \tag{2.40}$$

Darcy's law defines the migration of the solvent in the gel, thus equation (2.28) transforms to

$$\mathbf{q} = -\ \frac{K}{\Omega^2}\ \nabla\mu, \tag{2.41}$$

where Ω is the volume per solvent molecule and μ the time-dependent chemical potential of the solvent. Incompressibility of the network and the solvent imply that the change in volume of the gel is only due to migration of solvent molecules into or out of the network which changes the volume of solvent inside the gel:

$$\mathrm{tr}(\varepsilon) = \Omega(C - C_0). \tag{2.42}$$

At thermodynamic equilibrium, the work done on each element of the gel equals the change in free energy δW written as $\delta W = \mathrm{tr}(\boldsymbol{\sigma}.\delta\varepsilon) + (\mu - \mu_0)\delta C$, where W is the Helmholtz free energy per unit volume of the gel. In this relationship $tr(\boldsymbol{\sigma}.\delta\varepsilon)$ is the mechanical work due to stress and $(\mu - \mu_0)\delta C$ is the work done by the chemical potential. Using equation (2.42) one can write the change in free energy in terms of only the strain tensor $\delta W = \mathrm{tr}(\boldsymbol{\sigma}.\delta\varepsilon) + (\mu - \mu_0)\mathrm{tr}\ \varepsilon\,/\,\Omega$ which yields:

$$\boldsymbol{\sigma} = \frac{\partial W(\varepsilon)}{\partial \varepsilon} - \frac{(\mu - \mu_0)}{\Omega}\mathbf{I}. \tag{2.43}$$

The free energy can be written as a function of the strain tensor in the linear case of an isotropic gel:

$$W = G_s[\mathrm{tr}(\varepsilon^2) + \frac{\nu_s}{(1-2\nu_s)}tr(\varepsilon)^2]. \tag{2.44}$$

Combining equations (2.43) and (2.44) results in equation (2.26) replacing pore pressure by the term $(\mu - \mu_0)\,/\,\Omega$:

$$\boldsymbol{\sigma} = 2G_s\varepsilon + \frac{2G_s\nu_s}{(1-2\nu_s)}\,\mathrm{tr}\ \varepsilon\,\mathbf{I} - \frac{\mu - \mu_0}{\Omega}\mathbf{I}. \tag{2.45}$$

Navier and diffusion equations similar to the Biot poroelasticity equations can then be derived using the above equations:

$$G_s\nabla^2\mathbf{u} + \frac{G_s}{(1-2\nu_s)}\nabla\ \ \mathrm{div}\,\mathbf{u}\ \ - \frac{1}{\Omega}\nabla\mu = 0, \tag{2.46}$$

$$\frac{\partial C}{\partial t} = D_P \nabla^2 C. \tag{2.47}$$

These equations can be used to define the dynamics of gel swelling/shrinkage in response to a change in extracellular osmolarity. Experiments in Chapter 4.2 examines this situation in conjunction with the measurement of surface displacements of the gel by defocusing microscopy to determine D_P.

2.4 Basic 1D solutions for fundamental poroelasticity problems

2.4.1 Uniaxial strain (confined compression)

Let us consider the situation where all the components of the strain tensor except $\varepsilon_{xx} = \partial u_x / \partial x$ are zero so that the poroelastic material is only allowed to deform in one direction. In this case the non-zero components of the stress tensor reduce to

$$\begin{cases} \sigma_{xx} = \dfrac{2G_s(1-\nu_s)}{(1-2\nu_s)}\varepsilon_{xx} - p \\ \sigma_{yy} = \sigma_{zz} = \dfrac{2G_s\nu_s}{(1-2\nu_s)}\varepsilon_{xx} - p = \dfrac{\nu_s}{(1-\nu_s)}\sigma_{xx} - \dfrac{(1-2\nu_s)}{(1-\nu_s)}p. \end{cases} \tag{2.48}$$

Substituting u_x as the only component of the displacement field into the Navier equation (2.31), reads

$$\frac{2G_s(1-\nu_s)}{(1-2\nu_s)}\frac{\partial^2 u_x}{\partial x^2} - \frac{\partial p}{\partial x} = 0 \tag{2.49}$$

Combining equations (2.30) and (2.48) and using the fact that $\varepsilon_{xx} = \theta$, the diffusion equation for the pore pressure is obtained:

$$\frac{\partial p}{\partial t} - D_p \frac{\partial^2 p}{\partial x^2} = -\frac{\partial \sigma_{xx}}{\partial t} \tag{2.50}$$

Contrary to equation (2.32), equation (2.50) is an inhomogeneous diffusion equation that can be solved by specifying a stress condition. In the following the one dimensional time-

dependent settlement of a poroelastic material subjected to certain types of boundary conditions is studied.

2.4.2 One dimensional consolidation

Finite domain creep problem Consider a porous plunger that compresses a poroelastic material confined in a cylinder of height L as shown in Figure 2-3. At $t=0$ a certain constant load $\sigma_{xx}(0,t)=\sigma_0 H(t)$ is applied on the solid matrix and held constant. Under this condition the pressure diffusion equation (2.50) transforms into a homogeneous diffusion equation

$$\frac{\partial p}{\partial t}=D_p\frac{\partial^2 p}{\partial x^2}. \tag{2.51}$$

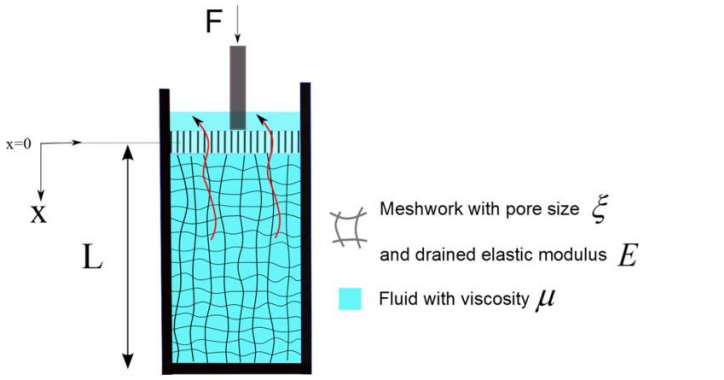

Figure 2-3 Compression of a porous solid with an interstitial fluid by a porous plunger.
The fluid diffuses out through the meshwork and exits through the plunger (red arrows) applying the external load.

Assuming an ideal permeable plunger and zero flux at the bottom of the cylinder yields $p = 0$ at $x = 0$ and $\partial p / \partial x = 0$ at $x = L$ respectively. Considering the above boundary and initial conditions one can solve equation (2.51) analytically:

$$p(x,t) = \sigma_0 \sum_{n=1,3,..}^{\infty} \frac{4}{m\pi} \sin \left(\frac{n\pi x}{2L} \right) \exp \left(-n^2 \pi^2 \tau \right) \tag{2.52}$$

where $\tau = D_p t / 4L^2$ is a dimensionless time. The solid phase displacement field is calculated employing equation (2.49) and the following boundary conditions $u_x = 0$ at $x = L$:

$$u_x(x,t) = \sigma_0 \frac{(1-2\nu_s)L}{2G_s(1-\nu_s)} \sum_{n=1,3,..}^{\infty} \frac{8}{n^2\pi^2} \cos \left(\frac{n\pi x}{2L} \right) \left(1 - \exp \left(-n^2 \pi^2 \tau \right) \right) \tag{2.53}$$

Semi-infinite domain creep problem Now I consider the case where the poroelastic material inside the cylinder is infinitely extended in the x direction. In this case, all the boundary and initial conditions are the same as for the finite domain problem except that $u_x = 0$ when $x = +\infty$ which implies that the dissipations arising from solid fluid interactions vanishes to zero at infinity, $\partial p / \partial x = 0$. The solutions for the pore pressure and displacement field for a creep problem of a semi-infinite poroelastic domain can be written as

$$p(x,t) = \sigma_0 \mathrm{erf} \left(\frac{x}{2\sqrt{D_p t}} \right) \tag{2.54}$$

$$u_x(x,t) = \sigma_0 \frac{(1-2\nu_s)}{2G_s(1-\nu_s)} \left[2\sqrt{\frac{Dt}{\pi}} e^{-\frac{x^2}{4D_p t}} - x \, \mathrm{erfc} \left(\frac{x}{2\sqrt{D_p t}} \right) \right]. \tag{2.55}$$

Figure 2-4 illustrates the normalized pore pressure and displacement field as a function of depth at different times for $D_p = 1$. At $x = 0$ The settlement on the surface is

$$u_x(0,t) = \sigma_0 \frac{(1-2\nu_s)}{2G_s(1-\nu_s)} 2\sqrt{\frac{Dt}{\pi}}. \tag{2.56}$$

The solutions for application of a sudden loading of the top surface by a fluid with pressure p_0 can be derived similarly assuming the following boundary conditions $p(0,t) = p_0 H(t)$ and $\sigma_{xx}(0,t) = 0$. The displacement solutions are exactly similar to equations (2.53) and (2.55) replacing σ_0 with p_0. However the pore pressure solutions take the form

$$p(x,t) = p_0 \left(1 - \sum_{n=1,3,..}^{\infty} \frac{4}{m\pi} \sin \frac{n\pi x}{2L} \exp -n^2\pi^2\tau \right), \tag{2.57}$$

$$p(x,t) = p_0 erfc\left(\frac{x}{2\sqrt{D_p t}} \right) \tag{2.58}$$

for finite and infinite domains respectively.

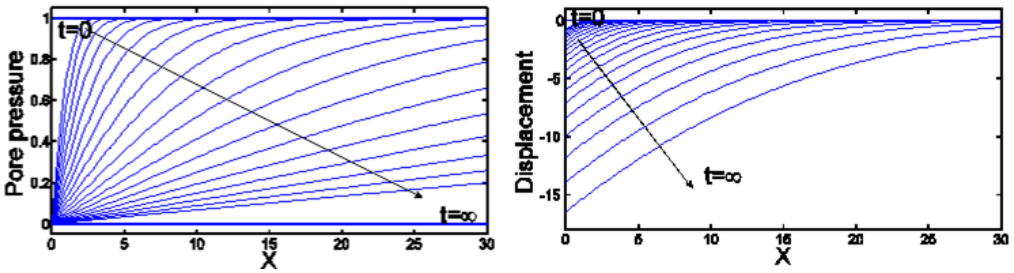

Figure 2-4 Creep response of a poroelastic half-space.

Pore pressure (left) and displacement (right) solutions for the semi-infinite domain creep problem. The curves are plotted as a function of depth at different times for $D_p = 1$.

In our experimental setup, cells have a finite thickness, therefore it is important to investigate the time/length scales at which the semi-infinite solutions are applicable to finite domain problems. Considering equation (2.58), at distance $x = L$, it takes a time t larger than $0.13L^2 / D_p$ for the pore pressure to reach 5% of its maximum value at the loaded boundary. Thus at times less than $0.13L^2 / D_p$ the pore pressure perturbation at the boundary $x = 0$ weakly influences the pore pressure at $x = L$. In other words, at distances beyond $3\sqrt{D_p t}$ the pore pressure is less than 5% of its maximum at the

boundary. In conclusion, at short times, perturbations applied to the surface boundary are confined to small regions near the boundary and thus the solution for the confined problem can be estimated from semi-infinite solutions.

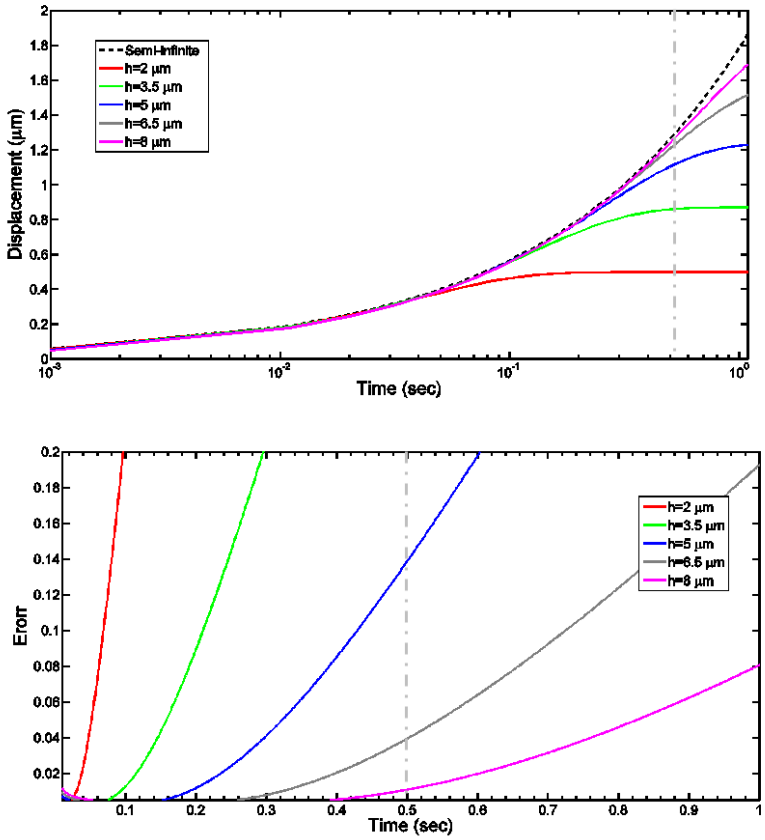

Figure 2-5 Creep response of a finite domain.

Top: Settlement response of the surface following a sudden application of σ_{ave} = 250 Pa for a poroelastic material with E_s = 1 kPa, ν_s = 0 and D_p = 40 μm^{2}s^{-1}. The dashed line is the semi-infinite response and the lines are the solutions of equation (2.53) for poroelastic materials of thicknesses ranging from h = 2 to 8 μm. Bottom: The displacement error considering the semi-infinite solution as the exact solution for the finite thickness domain.

Furthermore, in relation to real AFM indentation experiments, to investigate the time scales at which the half-space approximation can be employed, representative values of the physical parameters derived from experimental data were used to compare the surface

displacements ($x = 0$) in equations (2.53) and (2.56) for finite and semi-infinite domains. As will be described later in Chapter 4, application of F ~ 6 nN via a spherical tip with radius R = 7.5 μm results in indentation depths of δ_0 ~ 1 μm which leads to an average stress of $\sigma_{ave} = F / \pi R\delta$ ~ 250 Pa. Figure 2-5 shows the displacement as a function of time considering thicknesses H = 2 - 8 μm for a poroelastic material. It can be observed from this figure that for very small thicknesses (H < 3 μm) the semi-infinite solution is applicable only at very short times (t < 100 ms). For thicknesses of H ~ 5 μm (as shall be seen later this is approximately the height of the cells studied in this thesis) the semi-infinite approximation is valid for the first ~ 300 ms of the process. The half-space solution is a very good approximation for longer times (t ~ 1 s) if the thickness is H > 8 μm.

Semi-infinite domain stress relaxation Let us consider again the semi-infinite problem but with sudden application of displacement $u(0,t) = UH(t)$ instead of load on the top surface of a poroelastic material. This is the case of stress relaxation where the pressure is suddenly increased due to fast compression of the top layer followed by relaxation over time. Considering the far field conditions $u = \partial p / \partial x = 0$ at $x = \infty$, the strain diffusion equation (2.32) transforms into a displacement diffusion equation

$$\frac{\partial\, u_x}{\partial t} = D_P \frac{\partial^2 u_x}{\partial x^2}. \tag{2.59}$$

The displacement field satisfying the boundary conditions can be found as

$$u_x(x,t) = U \operatorname{erfc}\left(\frac{x}{2\sqrt{D_p t}}\right). \tag{2.60}$$

The corresponding pressure field becomes

$$p(x,t) = \frac{U}{K}\sqrt{\frac{D_p}{\pi t}}\left(1 - e^{-\frac{x^2}{4D_p t}}\right) \tag{2.61}$$

In Figure 2-6 the normalized pore pressure and the displacement field are plotted as a function of depth at different times for $D_p = 1$.

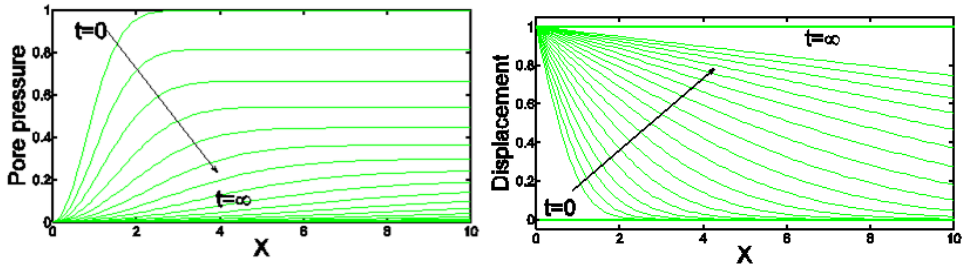

Figure 2-6 Stress relaxation response of a poroelastic half-space.

Pore pressure (left) and displacement (right) solutions from the semi-infinite domain stress relaxation problem. The curves are plotted as a function of depth at different times for $D_p = 1$.

2.5 Indentation of a poroelastic material

Conventional engineering methods such as compression, tensile and shear tests have limitations for the characterisation of very soft materials due to difficulties in manipulating soft and very small samples. Furthermore these methods do not have the necessary accuracy and sensitivity to study the time-dependent dynamics of very soft materials with short time scale responses. One of the best methods for characterisation of very soft materials, especially cells, is an indentation test and as explained later in chapter 3, I conducted AFM dynamic micro-indentation experiments to study cell rheology in the framework of poroelasticity. For indentation of a purely elastic material, there presently exist several closed-form formulations such as Hertz's equation (2.17) for obtaining cellular elastic properties such as the shear modulus. Some closed-form expressions have also been proposed for characterisation of time-dependent viscoelastic materials such as indentation of a Zener viscoelastic material as presented in Chapter 3.7.3 . However due to the higher complexity of the poroelastic equations, geometry and boundary conditions,

there exists no simple closed-form analytical solution that can be used to fit experimental data. Therefore in this work an empirical expression derived from finite element (FE) simulations [120] was employed to fit experimental poroelastic relaxation responses in AFM indentation tests.

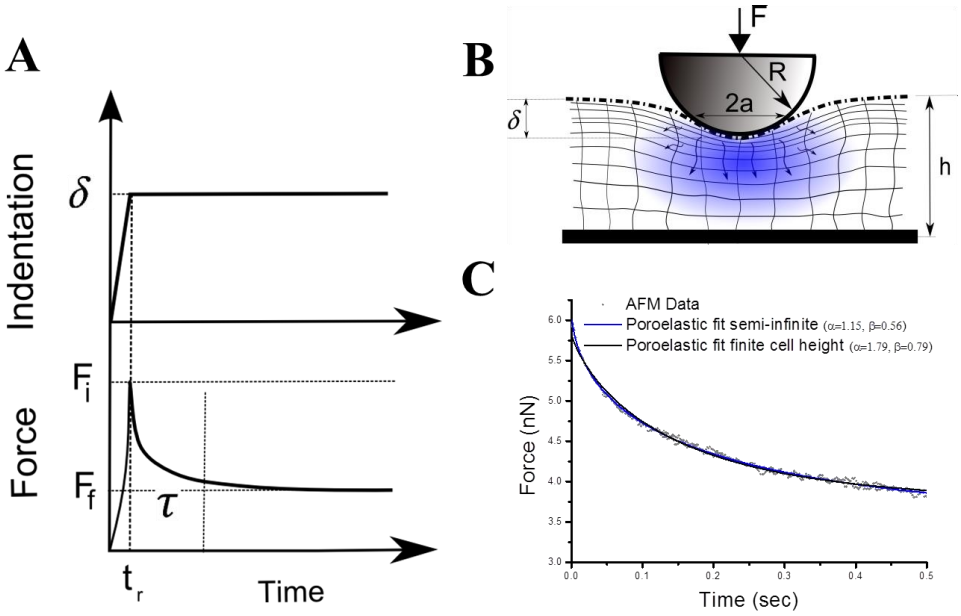

Figure 2-7 Spherical indentation and force relaxation a poroelastic material of finite thickness.

The indentor is pressed into the material until it reaches a target indentation depth of δ. The force required to induce such an indentation depth is F_i applied with a short rise-time of t_r. The applied force F_i relaxes to F_f with the poroelastic characteristic time of τ. (B) Compression of the solid matrix of a poroelastic material with a short rise time $t_r << \tau$, pressurise the interstitial fluid. This pressurisation induces fluid permeation expanding in a semi-spherical shape. The fluid migration can be affected by the substrate and for $h << a$ the shape of expansion changes from a semi-spheroid to a 2D tube. (C) Experimental force-relaxation data (grey dots) fitted with empirical solutions for force-relaxation of poroelastic materials assuming the cell has a finite height (black) or that the cell can be approximated as a semi-infinite half-plane (blue). Both empirical solutions fitted the experimental data well (r^2 > 0.95).

2.5.1 Indentation of a thin layer of poroelastic material

Very recently, detailed finite-element simulations of spherical indentation of thin layers of poroelastic material (Figure 2-7) have been reported [121]. Recalling the Hertz equation (2.17) for indentation of a semi-infinite elastic material, the reactive force on the indentor can be expressed in terms of shear modulus G, Poisson ratio ν and indentation depth δ: $F_{Hertz} = (8/3)GR^{1/2}\delta^{3/2}/(1-\nu)$. For indentation of a poroelastic material of finite thickness, the stress field is influenced by the substrate and thus the above equation can be corrected for the effects of the substrate:

$$F = \frac{8}{3}\frac{G}{1-\nu}R^{1/2}\delta^{3/2}f_p\left(\sqrt{R\delta}/h\right), \tag{2.62}$$

where f_p is solved numerically and takes the following empirical form [121]:

$$f_p\left(\sqrt{R\delta}/h\right) = \frac{0.46 + 0.82\left(\sqrt{R\delta}/h\right) + 2.36\left(\sqrt{R\delta}/h\right)^2}{0.46 + \left(\sqrt{R\delta}/h\right)} \tag{2.63}$$

For infinitely fast indentations ($t_r << \tau$) the fluid does not have enough time to permeate through deformed regions and the poroelastic material behaves as an incompressible elastic material (undrained condition) with the force response of $F_i = \frac{16}{3}GR^{1/2}\delta^{3/2}f_p\left(\sqrt{R\delta}/h\right)$. At long time scales, when the interstitial fluid has fully redistributed (fully drained condition), the force imposed by the indenter is balanced by the stress in the elastic porous matrix only. Under this condition, the force applied for the prescribed indentation is $F_f = \frac{8}{3}\frac{G}{1-\nu_s}R^{1/2}\delta^{3/2}f_p\left(\sqrt{R\delta}/h\right)$. Thus, the Poisson ratio of the solid matrix ν_s determines the ratio of forces at short and long timescales $F_i/F_f = 2(1-\nu_s)$. In intermediate regimes, the fluid permeates through pores and force-relaxation can be approximated in terms of stretched exponential functions:

$$\frac{F(t)-F_f}{F_i-F_f} = \exp\left(-\alpha\tau^{\beta}\right) \tag{2.64}$$

where $\tau = \frac{D_p t}{a^2}$ is the poroelastic characteristic time required for force to relax from F_i to F_f, and α and β are functions estimated empirically from the simulations that depend on the contact radius $a = \sqrt{R\delta}$ and the height h of the layer:

$$\begin{aligned}\alpha &= 1.15 + 0.44(\sqrt{R\delta}\,/\,h) + 0.89(\sqrt{R\delta}\,/\,h)^2 - 0.42(\sqrt{R\delta}\,/\,h)^3 \\ &\quad + 0.06(\sqrt{R\delta}\,/\,h)^4 \\ \beta &= 0.56 + 0.25(\sqrt{R\delta}\,/\,h) + 0.28(\sqrt{R\delta}\,/\,h)^2 - 0.31(\sqrt{R\delta}\,/\,h)^3 \\ &\quad + 0.1(\sqrt{R\delta}\,/\,h)^4 - 0.01(\sqrt{R\delta}\,/\,h)^5.\end{aligned} \tag{2.65}$$

In my experiments, a typical height of h ~ 4.5 μm (at indention point) was measured for HeLa cells and α and β were estimated from the above equations. Fitting experimental force curves with the proposed stretched exponential function indicated that for h > 4.5 μm and δ < 1.4 μm, approximating the cell to an infinite half-plane resulted in a less than 25% overestimation of the poroelastic diffusion constant D_p (Figure 2-7C).

Chapter 3

Materials and Methods

Equation Chapter (Next) Section 1

3.1 Cell culture, generation of cell lines, transduction, and molecular biology

In my experiments, I used three cell lines: cervical cancer HeLa cells, Madin-Darby Canine Kidney epithelial (MDCK) and HT1080 fibrosarcoma cells**.** HeLa cells, HT1080 and MDCK cells were cultured at 37°C in an atmosphere of 5% CO_2 in air in DMEM (Gibco Life Technologies, Paisley, UK) supplemented with 10% FCS (Gibco Life Technologies) and 1% PS. Cells were plated onto 50 mm glass bottomed Petri dishes (Fluorodish, World Precision Instruments, Milton Keynes, UK). For MDCK cells, they were cultured until forming a confluent monolayer. Prior to the experiment, the medium was replaced with Leibovitz L-15 without phenol red (Gibco Life Technologies) supplemented with 10% FCS.

To enable imaging of the cell membrane, we created a stable cell lines expressing the PH domain of Phospholipase Cδ tagged with GFP (PHPLCδ-GFP), a phosphatidyl-inositol-

4,5-bisphophate binding protein that localises to the cell membrane. Briefly, PH-PLCδ-GFP (a kind gift from Dr Tamas Balla, NIH) was excised from EGFP-N1 (Takara-Clontech Europe, St Germain en Laye, France), inserted into the retroviral vector pLNCX2 (Takara-Clontech), and transfected into 293-GPG cells for packaging (a kind gift from Prof Daniel Ory, Washington University [122]). Retroviral supernatants were then used to infect wild type HeLa cells, cells were selected in the presence of 1 $mg.ml^{-1}$ G418 (Merck Biosciences UK, Nottingham, UK) for 2 weeks, and subcloned to obtain a monoclonal cell line. Using similar methods, we created cell lines stably expressing cytoplasmic GFP for cell volume estimation, GFP-actin or Life-act Ruby ([123]; a kind gift of Dr Roland Wedlich-Soldner, MPI-Martinsried, Germany) for examination of the F-actin cytoskeleton, GFP-tubulin for examination of the microtubule cytoskeleton, and GFP-Keratin 18 (a kind gift of Dr Rudolf Leube, University of Aachen, Germany) for visualisation of the intermediate filament network. HT1080 cells expressing mCherry-LifeAct and MDCK cells expressing PHPLCδ-GFP were generated using similar methods. The EGFP-10x plasmid was described in [124] and obtained through Euroscarf (Frankfurt, Germany). Cells were transfected with cDNA using lipofectamine 2000 according to the manufacturer's instructions the night before experimentation[*].

3.2 Fluorescence and confocal imaging

In some experiments, we acquired fluorescence images of the cells being examined by AFM using an IX-71 microscope interfaced to the AFM head equipped with an EMCCD camera (Orca-ER, Hamamatsu, Germany) and piloted using μManager (Micromanager, Palo-Alto, CA). Fluorophores were excited with epifluorescence and the appropriate filter sets and images were acquired with a 40x dry objective (NA = 0.7). For staining of the nucleus, cells were incubated with Hoechst 34332 (1 μg/ml for 5 min, Merck-Biosciences).

[*]The cell lines described in this paragraph were generated with kind help from Dr. Charras.

In some cases, an AFM interfaced with a confocal laser scanning microscope (FV1000, Olympus) was utilized to image the cellular indentation in the zx-plane. Images were acquired with a 100x oil immersion objective lens (NA = 1.4, Olympus). Latex beads attached to AFM cantilevers were imaged by exciting with a 647 nm laser and collecting light at 680 nm. GFP tagged proteins were excited with a 488 nm laser and light was collected at 525 nm. zx-confocal images passing through the centre of the bead were acquired with 0.2 μm steps in z to give a side view of the cell before and after indentation (Figure 3-2D).

3.3 Cell volume measurements

To measure changes in HeLa cell volume in response to osmotic shock, confocal stacks of cells expressing cytoplasmic GFP were acquired at 2 min intervals using a spinning disk confocal microscope (Yokogawa CSU-22, Yokogawa, Japan) with 100x oil immersion objective lens (NA = 1.4, Olympus) and a piezo-electric z-drive (NanoscanZ, Prior, Scientific, Rockland, MA). Stacks consisted of 40 images separated by 0.2 μm and were acquired every 2 min for a total of 30 mins. Exposure time and laser intensity were set to minimize photobleaching. A custom written code in Matlab (Mathworks Inc, Cambridge, UK) was used to process the z-stacks and measure the cell volume at each time step. Briefly, the background noise of stack images was removed, images were smoothed, and binarised using Matlab Image Processing Toolbox functions. Following binarisation, series of erosion and dilatation operations were performed to create a contiguous cell volume image devoid of isolated pixels (Figure 3-1A, B). The sum of nonzero pixels in each stack was multiplied by the volume of a voxel to give a measure of cell volume at each time step. All experiments followed the same protocol: five stacks were captured prior to change in osmolarity and then cell volume was followed for a further 25 minutes (see Figure 5-2A).

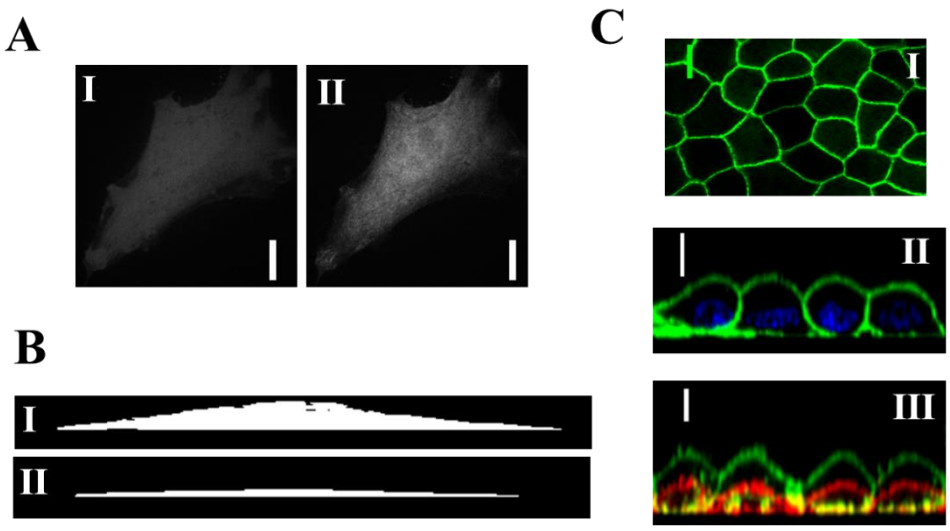

Figure 3-1 Cell volume measurement.

(A, B) The volume of HeLa cells was measured by acquiring fast xyz-t confocal stacks. (A) Image of HeLa cytoplasmic GFP cell showing the bottom of the cell before (I) and after (II) application of hyperosmotic shock induced by PEG-400. The decrease in cell volume increases the concentration of GFP molecules resulting in an increase in fluorescence intensity. (B) Reconstruction of cell profile from confocal z-stacks before I and after II application of PEG-400. (C-I) xy image of MDCK monolayer expressing PH-PLCδ. (C-II) zx section of MDCK cells expressing a membrane marker (PH-PLCδ, green) and stained for nucleic acids with Hoechst 34332 (blue). Nuclei localised to the basal side of cells far from the apex. (C-III) zx profile of MDCK cells before (green) and after (red) application of 500 mM sucrose. Cell height decreased significantly in response to increase in medium osmolarity. Scale bars = 10µm.

The volume of PH-PLCδ MDCK cells in response to osmotic perturbations was estimated by measuring the heights of cell from confocal z-slice images after and before application osmotic shocks (Figure 3-1C). During the osmotic perturbations, I verified that the xy projected area of the cells and the xy positions of cell-cell junctions were not perturbed significantly and therefore measuring the change in cell height was a good approximation for estimating changes in cell volume.

Changes in extracellular osmolarity were effected by adding a small volume of concentrated sucrose, 400-Dalton polyethylene glycol (PEG-400, Sigma-Aldrich, [125]),

or water to the imaging medium. When increasing osmolarity by addition of osmolyte, MDCK cells were treated with EIPA (50 μM, Sigma-Aldrich), an inhibitor of regulatory volume increases [126]. When decreasing the osmolarity by addition of water, the cells were simultaneously treated with the inhibitors of regulatory volume decreases, NPPB (200 μM; Tocris, Bristol, UK) and DCPIB (50 μM, Tocris), to achieve a sustained volume increase [126]. Cells were incubated with these inhibitors for 30 minutes prior to the addition of osmolytes (PEG-400, sucrose or water).

3.4 Disrupting the cytoskeleton

3.4.1 Pharmacological treatments

Cells were incubated in culture medium with the relevant concentration of drug for 30 min prior to measurement. The medium was then replaced with L-15 with 10% FCS plus the same drug concentration such that the inhibitor was present at all times during measurements. Cells were treated with latrunculin B (to depolymerise F-actin, Merck-Biosciences), nocodazole (to depolymerise microtubules, Merck-Biosciences), and paclitaxel (to stabilize microtubules, Merck-Biosciences), and blebbistatin (to inhibit myosin II ATPase, Merck-Biosciences).

3.4.2 Genetic treatments

To examine the effect of uncontrolled polymerization of cytoplasmic F-actin, Dr. Moulding transduced HeLa cells stably expressing Life-act ruby with lentivirus encoding WASp I294T as described in [26]. Lentiviral vectors expressing enhanced GFP fused to human WASp with the I294T mutation were prepared in the pHR'SIN-cPPT-CE and pHR'SIN-cPPT-SE lentiviral backbones as described previously [26, 127]. Lentivirus was added to cells at multiplicity of infection of 10 to achieve approximately 90% transduction.

To examine the perturbations to cytoskeletal proteins, Dr. Charras generated the plasmids described below, and I purified the cDNA and transfected the cells. To examine the effect of uncontrolled polymerisation of tubulin, I transfected HeLa cells with a plasmid encoding γ-tubulin-mCherry, a microtubule nucleator [128, 129]. To disrupt the keratin network of HeLa cells, keratin 14 R125C-YFP (a kind gift from Prof Thomas Magin, University of Leipzig) was overexpressed, a construct that acts as a dominant mutant and results in aggregation of endogenous keratins [130]. To disrupt F-actin crosslinking by endogenous α-actinin, cells were transfected with a deletion mutant of α-actinin lacking an actin-binding domain (ΔABD-α-actinin, a kind gift of Dr Murata-Hori, Temasek Life Sciences laboratory, Singapore). Cells were transfected with cDNA using lipofectamine 2000 the night before experimentation.

3.5 Visualising cytoplasmic F-actin

To visualise cytoplasmic F-actin density, cells were fixed for 15 minutes with 4% PFA at room temperature, permeabilised with 0.1% Triton-X on ice for 5 min, and passivated by incubation with phosphate buffered saline (PBS) and 10 mg/ml bovine serum albumin (BSA) for 10 min. They were then stained with Rhodamine-Phalloidin (Invitrogen) for 30 min at room temperature, washed several times with PBS-BSA, and mounted for microscopy examination on a confocal microscope.

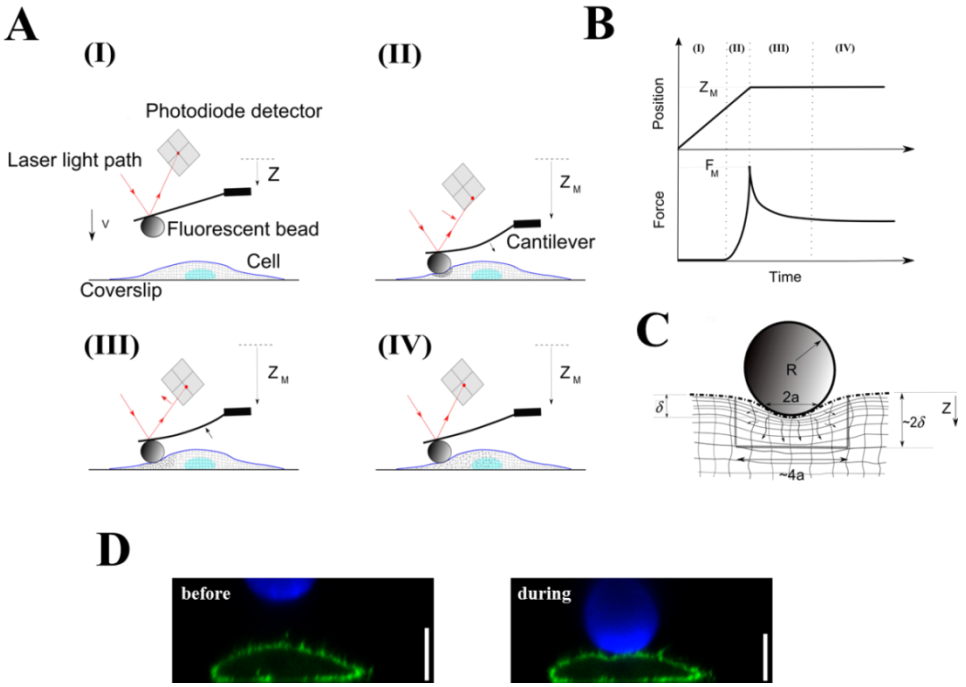

Figure 3-2 AFM experimental setup.

(A) Schematic diagram of the experiment. (A-I) The AFM cantilever is lowered towards the cell surface with a high approach velocity $V_{approach}$ ~ 30 µm.s^{-1}. (A-II) Upon contacting the cell surface, the cantilever bends and the bead starts indenting the cytoplasm. Once the target force F_M is reached, the movement of the piezoelectric ceramic is stopped at Z_M. The bending of the cantilever reaches its maximum. This rapid force application causes a sudden increase in the local stress and pressure. (A-III) and (A-IV) Over time the cytosol in the indented area redistributes inside the cell and the pore pressure dissipates. Strain resulting from the local application of force propagates through the elastic meshwork and at equilibrium; the applied force is entirely balanced by cellular elasticity. Indentation (I-II) allows the estimation of elastic properties and relaxation (III-IV) allows for estimation of the time-dependent mechanical properties. In all panels, the red line shows the light path of the laser reflected on the cantilever, red arrows show the change in direction of the laser beam, black arrows show the direction of bending of the cantilever, and the small dots represent the propagation of strain within the cell. (B) Temporal evolution of the cantilever position and force applied during the experiment. Before the cantilever contacts the cell, no force is applied (I). After contact, force increases until the target force (II). Finally, force relaxes (III) until equilibrium (IV). (C) Schematic drawing showing the zone of indentation. A bead of radius R is pressed into the cell surface creating a depression of radius a and depth $\delta < a$. The compression of the cell surface by the bead induces a pressure increase that squeezes a volume $\sim \delta a^2$ of fluid out of the indentation region (arrows). (D) Z-x confocal image of a HeLa cell expressing PH-PLCδ1-GFP (a membrane marker) corresponding to phases (I) and (IV) of the experiment described in A. The fluorescent bead attached to the cantilever is shown in blue and the cell membrane is shown in green. Scale bar = 10 µm.

3.6 Atomic force microscopy indentation experiments

Force-distance and force-relaxation measurements were acquired with a JPK Nanowizard-I (JPK instruments, Berlin, Germany) interfaced to an inverted optical fluorescence microscope (IX-81 or IX-71, Olympus). For most experiments, AFM cantilevers (MLCT, Bruker, Karlsruhe, Germany) were modified by gluing beads to the cantilever underside with UV curing glue (UV curing, Loctite, UK). Cantilever spring constants were determined prior to gluing the beads using the thermal noise method implemented in the AFM software (JPK SPM, JPK instruments). Prior to any cellular indentation tests, the sensitivity of the cantilever was set by measuring the slope of force-distance curves acquired on glass regions of the petri dish. For measurements on cells, I used cantilevers with nominal spring constants of 0.01 $N.m^{-1}$ and fluorescent latex beads with radii of 7.5 μm (ex645/em680, Invitrogen). For measurements on hydrogels, I used cantilevers with nominal spring constants of 0.6 $N.m^{-1}$ and glass beads with radii of 25 μm (Sigma).

During AFM experiments, the bead on the cantilever was aligned over regions near the cell nucleus and measurements were acquired in several locations in the cytoplasm avoiding the nucleus (except when doing spatial mapping, see section 3.7.5). To maximize the amplitude of stress relaxation, the cantilever tip was brought into contact with the cells using a fast approach speed ($V_{approach}$ > 10 $\mu m.s^{-1}$) until reaching a target force F_M (Figure 3-2A-I, A-II, B). With these settings, force was applied onto the cells in less than 35 ms on average, which is fast compared to the expected poroelastic relaxation time (~0.1-10 s, see Chapter 4 section 1.1). Hence, in the analysis of stress relaxation I assumed that force application was quasi-instantaneous. Upon reaching the target force F_M the piezoelectric ceramic length was kept constant at Z_M and the force-relaxation curves were acquired at constant Z_M (Figure 3-2A-III, A-IV). After 10 s, the AFM tip was retracted with the same speed as the approach.

During force-relaxation measurements, the z-closed loop feedback implemented on the JPK Nanowizard was used to maintain a constant z-piezo height. When acquiring force-relaxation curves with high approach velocities ($V_{approach}$ > 10 µm.s^{-1}), the first 5 ms of force-relaxation were not considered in the data analysis due to the presence of small oscillations in z-piezoelectric ceramic height immediately after contact due to the PI feedback loop implemented in the JPK software. When acquiring force-relaxations curves for averaging over multiple cells, I used approach velocities $V_{approach}$ ~ 10 µm.s^{-1} that did not give rise to oscillations in length of the z-piezoelectric ceramic.

3.6.1 Measuring indentation depth and cellular elastic modulus

The approach phase of the AFM force-distance curves (Figure 3-3) was analysed to extract the bulk elastic modulus E, which is linearly related to the shear modulus G through the Poisson ratio via equation (2.4); $E = 2G(1+\nu)$. During indentation (after contact) the force the cantilever is related to the cell stiffness and the deflection of the cantilever Δd by

$$F = k_c \Delta d = k_c (d - d_0), \tag{3.1}$$

where k_c is the cantilever's spring constant, d is the deflection of cantilever (correlated to changes in reflection of AFM laser beam which is detected by photo-detector), and d_0 is the deflection offset at the point of contact where the force is zero.

The indentation depth δ is calculated by subtracting the cantilever deflection Δd from the piezo translation Δz

$$\begin{aligned} \delta = \Delta z - \Delta d &= (z - z_0) - (d - d_0) \\ &= (z - d) - (z_0 - d_0) = w - w_0, \end{aligned} \tag{3.2}$$

where z_0 is the translation of the piezo at the contact point, $w = (z - d)$ and $w_0 = z_0 - d_0$ are the transformed variables. E was then estimated by fitting the force-indentation data with a Hertzian contact model between a sphere and an infinite half

space (equation (2.17)). In this framework, the relationship between the applied force F and the indentation depth δ is:

$$F = \frac{4}{3}\frac{E}{1-\nu^2}R^{1/2}\delta^{3/2}. \tag{3.3}$$

with ν the Poisson ratio, and R the radius of the spherical indenter. The above Hertz model of indentation can be used to compute the elastic modulus of a linear elastic material of infinite thickness (see Chapter 2.1.1). To limit the effects of finite cell thickness, in my analysis I only considered the force-indentation/relaxation curves in which the indentation depths were less than 25% of the cell height. This ensures errors of less than 20% in the estimation of the elastic modulus (see equation 2.63) in my experiments. To use the Hertz model in this work I assumed the cell to be a isotropic, homogeneous and linear elastic materials and the contact surfaces were assumed to be frictionless and non-adhesive [131]. Although these assumptions are not fully accurate for indentation of adherent cells, the Hertz model is still widely used for characterisation of cells and soft materials providing fairly accurate measurements of elastic modulus [132].

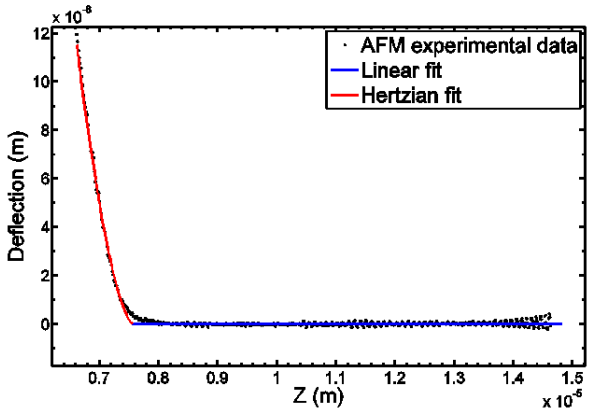

Figure 3-3 AFM force-distance curve.

The approach phase of AFM force-distance curve (Figure 3-2A-I and II). The force distance AFM data (dotted points) is fitted with two linear (blue line) and nonlinear (red line) curves for the noncontact and contact portions of the curve respectively. The contact point is estimated by choosing the point that minimises the total mean square error of the fitted curves.

Together with equations (3.1) and (3.2), contact mechanics models (like equation (3.3)) can be fit to AFM indentation data. However the main challenge in analysing AFM force-distance curves is to design an automated routine to find the correct contact point which enables us to compute the indentation depth. The contact point between the cell and the AFM tip was estimated using the method described in [133] implemented in our laboratory, see Figure 3-3. In brief, as a first step the force distance-curve is transformed into a d-w curve introducing the variable $w = (z - d)$. Then our custom written Matlab code marches along all points of the d-w curve, and assumes each point is the potential contact point. Considering (w_0^i, d_0^i) as the contact point, at each iteration i the initial portion of the curve (assumed to be the noncontact region) was fitted with a line while the latter portion (assumed to be the portion of the curve in contact) was fitted with a power function as in equation (3.3):

$$(d - d_0^i) = b^i (w - w_0^i)^{3/2}, \tag{3.4}$$

where b^i is the sole fitting parameter. The total mean square error (MSE) from both fits was calculated and the contact point (w_0^n, d_0^n) was chosen as the point where the total MSE reaches its minimum value at $i = n$ with $b^n = 4ER^{1/2} / \ 3(1-\nu^2)k_c$ (see Figure 3-3).

Comparing the long time-scale and short time-scale limits allows for estimation of the Poisson ratio of the solid matrix; $F(0) / F(\infty) = 2(1-\nu_s)$. However for cellular indentations the force relaxation curves do not reach a relaxation plateau for estimation of $F(\infty)$ and thus for estimation of the elastic modulus, I assumed a Poisson ratio of ν_s =0.3.

3.6.2 Measurement of the poroelastic diffusion coefficient

A brief description of the governing equations of linear isotropic poroelasticity and the relationship between the poroelastic diffusion constant D_p, the shear modulus G, and

hydraulic permeability K are given in Chapter 2 section 3. To experimentally measure the cellular poroelastic properties, I monitored stress-relaxation following rapid local application of force by AFM microindentation (Figure 3-3, Figure 3-4 and Figure 5-1A). I analysed my experiments as force-relaxation in response to a step displacement of the cell surface. No closed form analytical solution for indentation of a poroelastic infinite half space by a spherical indentor exists. However, an approximate solution obtained by FE simulations gives [120]:

$$\frac{F(t)-F_f}{F_i-F_f} = 0.491\,\mathrm{e}^{-0.908\sqrt{\tau}} + 0.509\,\mathrm{e}^{-1.679\tau}, \tag{3.5}$$

where $\tau = D_p t/(R\delta)$ is the characteristic poroelastic time required for force to relax from F_i to F_f. Cells have a limited thickness h and therefore the infinite half-plane approximation is only valid at time-scales shorter than the time needed for fluid diffusion through the cell thickness: $t_{hp} \sim h^2 / D_p$. As we shall see in the next chapters, in experiments on HeLa cells, I measured h ~ 5 µm and D_p ~ 40 µm^2.s^{-1} setting a time-scale t_{hp} ~ 0.6 s. I confirmed numerically that for times shorter than ~ 0.5 s, approximating the cell to a half-plane gave errors (calculated by comparing the half space approximation and the finite thickness solution) of less than 20% (Figure 2-5 and Figure 2-7C). For short time-scales, both terms in equation (3.5) are comparable and hence as a first approximation, the relaxation scales as $\sim e^{-\tau}$. Equation (3.5) was utilized to fit our experimental relaxation data, with D_p as single fitting parameter and I fitted only the first 0.5 s of relaxation curves to consider only the maximal amplitude of poroelastic relaxation and minimise errors arising from finite cell thickness.

3.6.3 Determining the apparent cellular viscoelasticity

To determine the single phase viscoelastic parameters, I modelled cells using a standard linear model consisting of a spring-damper (stiffness k_1 and apparent viscosity η) in parallel with another spring (stiffness k_2), as described in [53] (see Figure 2-2). In this

model, the applied force decays exponentially when the material is subjected to a step displacement at t = 0:

$$\frac{F(t) - F_f}{F_i - F_f} = e^{-\frac{k_1 t}{\eta}}. \tag{3.6}$$

The spring constant k_1 scales with the elastic modulus $k_1 \sim E$ (estimated from approach phase of indentation tests) and therefore the experimental force relaxation curves were fitted using equation (3.6), with η as the sole fitting parameter.

3.6.4 Measuring cell height

To measure cell height at each contact point, I collected a force-distance curve on the glass substrate next to the cell being examined. The z_0 calculated from the force-distance curve on the glass was used as a height reference. As shown in Figure 3-4, at each indentation point, the cell height was estimated by subtracting the z_0 of the cell from the reference z_0.

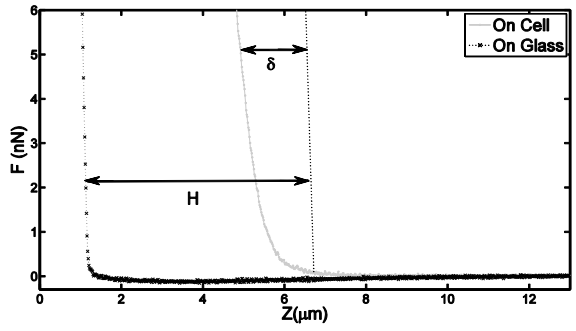

Figure 3-4 Calculating the height of cell at contact point.

A force-distance curve acquired on the glass substrate next to the cell examined was used as the reference to estimate the height of the cell at the contact point

3.6.5 Spatial probing of cells

To investigate spatial variations in the cellular poroelastic properties, I acquired measurements at several locations on the cell surface along the long axis of the cell with a target force of F_M = 4 nN. To locate indentation points in optical images of the cell, a fluorescence image of the bead resting on the glass surface close to the cell was acquired, and the centre of the bead was used as a reference point. This reference point was used to estimate the height of the cell for each measurement, as well as the position of indentation on the cell surface, the xy-coordinates of each stress relaxation measurement being known from the AFM software. The position of the measurement point relative to the nucleus was estimated by acquiring a fluorescence image of the nucleus and calculating the centre of mass of the nucleus (see Figure 3-5). This also enabled us to know whether the measurement point was above the nucleus or not.

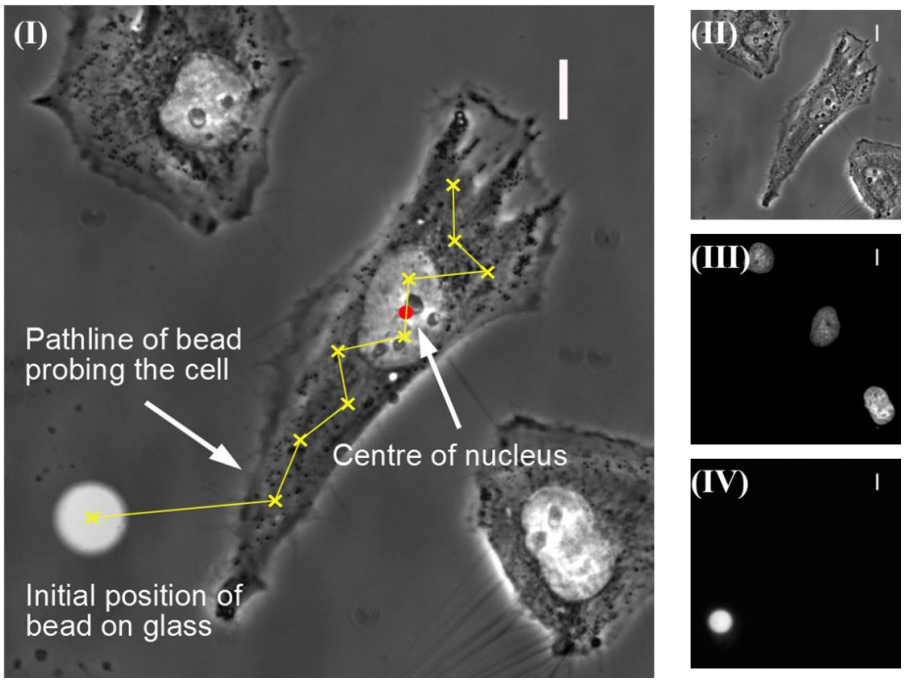

Figure 3-5 Spatial AFM measurement

(I) Representative phase contrast image of a HeLa cell and the location of AFM measurements on its surface. The position of the height reference, where the AFM tip contacts the glass surface was also chosen as the xy reference (fluorescence image of the bead, IV). The location of the nucleus was determined using Hoechst 34332 staining and the centroid of the nucleus (red dot in I) was used as a reference for displaying the measured properties. To determine the exact pathline of the bead and to calculate the distance of each point from the centre of nucleus, images of the cell (II), the cell nucleus (III), and the bead (IV) were overlaid (I). Scale bars = 10 μm.

3.7 Microinjection and imaging of quantum dots

PEG-passivated quantum dots (qdots 705, Invitrogen) were diluted in injection buffer (50 mM potassium glutamate, 0.5 mM MgCl2, pH 7.0) to achieve a final concentration of 0.2 μM and microinjected into HeLa cells as described in [134]. Quantum dots were imaged on a spinning disk confocal microscope by exciting at 488 nm and collecting emission above 680 nm. To qualitatively visualize the extent of quantum dot movement, time series were projected onto one plane using ImageJ.

3.8 Rescaling of force relaxation curves

Plotting the obtained experimental relaxation curves in different scale coordinates and/or normalising them in different ways can provide useful insights into the functional nature of these curves. For instance it is difficult to differentiate between exponential relaxation curves and weak power law curves unless the curves are plotted in log-log coordinates. Furthermore, to differentiate between poroelastic and viscoelastic responses during indentation tests several methods for normalisation of relaxation curves have been proposed [120, 135-137]. One successfully applied method is based on the collapse of normalised force relaxation curves acquired with different indentation depths onto a single master curve [137]. Prompted by this, I have proposed the following more general force normalisation method:

$$\frac{F(t)-F(t=t^*)}{F(t=0)-F(t=t^*)}, \tag{3.7}$$

where t^* can be any arbitrary time. Let us consider that the force relaxation is decaying function of the form $F(t)=F(t,\tau_1,\tau_2,...,\tau_n)$ that is a function of a number of (finite or infinite) characteristic relaxation times τ_i. For force relaxation curves acquired with different indentation depths, if the characteristic relaxation times (or in general the decay function F) do not have any form of functional dependency on indentation depth (as during linear viscoelastic or power law responses), force normalisation using equation (3.7) results in the collapse of all the relaxation curves onto a single curve. In contrast, the characteristic relaxation time in poroelastic materials depends on the indentation depth and force-normalisations alone will not result in collapse of curves onto a single master curve.

Considering the spherical indentation of a purely poroelastic material, the force relaxation can be written in the form $F(t)=[F(0)-F(\infty)]P(D_p t / R\delta)+F(\infty)$ where P is the poroelastic response function (decaying in an exponential manner from 1 at $t=0$ to 0 at $t=\infty$) and $F(0)$ and $F(\infty)$ are the forces at very short (t = 0+) and very long (t = ∞)

timescales, respectively. For any given indentation depth δ, using the normalisation in equation (3.7) results in:

$$\frac{F(t)-F(t=t^*)}{F(t=0)-F(t=t^*)}=\frac{P(D_p t/R\delta)-P(D_p t^*/R\delta)}{1-P(D_p t^*/R\delta)} \tag{3.8}$$

To obtain collapse of force relaxation curves onto a single master curve for any t^* using the above equation time must be rescaled with indentation depth. First, t^* must be selected so that it is proportional to the indentation depth δ specific to each curve: $t^*=\alpha\delta$ where α (with unit of s. μm^{-1}) is an arbitrary number fixed for all curves. Then rescaling of time with respect to indentation depth (t/δ), leads to collapse of all experimental curves onto one master curve.

Note that, if the chosen t^* is such that $t^* >> \tau = R\delta/D_p$, then the force relaxation curve reaches a plateau: $F(t)\to F(\infty)$ and $P(D_p t^*/R\delta)\to 0$ and equation (3.7) becomes:

$$\frac{F(t)-F(t=t^*)}{F(t=0)-F(t=t^*)}=P(D_p t/R\delta), \tag{3.9}$$

and therefore rescaling of time with respect to indentation depth (t/δ), is sufficient to obtain collapse of all relaxation curves as in [137].

3.9 Polyacrylamide hydrogels

For comparison with cells, I acquired force-relaxation measurements on polyacrylamide (PAAm) hydrogels, which are well-characterised poroelastic materials. For the measurements, we made gels of 15% acrylamide-bis-acrylamide crosslinked with TEMED and ammonium persulfate following the manufacturer's instructions (Bio-Rad, UK).

3.10 Particle tracking using defocused images of fluorescent beads

Optical images of fluorescent beads acquired by wide-field microscopy can exhibit different shapes depending on the distance between the bead and the plane of focus. The in-focus image of a bead is a spot with a certain diameter, while when the plane of focus is away from the bead centre by a distance of a few micrometres, sets of concentric rings are visualised (see Figure 3-6A). The z-distance of the particle from the imaging plane is precisely correlated to the radius of the outer ring. As a very simple 3D particle tracking technique, calculating the centre and radius of the outer ring over several frames over time can provide a very precise means for tracking the coordinates of a bead: (x, y, z, t) [138]. This technique is presented in Chapter 4.2 and was employed to study the swelling/shrinking kinetics of cell (Figure 4-7).

3.10.1 Experimental protocol and calibration setup

Yellow-Green carboxylate-modified fluorescent microspheres 0.5 µm in diameter (FluoSpheres, Molecular Probes, Invitrogen) were coated with collagen-I following the protocol suggested by the manufacturer. To attach beads to the cell membrane prior to experiments, Life-act ruby HeLa cells were incubated for ~ 30 min with a dilute solution (100x dilution) containing fluorescent collagen coated beads.

A Piezo-electric z-stage (NanoscanZ, Prior, Scientific, Rockland, MA) was used to calibrate defocused images and to estimate the height of the cell at the location of the attached beads (Figure 3-6). The z-stage was fixed on top of the optical fluorescence microscope stage (IX-71, Olympus) and was piloted using µManager (Micromanager, Palo-Alto, CA) to step up/down while taking epifluorescence images. To find the relationship between the z-positions of a bead and the radius of the outer rings formed in the defocused images, fluorescence z-stack images of the bead with a step size of 100 nm were acquired. To measure the poroelastic diffusion constant using equation (4.6), the height of the bead also needed to be determined. For this, the z-position of the bead with

respect to the bottom of the cell was estimated by acquiring fluorescence z-stack images of Lifeact-Ruby HeLa cells with step size of 200 nm over large distances (~ 10 µm, starting from a few micrometres above the cell and ending a few micrometres below the cell-glass interface). The height of the cell was measured as the distance between the plane that shows an in-focus image of the stress fibres at the bottom of the cell and the plane focused on the bead (Figure 3-6D).

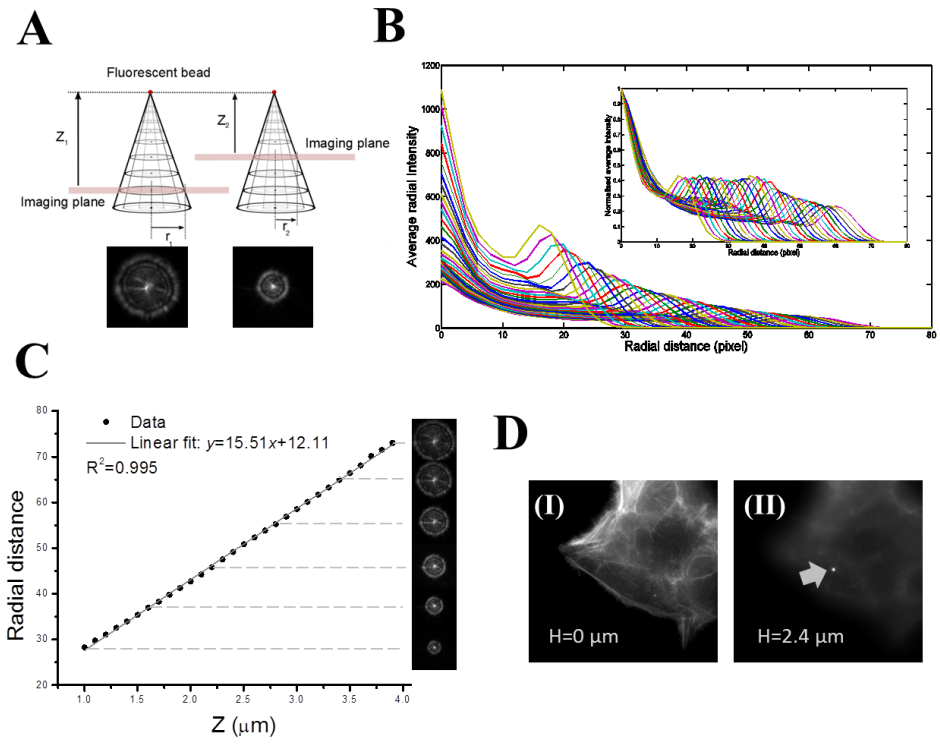

Figure 3-6 High resolution defocusing microscopy of fluorescent bead.

(A) Images of a 500 nm fluorescent bead attached to the cell membrane taken at different distances from bead centre appears as concentric rings. The radius of the outermost ring in the image can be related to the distance between the bead centre and the plane of imaging. (B) The averaged radial intensity curves calculated when the imaging plane is moved in 100 nm increments away from the bead focal plane. The radius of outer rings can be estimated using these curves. Inset is the normalised averaged radial intensity curves. To determine the radius of outer rings, the peak of each curve can be fitted with a Gaussian function. (C) The radial position of the outer ring is linearly related to the distance between the imaging plane and the bead focal plane. Using this concept the z-position of a particle can be tracked with very high accuracy (~ 10 nm). (D) The height of a bead attached to the cell is estimated by focusing on the bottom of the dish in (I) where stress fibres are in focus, and on the bead attached to the cell membrane in (II).

3.10.2 Radial projection

The 2D defocused images of a bead are circularly symmetric so a 1D radius function was used to detect the radius of the outer ring in each defocused image. Since there were several beads attached to the cell membrane, the rough central position of the bead of interest was selected visually and then the precise coordinates of the centroid of the chosen bead (x_c, y_c) were estimated by fitting a 2-D Gaussian function to the image. An arbitrary annulus interval Δ was set to generate a radial distance vector $r_i = i\Delta,\ i = 0...N$. By knowing the precise centre of the image, the distance of each pixel in the image from the centroid was estimated. According to the radial distance of each pixel d, there are total of P_i pixels lying between radii r_{i-1} and r_{i+1}. For each pixel within the annulus between radii r_{i-1} and r_{i+1} the averaged radial intensity vector $\mathrm{I}_R(r_i)$ (see Figure 3-6B) was calculated by splitting the intensity of each pixel I in this annulus linearly according to its radial position d:

$$\mathrm{I}_R(r_i) = \frac{1}{\sum_{n=1}^{P_i} w_n} \sum_{n=1}^{P_i} w_n I_n$$
$$w_n = \begin{cases} \dfrac{d - r_{i-1}}{\Delta} & if\ \ r_{i-1} \le d < r_i \\ \dfrac{r_{i+1} - d}{\Delta} & if\ r_i \le d < r_{i+1}. \end{cases} \tag{3.10}$$

To find an estimate with sub-pixel resolution for the radial position of the outer rings, two approaches were implemented. In the first approach the radius of the outer ring was calculated by finding the position of the outer peak in the averaged radial intensity curve (using an inbuilt Matlab function) and fitting a rotationally symmetric Gaussian function to the intensity curve neighbouring this point. In the second approach the averaged radial intensity curve was normalised to its maximum intensity as shown in the inset of Figure 3-6B and the intersection of the curve with the line y = 0.05 provided an estimate for the radial position of the ring where the intensity of the outer ring diminishes to zero.

3.11 FRAP experiments

I performed the fluorescence recovery after photobleaching (FRAP) experiments described in the following with kind help from Marco Fritzsche. FRAP experiments were performed using a 100x oil immersion objective lens (NA = 1.4, Olympus) on a scanning laser confocal microscope (Olympus Fluoview FV1000; Olympus). Fluorophores including GFP-tagged proteins and CMFDA (a small cytoplasmic fluorescent probe, 5-chloromethylfluorescein diacetate, Celltracker Green, Invitrogen) were excited at a wavelength of 488 nm. For experiments with CMFDA, cells were incubated with 2 µM CMFDA for 45 min before replacing the medium with imaging medium. For experiments with cytoplasmic GFP or EGFP-10x, cells were transfected with the plasmid of interest the day before experimentation. To obtain a strong fluorescence signal and minimize photobleaching, a circular region of interest (ROI, 1.4 µm in diameter) in the middle of the cytoplasm was imaged, setting the laser power to 5% and 1% of the maximum output (488nm wave length, nominal output of 20mW) for GFP and CMFDA, respectively. Each FRAP experiment started with five image scans to normalise intensity, followed by a 1s bleach pulse produced by scanning the 488nm laser beam line by line (at 100% power for GFP and 25% power for CMFDA) over a circular bleach region of nominal radius r_n = 0.5 µm centred in the middle of the imaging ROI. To sample the recovery sufficiently fast, an imaging ROI of radius of 0.7 µm was chosen allowing acquisition of fluorescence recovery with a frame rate of 50 ms per frame.

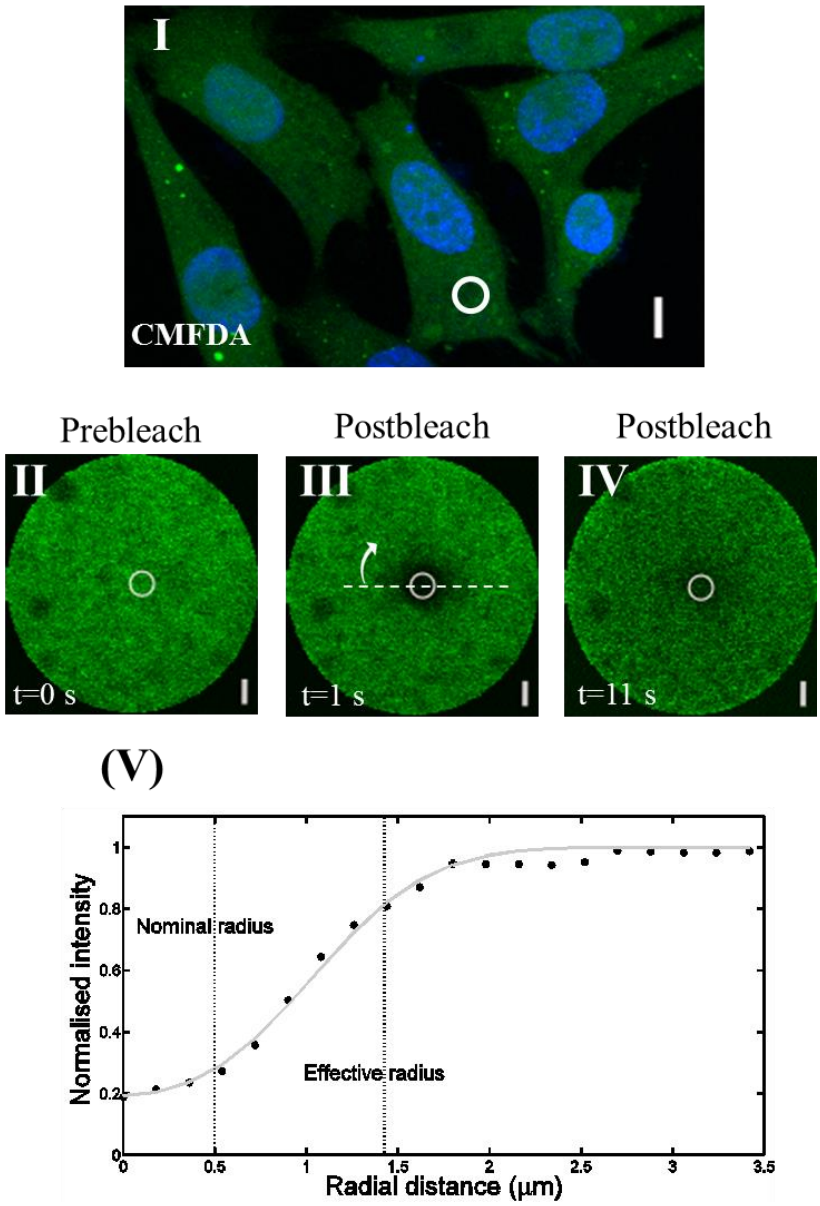

Figure 3-7 Estimation of the effective bleach radius in HeLa cells FRAP experiments.

(I) Confocal image of cells loaded with the cytoplasmic indicator CMFDA (green). Nuclei (blue) were stained with Hoechst 34332. Scale bar = 10 µm. (II-III-IV) Time series of a photobleaching experiment in the cytoplasm of the cells shown in (I, indicated by the white circle). The white circle in images (II-IV) denotes the nominal photobleaching zone. In all three images, scale bars = 1 µm. (II) shows the last frame prior to photobleaching. (III) shows the first frame after photobleaching. The bleached region is clearly apparent and larger than the nominal photobleaching zone. (IV) After a long time interval, fluorescence intensity re-homogenises due to diffusion. (V) Fluorescence intensity immediately after photobleaching in the cytoplasm centred on the photobleaching zone in frame (III). Fluorescence was normalised to the intensity far away from the photobleaching zone.

3.11.1 Effective bleach radius

Most experiments were carried out on cytoplasmic fluorophores. Because of their rapid diffusion within the cytoplasm during the bleaching process, the effective radius over which photobleaching takes place (r_e) is larger than the nominal radius (r_n). In my experiments to measure the translational diffusion coefficient D_T precisely, I needed to first determine r_e. To experimentally estimate the effective radius r_e, I performed a separate series of FRAP experiments on cells loaded with CMFDA in hyperosmotic conditions. An imaging area larger than the effective photobleaching radius (4 μm in diameter) was empirically chosen and photobleaching recovery in this area was imaged with a frame rate of 0.2 s/frame. Next, using a custom written Matlab program, I calculated the radial projection profile of the fluorescence intensity in the imaging region for the first postbleach image $I(r, t = 1)$ and then fitted the experimental intensity profile with the bleach equation for a Gaussian laser beam to determine r_e (Figure 3-7):

$$I(r) = \exp\left(-K \exp\left(-2\frac{r^2}{r_e^2}\right)\right), \tag{3.11}$$

where r is the radial distance from the center of bleach spot and K is the bleaching constant related to the intensity of the bleaching laser and the properties of the fluorophore.

3.11.2 FRAP analysis

FRAP recovery curves $I(t)$ were obtained by normalising the mean fluorescence intensity within the nominal bleach area for each frame to the average fluorescence intensity of the first prebleach image. The translational diffusion coefficient D_T was estimated using the model for a uniform-disk laser profile and ideal bleach [139, 140] following the methods described in [141]:

$$I_n(t) = \exp\left(-\frac{r_e^2}{8D_T t}\right)\left[I_0\left(\frac{r_e^2}{8D_T t}\right) + I_1\left(\frac{r_e^2}{8D_T t}\right)\right], \tag{3.12}$$

where $I_n(t) = I(t) / I(\infty)$ is the normalized fluorescence intensity in the bleached spot as a function of time t, r_e is the effective bleach radius, I_0 and I_1 are modified Bessel functions. In the experimentally acquired FRAP curves, the first post-bleach value $I_n(t = 1\,s)$ was larger than zero (Figure 5-4 and Figure 5-5B, C), something that could be due to rapid fluorophore diffusion during the bleach process or incomplete weak bleaching [141]. In cells exposed to hyperosmotic conditions, the intensity of the first post-bleach time point was over 30% lower than in isoosmotic conditions, suggesting that the non-zero value of this first time point was due to rapid diffusive recovery. Based on this observation, we assigned a timing of $t_0 = 0.1$ s to the first post bleach time point when fitting fluorescence recovery curves. The validity of the fitting was verified by comparing the translational diffusion constant of GFP and CMFDA estimated with our technique to previously published values.

3.11.3 Estimation of cortical F-actin turnover half-time

To assess the turnover rate of the F-actin cytoskeleton, HeLa cells stably expressing actin-GFP were blocked in prometaphase by overnight treatment with 100 nM nocodazole. Under these conditions, cells form a well-defined actin cortex. To estimate F-actin turnover, photobleaching was performed on the F-actin cortex and recovery was imaged at a frame rate of 0.9s/frame (Figure 5-4B).

3.12 Data processing, curve fitting and statistical analysis

Indentation and stress relaxation curves collected by AFM were analysed using custom written code in Matlab (Mathworks Inc, Cambridge, UK). Data points where the indentation depth δ was larger than 25% of cell height were excluded. Goodness of fit was evaluated by calculating r^2 values and for analyses only fits with r^2 > 0.85 were considered (representing more than 90% of the collected data). The calculated value for

each group of variables is presented in terms of mean and standard deviation (Mean±SD). To test pairwise differences of population experiments, the student's *t*-test was performed between individual treatments. Values of $p < 0.01$ compared to control were considered significant and are indicated by asterisks in the graphs.

Chapter 4

The cytoplasm of living cells behaves as a poroelastic material

Equation Chapter (Next) Section 1

The cytoplasm of living cells is constituted of a porous elastic solid meshwork (cytoskeleton, organelles, macromolecules, etc) bathing in an interstitial fluid (cytosol) (see Figure 1-1 and Figure 1-10A). Based on this description, it is not very surprising that the cytoplasm has many hydrogel-like characteristics. Hydrogels, an aggregate of cross-linked polymer network and water molecules, are ubiquitous in nature and especially in biological tissues. One of the main characteristics of hydrogels is that their mechanical response is manifested through concurrent interaction of the solid network and the fluid phase. In such fluid-filled sponges, the rate of relaxation is limited by the rate at which interstitial fluid can redistribute within the solid network. As briefly described in Chapter 2.3, the Biot theory of poroelasticity has been applied to study the rheology of fluid-infiltrated porous elastic solids. In this chapter, two different experimental approaches are utilized to examine the poroelastic behaviours of cytoplasm and compare it to hydrogels.

First, by employing AFM micro indentation tests acquired on cells and hydrogels, the functional form of force-relaxation curves at different timescales was examined. Then the idea of poroelastic cytoplasm is validated by comparing the force relaxation curves acquired on cells with those acquired on hydrogels as these are well-characterized poroelastic materials. Second, to further test the poroelastic behaviour of cytoplasm, the rheology of cells in response to different types of osmotic perturbation were studied and the swelling/shrinking kinetics of cytoplasm were investigated in the framework of poroelasticity.

4.1 Indetation test for characterisation of poroelastic material

4.1.1 Establishing the experimental conditions to probe poroelasticity

First, I established the experimental conditions under which water redistribution within the cytoplasm (or hydrogel) might contribute to force-relaxation. In our experiments (Figure 3-2), following rapid indentation with an AFM cantilever (3.5-6nN applied during a rise time t_r ~ 35ms resulting in typical cellular indentation of δ ~ 1µm), force decreased by ~ 35% whereas indentation depth only increased by less than ~ 5%, therefore our experiments measure force-relaxation under approximately constant applied strain (Figure 4-1A). Relaxation in poroelastic materials is due to water movement out of the porous matrix in the compressed region (Figure 2-7B, Figure 3-2C). The time-scale for water movement is $t_p \sim L^2 / D_p$ (L is the length-scale associated with indentation[120]: $L \sim \sqrt{R\delta}$ with R the radius of the indenter) and therefore poroelastic relaxation contributes significantly if the rate of force application is faster than the rate of water efflux: $t_r << t_p$. Previous experiments estimated D_p ~ 1-100 µm^2.s^{-1} in cells [100, 101] yielding a characteristic poroelastic time of t_p ~ 0.1-10 s, far longer than t_r. Hence, if intracellular water redistribution is important for cell rheology, force-relaxation curves should display characteristic poroelastic signatures for times up to t_p ~ 0.1-10 s.

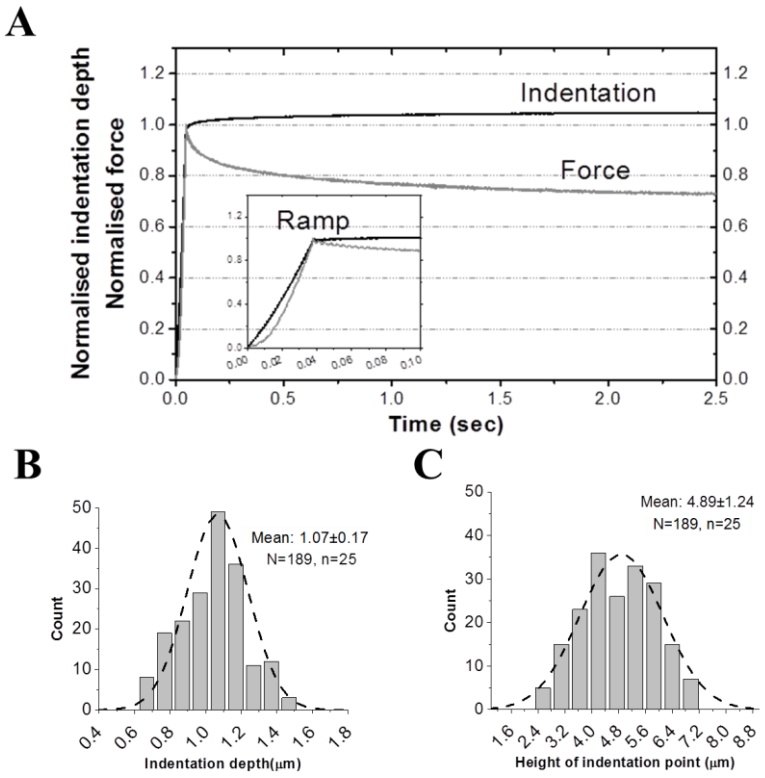

Figure 4-1 Stress relaxation of HeLa cells in response to AFM microindentation

(A) Temporal evolution of the indentation depth (black) and the measured force (grey) in response to AFM microindentation normalized to their values when the target force is reached. Inset: approach phase from which the elasticity is calculated (grey curve). The total approach time lasts less than 50 ms. (B) cell height distribution at the indentation point. (C) Indentation depth distribution. In B and C, N indicates the total number of measurements and n indicates the number of cells.

For hydrogels similar to the ones that were used in our experiments, poroelastic diffusion constants of D_p ~ 100 μm^2.s^{-1} have been reported [137]. Considering this estimate, applying indention depths of δ ~ 2 μm with the same size indentors as for cells (radius of 7.5 μm) would give characteristic poroelastic times t_p < 0.1 s, too fast to accurately observe poroelastic effects, given a rise times of t_r ~ 0.1 s. Therefore to be able to reliably observe poroelastic effects, I used a larger indentor (radius of R = 25 μm). Using this larger indentor with δ ~ 2 μm gave an expected characteristic poroelastic time of t_p > 0.5 s much larger than the experimental rise time t_r.

4.1.2 Poroelasticity is the dominant mechanism of force-relaxation in hydrogels

To test our rescaling strategies on hydrogels, force-indentation and force relaxation curves were acquired on hydrogels by setting target forces of 40, 80 and 140 nN as shown in Figure 4-2. For each set of target forces, 20 replicate measurements were performed on a 100 μm × 100 μm area of the gel and the relaxation curves were averaged for each time point. Analysis of force indentation curves for each set of target forces respectively yields indentation depths of 1.99±0.02 μm, 2.77±0.03 μm and 3.86±0.06 μm and not significantly different elastic moduli of 1.8±0.05 kPa, 1.9±0.06 kPa and 2±0.1 kPa. Figure 4-2B shows the plot of force relaxation curves in log-log coordinates which displays two clear plateaus at very short and at very long time scales for each set of curves. The long timescale plateau indicates that the force relaxation in the gel has a clear characteristic relaxation time. Furthermore these curves show that force relaxation in these hydrogels does not exhibit a power law behaviour.

One hallmark of poroelastic materials is that their characteristic relaxation time $t_p \sim R\delta / D_p$ is dependent on the indentation depth δ. In contrast, power law relaxations of the form $F(t) \sim F_0(t / t_0)^{\beta}$ and exponential relaxations of the form $F(t) \sim F_0 \exp(-t / \tau)$ have parameters β and τ that are independent of length scale. For ideal stress-relaxations of any power-law or linear viscoelastic material, normalisation of force between any two arbitrarily chosen times t_1 and t_2 $[F(t) - F(t_1)] / [F(t_2) - F(t_1)]$ should lead to collapse of all experimental relaxation curves onto one master curve. However, for poroelastic materials, force normalisation alone is not sufficient to collapse curves onto a single master curve and time must also be renormalised with respect to the indentation depth to achieve collapse of curves.

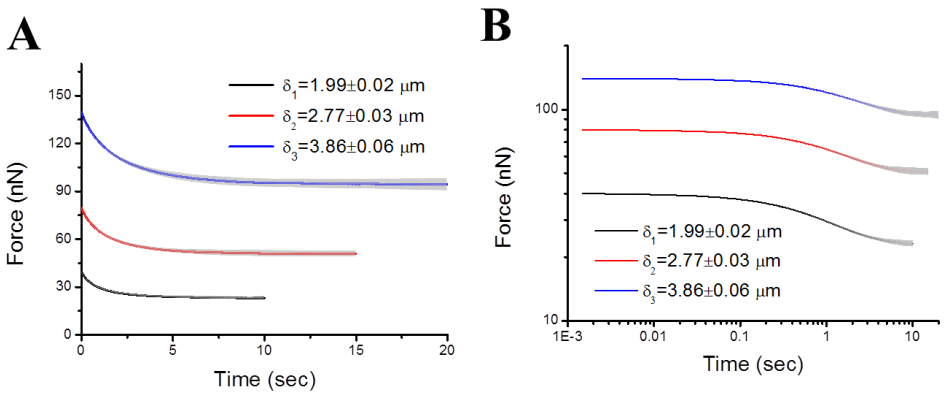

Figure 4-2 Force-relaxation curves acquired with different indentation depths on hydrogel.

(A) Force-relaxation curves acquired on a hydrogel for three different indentation depths (δ_1, δ_2 and δ_3). Each data point is the average of 20 measurements acquired at different positions on the hydrogel surface. (B) log-log plot of the curves shown in (A). Curves show characteristic plateaus at short and long time-scales. In all graphs, solid lines and grey shadings represent the mean and standard deviations at each data point, respectively.

To distinguish between poroelastic and viscoelastic force-relaxations, I undertook a rescaling analysis as explained in Chapter 3.8. First the force was normalised according to equation (3.7) up to the time when each curve reaches its final plateau ($t^* = t_\infty$). As shown in Figure 4-3A, normalisation of force alone did not result in the collapse of curves onto a single master curve. If the gel were a linear viscoelastic material, normalisation of force in this way should result in collapse of all curves onto a single curve irrespective of indentation depth. However, if in addition to force, time is also normalised by indentation depth, all experimental curves collapse onto a single curve, indicating that poroelasticity is the dominant mechanism of force relaxation in hydrogels (Figure 4-3B).

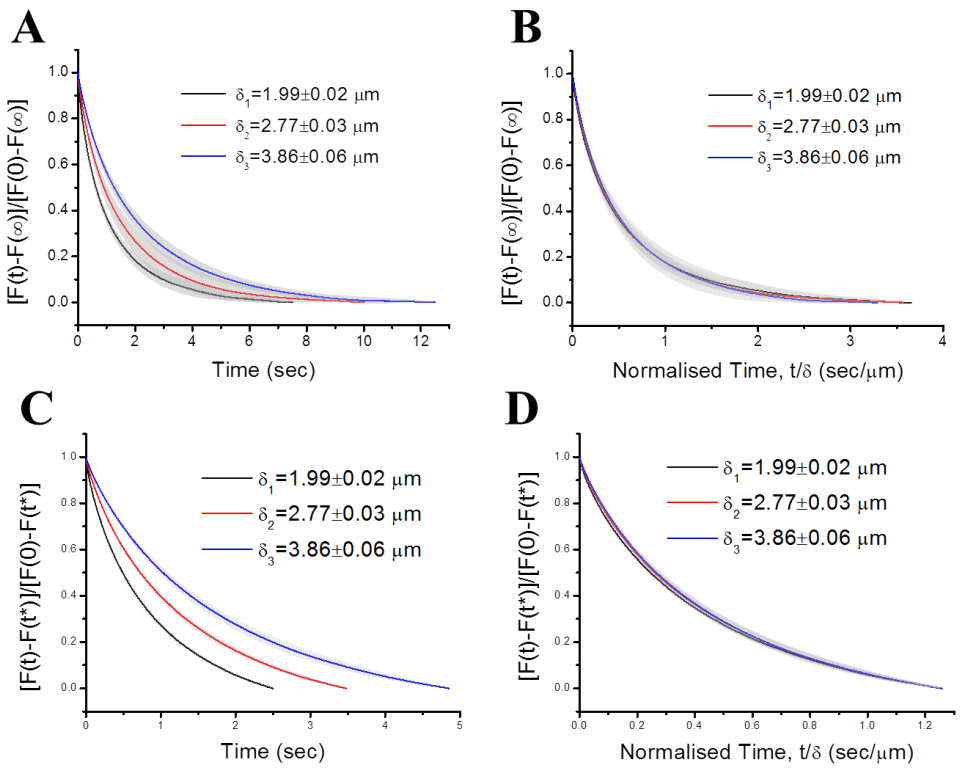

Figure 4-3 Normalisation of force-relaxation curves acquired on hydrogel.

(A) Normalisation of force-relaxation curves (Figure 4-2) using equation (3.7) plotted as a function of time. For force renormalisation, a separate time t^* was chosen for each curve such that $t^* = t_\infty$, with t_∞ the time at which each curve reaches its plateau: t_1^* = 7.5 s, t_2^* = 10 s and t_3^* = 12.5 s. (B) Normalised force-relaxation curves from A plotted as a function of time divided by indentation depth δ (t/δ). Time rescaling was performed for each force relaxation curve separately using their respective indentation depth. Following force renormalisation and time-rescaling, all force-relaxation curves collapsed onto one single curve. (C) Normalisation of force-relaxation curves shown in Figure 4-2 using equation (3.7) plotted as a function of time. For force renormalisation, a separate time t^* dependent on indentation depth was chosen for each curve with $t^* = \alpha\delta$. Choosing α = 1.25 s.μm^{-1} gave times t_1^* = 2.5 s, t_2^* = 3.5 s and t_3^* = 4.9 s. (D) Normalised force-relaxation curves from C plotted as a function of time divided by indentation depth δ (t/δ). Time rescaling was performed for each force-relaxation curve separately using their respective indentation depth. Following force renormalisation and time-rescaling, all force-relaxation curves collapsed onto one single curve. In all graphs, solid lines and grey shadings represent the mean and standard deviations at each data point, respectively.

As explained earlier in Chapter 3.8, collapse of curves can also be obtained following normalisation of time for times shorter than t_∞ . For times $t^* < t_\infty$ to obtain collapse of force relaxation of poroelastic material onto a master curve, t^* must be selected proportional to the indentation depth δ specific to each curve: $t^* = \alpha\delta$ where α (with unit of s.μm^{-1}) is an arbitrary number fixed for all curves (Figure 4-3C). With this choice of t^* a similar collapse of curves was observed using force and time normalisation (Figure 4-3D), confirming the dominance of poroelasticity in the force relaxation of gels in these experiments. Fitting the relaxation curves with equation (3.5) gave a poroelastic diffusion constant of 33±4 μm.s^{-1} for the hydrogel comparable to the previously reported values [137].

4.1.3 Cellular force-relaxation at short timescales is poroelastic

Population averaged force-relaxation curves showed similar trends for both HeLa and MDCK cells with a rapid decay in the first 0.5 s followed by slower decay afterwards (Figure 4-4A). When plotted in log-log scale in Figure 4-4B, we see that force-relaxation clearly displayed two separate regimes: a plateau lasting ~ 0.1-0.2 s followed by a transition to a linear regime. This indicated that at short time-scales cellular force-relaxation did not follow a simple power law. Comparison with force-relaxation curves acquired on physical hydrogels, which display a plateau at short time-scales followed by a transition to a second plateau at longer time-scales (Figure 4-2A, B), suggests that the initial plateau observed in cellular force-relaxation may correspond to poroelastic behaviour. Indeed poroelastic models fitted the force-relaxation data well for short times (< 0.5 s); whereas power law models were applicable for times longer than ~ 0.1-0.2 s (Figure 4-4B).

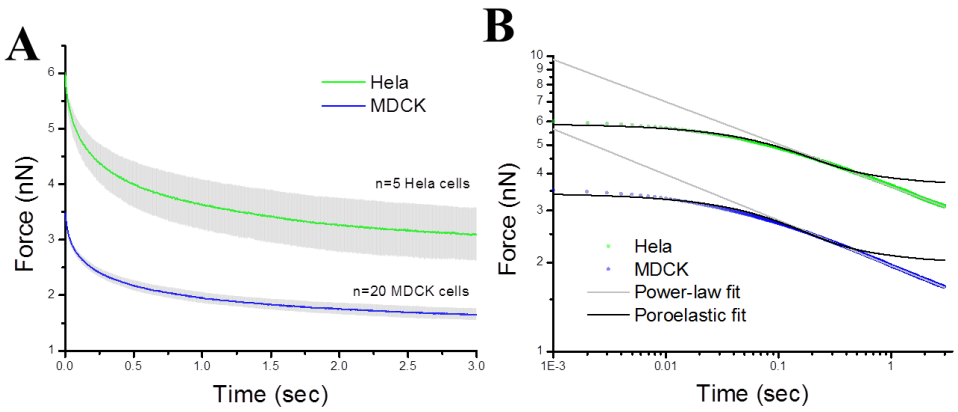

Figure 4-4 Force-relaxation curves acquired with different indentation depths on cells.

(A) Population averaged force-relaxation curves for HeLa cells (green) and MDCK cells (blue) for target indentation depths of 1.45 μm for HeLa cells and 1.75 μm for MDCK cells. Curves are averages of n = 5 HeLa cells and n = 20 MDCK cells. The grey shaded area around the average relaxation curves represents the standard deviation of the data. (B) Population averaged force-relaxation curves for HeLa cells (green) and MDCK cells (blue) from D-I plotted in a log-log scale. For both cell types, experimental force-relaxation was fitted with poroelastic (black solid line) and power law relaxations (grey solid line).

To gain further insight into the nature of cellular force-relaxation at short time-scales, I acquired experimental relaxation curves following indentations with increasing depths. For analysis of these experiments, I selected cells with identical elasticities such that application of a chosen target force resulted in identical indentation depths and I averaged their relaxation curves. This filtering procedure ensured that the cellular relaxation curves were comparable in all aspects (Figure 4-5A and Figure 4-6A) and allowed us to assess whether or not cellular relaxation was dependent upon indentation depth. As shown earlier for hydrogels, the most important property of these gels as a poroelastic material is that their characteristic relaxation time depends on indentation depth. Indeed, the length scale dependency of relaxation in poroelastic materials is in contrast to power law and linear viscoelastic exponential relaxation behaviours.

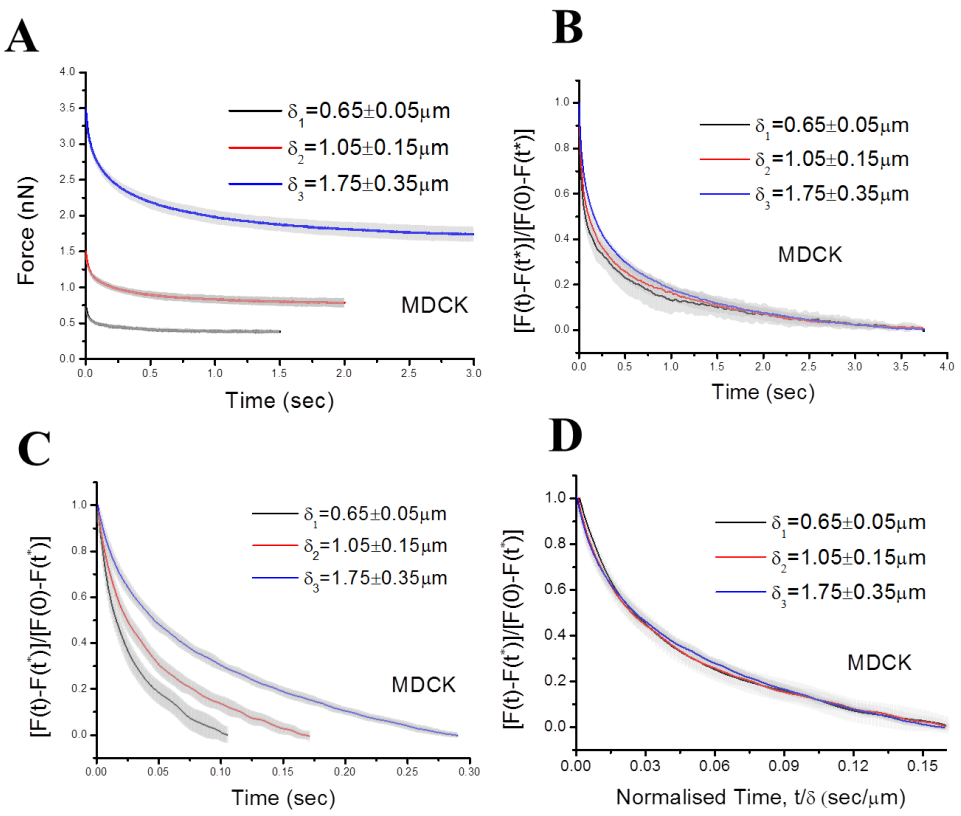

Figure 4-5 Normalisation of force-relaxation curves acquired on MDCK cells.

(A) Force-relaxation curves acquired on MDCK cells for three different indentation depths (δ_1, δ_2 and δ_3). Each relaxation curve is the average of 20 force-relaxation curves acquired on cells with matching elasticities of E = 0.4±0.1 kPa. Elasticity matching ensured that identical forces were applied onto each cell to obtain a given indentation depth. (B) Normalisation of force-relaxation curves shown in A using equation (3.7) choosing t^* = 3.6 s for all curves. Relaxation curves were significantly different from one another for times shorter than ~ 0.5 s but appeared to collapse at times longer than ~ 1.2 s. (C) Normalisation of force-relaxation curves shown in A using equation (3.7) plotted as a function of time. For force renormalisation, a separate time t^* dependent on indentation depth was chosen for each curve with $t^* = \alpha\delta$. Choosing α = 0.16 s.μm^{-1} gave times t_1^* ~ 105 ms, t_2^* ~ 170 ms and t_3^* ~ 285 ms. (D) Normalised force-relaxation curves from C plotted as a function of time divided by indentation depth δ (t/δ). Time rescaling was performed for each force relaxation curve separately using their respective indentation depth δ. Following force renormalisation and time-rescaling, all three force-relaxation curves collapsed onto one single curve. In all graphs, solid lines and grey shadings represent the mean and standard deviations at each data point, respectively.

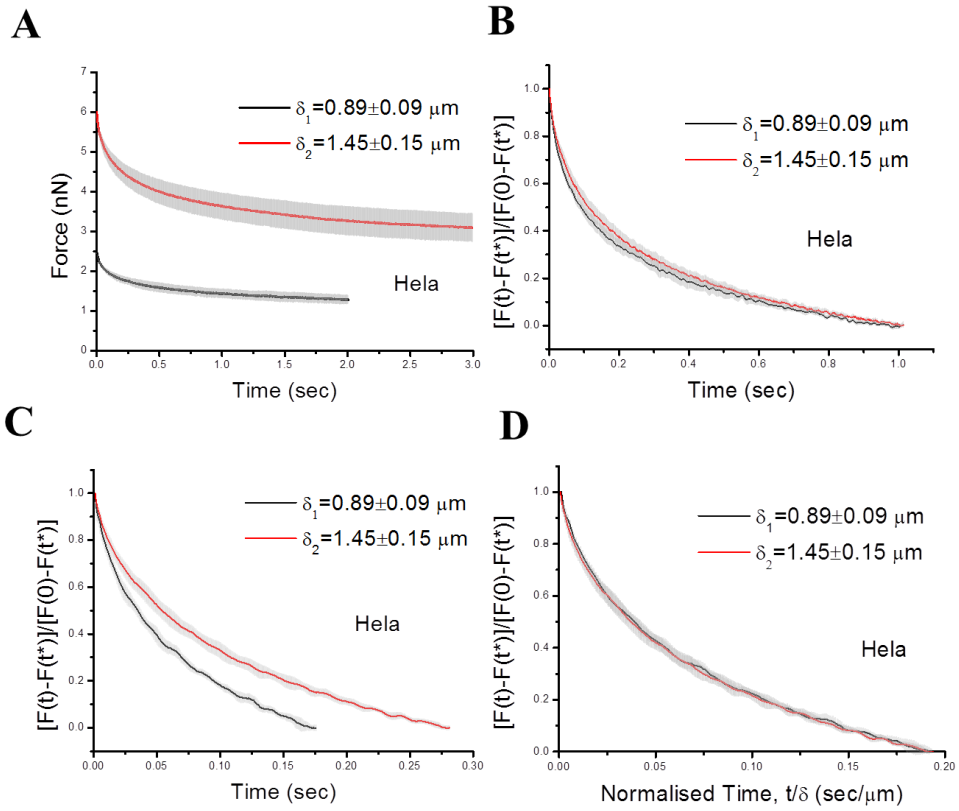

Figure 4-6 Normalisation of force-relaxation curves acquired on HeLa cells.

(A) Force-relaxation curves acquired on HeLa cells for two different indentation depths (δ_1 and δ_2). Each relaxation curve is the average of 5 force-relaxation curves acquired on cells with matching elasticities of E = 0.66±0.1 kPa and heights of h = 5.5±0.3 μm. This ensured that identical forces were applied onto each cell to obtain a given indentation depth. Matching of cell heights was necessary to minimise substrate effects due to the smaller thickness of HeLa cells compared to MDCK cells. (B) Normalisation of force-relaxation curves shown in A using equation (3.7) choosing t^* = 1 s for all curves. Relaxation curves were significantly different from one another for times shorter than ~ 0.5 s but appeared to collapse at times longer than ~ 0.6 s. (C) Normalisation of force-relaxation curves shown in A using equation (3.7) plotted as a function of time. For force renormalisation, a separate time t^* dependent on indentation depth was chosen for each curve with $t^* = \alpha\delta$. Choosing α = 0.19 s.μm^{-1} gave times t_1^* ~ 170 ms and t_2^* ~ 275 ms. (D) Normalised force-relaxation curves from C plotted as a function of time divided by indentation depth δ (t/δ). Time rescaling was performed for each force relaxation curve separately using their respective indentation depth. Following force renormalisation and time-rescaling, both force-relaxation curves collapsed onto one single curve. In all graphs, solid lines and grey shadings represent the mean and standard deviations at each data point, respectively.

After force normalisation, experimental force-relaxation curves acquired on cells for different indentation depths collapsed for times longer than ~ 1 s, but were significantly different from one another for shorter times (Figure 4-5B for MDCK cells and Figure 4-6B for HeLa cells), suggesting that, at short times, relaxation is length-scale dependent consistent with a poroelastic behaviour.

For cells, experimental force-relaxation curves do not reach a plateau because relaxation follows a power law at long time-scales (Figure 4-4B). Hence, to determine if relaxation displayed a poroelastic behaviour at short time-scales, I followed the force normalisation and time rescaling steps described in Chapter 3.8 for cases where $t^* < t_\infty$. These procedures resulted in all cellular force-relaxation curves collapsing onto a single master curve (Figure 4-5D for MDCK cells and Figure 4-6D for HeLa cells). This behaviour was apparent in poroelastic hydrogels for both long and short time-scales (Figure 4-3B, D) and in cells for times shorter than ~ 0.5 s (Figure 4-5D and Figure 4-6D). Taken together, these data suggested that at short time-scales cellular relaxation is indentation depth dependent and therefore that cells behaved as poroelastic materials.

4.2 Kinetics of whole cell swelling/shrinking

Using fluorescent particles attached to the cell membrane (see Figure 4-7A) and particle tracking techniques, my aim here was to monitor the response of cells to osmotic perturbations to investigate the swelling/shrinking kinetics of the cytoplasm. In particular off-plane defocused images of fluorescent particles (depicted in Figure 3-6A, C) enabled us to measure time-dependent cellular deformations in the z-direction very precisely. HeLa cells with fluorescent beads bound to their membrane were suddenly exposed to a change of osmolarity induced by addition of a small volume of water/sucrose (achieving final concentrations of 50% water and 400 mM sucrose). A sudden change in osmolarity induces osmotic pressure gradients that drive water in or out of the cell resulting in it swelling or shrinking. After application of hypo/hyperosmotic shock, changes in the cell

height were measured over time by monitoring changes in the radius of the outer ring (formed by the out of focus image of the fluorescent bead attached to the cell surface, Figure 3-6A, B, C) to determine changes in z position of the bead.

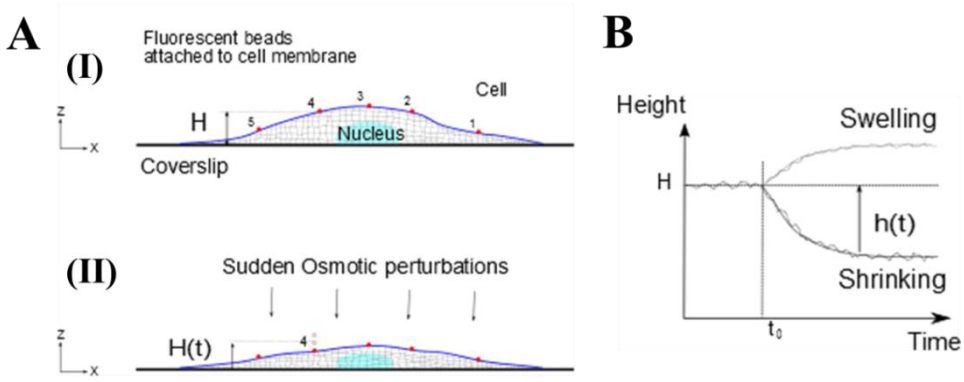

Figure 4-7 Experimental setup to investigate the poroelastic behaviour of cells during swelling/shrinkage. (A-I) Schematic of fluorescent microbeads attached to the cell membrane. (A-II) By changing the osmolarity of the extracellular medium we can induce osmotic pressure gradients across the cell membrane that drive water in or out of the cell resulting in swelling or shrinkage (Here a decrease in cell volume due to hyperosmotic shock is depicted). Keeping the focal plane fixed, changes in the vertical position of each bead due to swelling/shrinkage of the cell can be determined from the outer ring radius of the defocused image using the calibration curve, Figure 3-6C. (B) Changes in height of beads over time after application of hypo-osmotic/hyperosmotic shock at time t_0. Fitting the displacement curve to the analytical solutions for poroelastic hydrogels allows the poroelastic properties of the cell to be estimated.

First, I asked whether the cell behaves as a poroelastic gel by fitting the experimental displacement curves to the analytical solutions for swelling kinetics of poroelastic gels. Then the poroelastic diffusion coefficient D_p was computed and compared with the values obtained from AFM indentation experiments in Chapter 5. As proposed in Chapter 6, this method could be employed to dissect the contribution of different cellular layers to cell rheology and to determine the spatial distribution of D_p.

4.2.1 Swelling/shrinkage of a constrained poroelastic material

Consider a thin layer of poroelastic material (a gel) attached on one side to a fixed substrate and immersed in a solvent for sufficiently long to reach an equilibrium homogeneous state with C_0 and μ_0 the initial concentration and chemical potential of the solvent respectively. When the gel is suddenly exposed to a solvent with different chemical potential $\bar{\mu}$, the chemical potential gradient $\bar{\mu} - \mu_0$ drives the solvent to flow into/out of the gel. The displacement and chemical potential fields can be considered one dimensional in z if the lateral dimensions L_x and L_y of the gel are much larger than its thickness H ($L_x, L_y >> H$). Indeed, in this case, there is a negligible amount of flow from the edges and the solvent flows mostly through top surface of the gel. The gel is constrained in xy so $\varepsilon_{xx} = \varepsilon_{yy} = 0$ and the problem is similar to uniaxial strain consolidation as described in Chapter 2 (2-4-2). For cells, constraint in xy is achieved through focal contacts and integrin transmembrane proteins. The gel can freely swell and shrink from the top surface ($\sigma_{zz} = 0$) and thus the equations (2.48) and (2.50) can be written in terms of chemical potential:

$$\begin{cases} \varepsilon_{zz} = \dfrac{\partial u_z}{\partial z} = \dfrac{(1-2\nu_s)}{2G_s(1-\nu_s)} \dfrac{\mu - \mu_0}{\Omega} & (a) \\ \sigma_{xx} = \sigma_{yy} = -\dfrac{(1-2\nu_s)}{(1-\nu_s)} \dfrac{\mu - \mu_0}{\Omega} & (b), \end{cases} \tag{4.1}$$

$$\frac{\partial \mu}{\partial t} = D_p \frac{\partial^2 \mu}{\partial x^2}. \tag{4.2}$$

Considering the top surface as the reference point, the spatial and temporal evolution of chemical potential can be derived using appropriate boundary and initial conditions. The equilibrium chemical potential before application of osmotic shock yields the initial condition $\mu(z,0) = \mu_0$. A step change in chemical potential on the top surface which remains constant over time $\mu(0,t) = \bar{\mu}$ and the no flow condition at the bottom of the

gel $\frac{\partial \mu}{\partial z}|_{z=-H}=0$ yield the boundary conditions. Therefore the solution of the diffusion equation (4.2) is very similar to equation (2.52):

$$\frac{\mu(z,t)-\bar{\mu}}{\mu_0-\bar{\mu}}=-\sum_{n=1,3,..}^{\infty}\frac{4}{m\pi}\sin\ \frac{n\pi z}{2H}\ \ \exp\ -n^2\pi^2\tau\ \ , \tag{4.3}$$

where $\tau = D_p t / 4H^2$ is the dimensionless time. One can also obtain the solution for infinite thickness (also applicable for early times after shock) as:

$$\frac{\mu(z,t)-\bar{\mu}}{\mu_0-\bar{\mu}}=erfc\left(-\frac{z}{\sqrt{4D_p t}}\right). \tag{4.4}$$

After a long enough time $t >> H^2 / D$, the solvent inside the gel has reached a new equilibrium $\mu=\bar{\mu}$ and the gel has shrunken/swollen from its initial height H, by h_∞ to its final height. Considering the total final strain at very long times $\varepsilon_{zz} = \frac{h_\infty}{H}$ and employing equation (4.1)-a, the final change in thickness of the gel is:

$$h_\infty=\frac{(1-2\nu_s)}{2G_s(1-\nu_s)}\frac{\mu-\mu_0}{\Omega}H. \tag{4.5}$$

The change of thickness at top surface $h(t)$ is derived by integrating equation (4.1) and using equations (4.3) and (4.5):

$$\frac{h(t)}{h_\infty}=1-\sum_{n=1,3,..}^{\infty}\frac{8}{m^2\pi^2}\exp\ -n^2\pi^2\tau \tag{4.6}$$

Using equation (4.4) the change in the thickness of the gel is written as:

$$\frac{h(t)}{h_\infty}=\frac{2}{H}\sqrt{\frac{D_p t}{\pi}}. \tag{4.7}$$

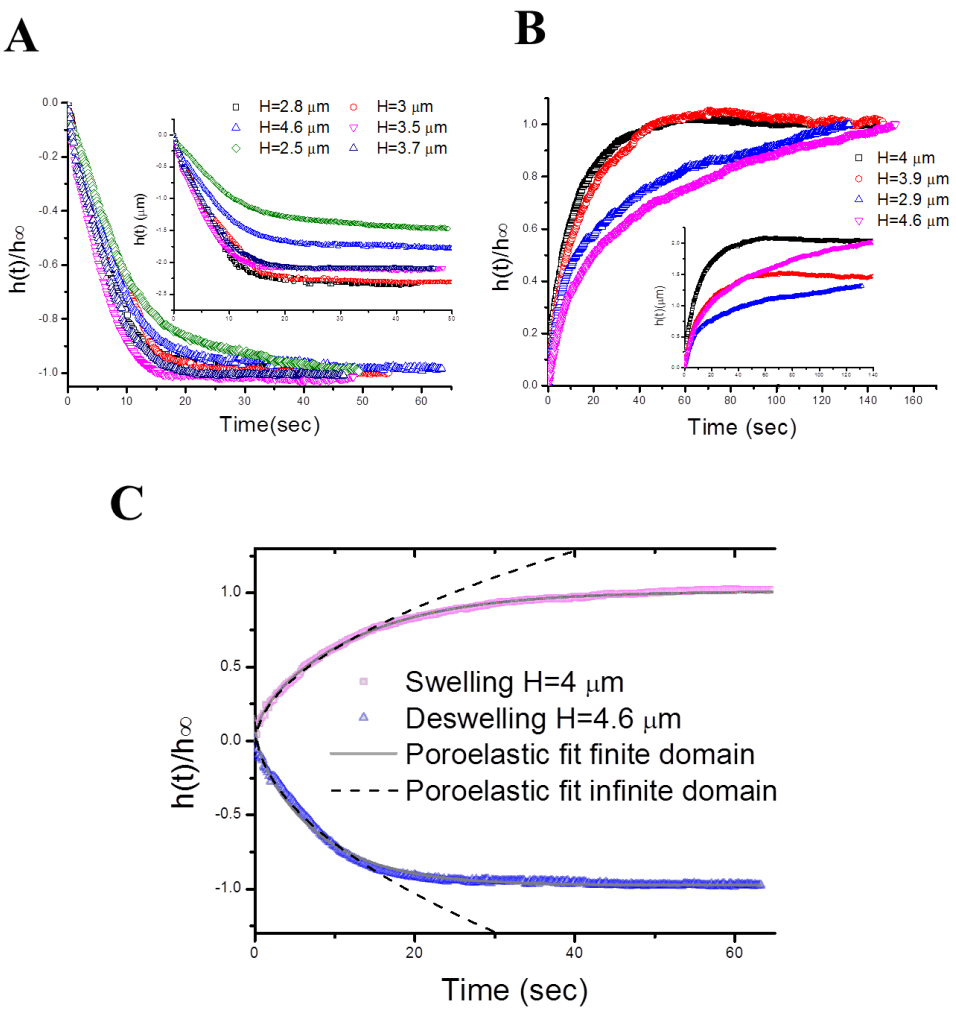

Figure 4-8 Kinetics of cell swelling/shrinking in HeLa cells

(A, B) Swelling/shrinking kinetics of HeLa cells in response to hyperosmotic (A) and hypoosmotic (B) shocks. Dynamics of cellular swelling/shrinking is precisely probed by tracking the height $h(t)$ of fluorescent beads attached on the cell membrane at different heights H. The curves show the change cell height normalised to the final change in thickness $h(t)/h_{\infty}$. The inset shows the absolute change of height $h(t)$. (C) Swelling/shrinking curves were fitted to the poroelastic model using equation (4.6) derived for poroelastic swelling of constrained gels. Fits to the equation (4.7) describes the early stage behaviour of cellular swelling/shrinking.

4.2.2 Poroelasticity can explain the kinetics of cellular swelling/shrinking

During the experiments, HeLa cells were exposed to hyper/hypoosmotic medium at t =0 and the vertical displacement of the attached beads was measured as a function of time to obtain swelling/shrinking curves (Figure 4-8A, B insets). These curves were then normalized with respect to the final change in the height h_∞ (Figure 4-8A,B). The $h(t)/h_\infty$ curves were fitted with the analytical solution derived for a poroelastic cytoplasm in equation (4.6) (Figure 4-8C). This solution fitted the experimental curves well and fitting gave the poroelastic diffusion constants of D_p = 0.3±0.2 μm^2.s^{-1} (n = 16) and D_p = 0.6±0.3 μm^2.s^{-1} (n = 10) for swelling and shrinking respectively. Furthermore, considering the early stage behaviour, the first 10 s of curves were fitted with analytical solution in equation (4.7) and diffusion coefficients of D_p = 0.4±0.2 μm^2.s^{-1} and D_p = 0.7±0.3 μm^2.s^{-1} were obtained for swelling and shrinking respectively (Figure 4-8C). The values obtained from fits with the short timescale solution were in good agreement with those obtained fitting with the full analytical solution.

4.3 Discussion and conclusions

To validate the experimental strategy and analytical methods, first the force-relaxation behaviour of hydrogels, which are well-characterised poroelastic materials, was examined. Intrinsic viscoelasticity and poroelasticity concurrently contribute to the time dependent deformation of gels. The intrinsic viscoelasticity is associated with conformational changes in the solid meshwork, while poroelasticity is related to the redistribution of fluid. During indentation tests on gels (similar to the hydrogel that is used in my experiments) the viscoelastic relaxation time results from the occurrence of multiple microscopic processes such as slippage and reptation of polymer chains [87]. This relaxation time is determined by the ratio of the shear viscosity η and the shear modulus G: $\tau_v \sim \eta/G$ [87], and is indentation depth independent as both η and G are

independent of contact size. In contrast, the poroelastic relaxation time $\tau_p \sim R\delta / D_p$ is related to the time scale of fluid redistribution/migration within/out of the deformed region and this depends on the contact radius and indentation depth. For hydrogels, plots of force-relaxation curves in log-log coordinates suggest the involvement of a limited number of relaxation processes consistent with poroelastic behaviour. More importantly, for experiments performed with different indentation depths, appropriate normalisation of experimental force-relaxation curves resulted in the collapse of all curves onto a single master curve. This provides strong evidence for the dominance of poroelasticity in relaxation of hydrogels in agreement with [121, 137, 142]. It may thus be concluded that poroelasticity is the dominant mechanism of relaxation in our indentation experiments on hydrogels.

A detailed examination of the functional form of cellular force-relaxation curves at different time scales was undertaken and these curves were compared to force-relaxation curves acquired on hydrogels. Force-relaxation induced by fast localised indentation by AFM contained two regimes: at short time-scales, the time-scale of force-relaxation was indentation depth dependent, a hallmark of poroelastic materials; while at longer timescales relaxation exhibited a power law behaviour. This confirms that living cells are much more complex active materials than simple hydrogels. Indeed, at physiological time-scales (0.1-10s), in addition to conformational changes in polymeric network of cytoskeleton and rearrangements in the solid phase (macromolecules) other factors such as turnover of cytoskeletal fibres, activity of myosin molecular motors and network rearrangements due to association and dissociation of crosslinkers, also influence the relaxation significantly.

Cell mechanical studies over the years have revealed a rich phenomenological landscape of rheological behaviours that are dependent upon probe geometry, loading protocol and loading frequency [56, 58, 63-65], though the biological origin of many of these regimes

remains to be fully explored. It is widely recognized that over wide ranges of frequency, the rheology of living cells exhibits a weak power law behaviour in which the viscoelastic response does not exhibit any characteristic timescale (see Chapter 2.2.3). The structural damping model, which has previously been applied to characterise a variety of biological materials [143], was recently implemented to describe the observed power law behaviour in cells [33]. In the power law structural damping model, the storage and loss moduli are both weak power law functions of frequency: $G', G'' \sim \omega^{\beta}$, $0 \leq \beta \leq 1$, and are related through a structural damping coefficient $\eta_{damp} = G''/G' = \tan(\beta\pi/2)$. As a result, in this model, dissipation is linked to an elastic stress rather than an independent viscous stress. A Newtonian viscous term μ was added to the loss modulus of the model to capture the observed dynamics at short timescales [112]. In magnetic twisting cytometry, the addition of such a linear term could be to take into account the effects of drag forces generated from viscous interaction between the probe and the surrounding fluid. However, the calculated values for this viscous term ($\mu > 1$ pa.s, [33, 79, 144]) are much larger than the viscosity of surrounding fluid (~ 0.001 pa.s). Therefore, the physical origins of this additional viscous parameter are still not clear and are therefore debatable.

The shape of my force-relaxation curves at short timescales was not consistent with a power law behaviour (similar to experiments reported by others [53, 145-149]) and it is surprising that the initial non-power law regime observed in my experiments should not have been described before. I envisage two major reasons for this. First, most recent experiments aim to describe the shear rheology of cells over many decades of frequency and therefore apply oscillatory deformations to the cell, using shear rheology methods rather than focusing on volumetric changes (dilatational rheology) as done here. Indeed, measurements of shear rheology are of little or no consequence in understanding cell rheology for which volumetric deformations are critical (e.g. cell migration [150] and the formation of quasi-spherical protrusions known as blebs [107]). My experiments were designed to apply large volumetric deformations via micro-indentation tests such that

they inherently capture the dilatational rheology of the cell. Indeed, my experiments are placed in a regime where intracellular water flows should play an important role: rapid application of a large volumetric deformation and observation of force relaxation over short and intermediate time-scales using microindentation. Second, in experiments reported by other groups, such as force-relaxation experiments similar to the ones presented here [52, 53, 145, 151] and also using other very different experimental setups [146, 147, 149], a rapid initial force relaxation was observed but its origin was not examined. In these experiments, either the short timescale behaviours were neglected, only the asymptotic part of relaxation was fitted, or functions such as double exponentials with both fast and slow relaxation times or stretched exponential functions were used to fit the experimental data.

To observe water flows in response to applied deformations, one needs to deform the cell with a large probe over a short rise time t_r. Indeed, the time scale of application of deformation t_r must be shorter than the time it takes for water to drain out of the deformed volume $t_p \sim L^2 / D_p \sim L^2\mu/(E\xi^2)$ (L is the probe length-scale and in the case of indentation: $L \sim \sqrt{R\delta}$ with R the radius of the indenter and δ indentation depth). In the context of oscillatory sinusoidal loading, shorter rise time deformations are achieved by increasing the frequency of excitation. However, if the loading frequency is too high, water does not have time to drain out of the deformed volume before the next cycle of deformation is applied. In this regime, water will not move relative to the mesh and therefore inertial and structural viscous effects from the mesh are sufficient to describe the system [81, 152]. Previous work has shown that for frequencies $f_p >> E\xi^2/(L^2\mu)$ such coupling occurs [81]. Hence, to observe poroelastic effects in oscillatory experiments, it is required to deform the material at frequencies larger than $1/t_p$ to satisfy the short rise time condition to induce fluid flow but smaller than f_p so that fluid and mesh are not coupled. As both conditions have identical scaling, it is expected that they only be satisfied in a narrow window around f_p ~ 5 Hz for my experimental

conditions. Most oscillatory loading experiments sample rheology in 2 points per decade and hence would likely not detect this window. Hence, to observe poroelastic effects, we need to apply deformations with rise times shorter than t_p and repeated at frequencies lower than f_p.

It should be emphasised that this type of loading regime is very physiologically relevant. Indeed, cells in tissues of the cardiovascular or respiratory systems are exposed to large strain deformations (tens of %) applied at high strain rates (> 20%.s^{-1}) but with low repeat frequencies (< 4 Hz) (e.g. 10% strain applied at ~ 50%.s^{-1} repeated at up to 4 Hz for arterial walls [153], 70% strain applied at up to 900%.s^{-1} repeated at up to 4 Hz in the myocardial wall [154], and 20% strain applied at > 20%.s^{-1} repeated at ~ 1 Hz for lung alveola [155]). As the changes in cell shape that occur in physiological tissue deformation are similar in magnitude or larger than those induced in our experiments and are repeated with low frequency, I expect intracellular water redistribution to play an important role in the relaxation of cells within these tissues

When force-relaxation curves acquired for different indentation depths on cells were renormalized for force and rescaled with a time-scale dependent on indentation depth, all experimental curves collapsed onto a single master curve for short time-scales, confirming that the initial dynamics of cellular relaxation is dominated by poroelastic effects and intracellular water flow (Figure 4-5 and Figure 4-6), but for larger timescales the relaxation curves exhibit a weak power law behaviour. Together these data suggest that in my experiments the power-law dynamics and poroelasticity coexist. For timescales shorter than ~ 0.5 s, intracellular water redistribution contributed strongly to force-relaxation, consistent with the ~ 0.1 s time-scale measured for intracellular water flows in the cytoplasm of HeLa cells [156]. At long timescales when fluid is fully redistributed, fluid related poroelastic dissipations became negligible and structural damping effects (manifested in the form of a weak power law(come into play as the main source of dissipation.

Volume exclusion effects are the primary source of swelling/shrinking behaviour in artificial and biological gels as well as living cells. The dynamics of swelling and shrinking mainly depends on the rate at which water can be transported into and out of the gel. However, poroelasticity can also significantly affect the swelling/shrinking kinetics: for an elastic porous medium, the deformation of the porous matrix induced by osmotic shock significantly limits the rate of swelling/shrinkage. Indeed a very stiff sponge cannot swell/shrink even if water can diffuse into/out of it infinitely fast. Here the hypothesis that the swelling/shrinking behaviour of cytoplasm is similar to that of hydrogels was tested by examining its volume response to osmotic perturbations. It is shown that that the swelling/shrinking kinetics of cytoplasm can be well described via a simple 1-D poroelastic model and analytical solutions fitted the experimental data well. The estimated values of the diffusion coefficient were within the previously reported range of 0.1 to 10 $\mu m.s^{-1}$ [100-102] but around one order of magnitude smaller than those obtained from indentation experiments (as presented in next chapter). There are several possible sources of this discrepancy as shall be explained in the following paragraph.

A one dimensional model for swelling/shrinking of a constrained gel was used to determine the cellular poroelastic diffusion coefficient from fits of experimental curves. This one dimensional formulation was a good approximation for my analysis because the lateral movements of the membrane-attached beads were much smaller than their vertical displacement (less than ~ 0.5 μm in xy versus greater than ~ 2 μm in z). However this model is only valid if the osmotic perturbations are applied in a step manner (infinitely fast). In our experiments, it takes a certain amount of time for the added osmolyte to mix with the bath solution and for osmolyte to equilibrate. This non instantaneous change in osmolarity could be one reason for underestimation of diffusion coefficient using proposed the poroelastic model. Comparing shrinking and swelling experiments, faster poroelastic diffusion constants were obtained in shrinking experiments, which might be due to irreversible dynamics of the membrane water channels (aquaporins) or different

responses of the solid phase and cytoskeleton to tensional versus compressional forces created during hyperosmotic shrinkage and hypoosmotic swelling, respectively.

The structural heterogeneity and complex nature of the cell may be the key reason that different experimental setups report different values for cellular mechanical and rheological properties. AFM probes only small regions of cytoplasm whereas all of the structures inside the whole cell are perturbed during a swelling/shrinking experiment. Indeed several cellular layers, such as the cell membrane, the cell cortex, the nucleus, and the granular filamentous interior, each with different permeabilities and elasticities, contribute to setting the poroelastic behaviour of the cell in swelling/shrinking. During indentation experiments, small regions of cytoplasm underneath the indentor are compressed and water movement is directed towards the cell interior (see Figure 4-9). For these indentation experiments, the cell membrane most likely does not play a significant role in setting the rate of water permeation and the membrane can be assumed to be fully permeable. In contrast, during swelling/shrinkage of the whole cell, water infiltration through cytoplasm and all parts of the cell (including the nucleus) sets the dynamics of swelling/shrinking. Specifically the rate of swelling/shrinking can be limited significantly by the rate at which water can pass through thin layers of cytoplasm such as the cell cortex and the plasma membrane.

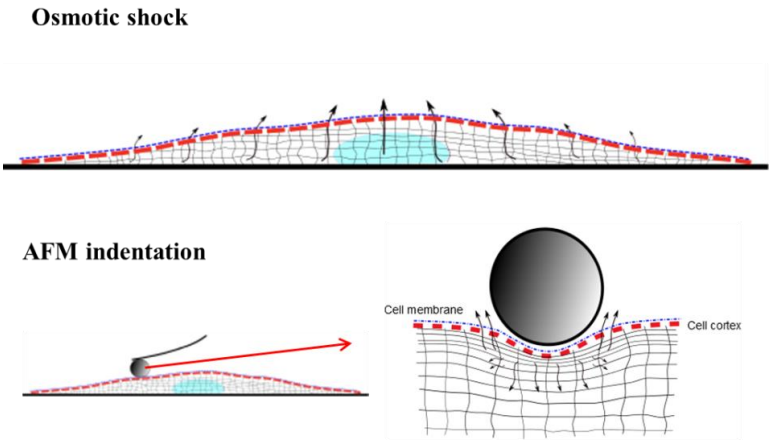

Figure 4-9 Schematic representation of intracellular water movements in different experimental setups. During osmotic shocks the water permeates through whole cytoplasm and all parts of the cell whereas for AFM indentation tests water movements is restricted to small regions of cytoplasm underneath the indentor. The arrows show possible directions of water movement.

The plasma membrane has long been thought of as the main regulator for volumetric responses of cells to osmotic perturbations. However, it has been recently shown that in the absence of a cell membrane the cytoplasm of mammalian cells has intrinsic osmosensitivity [157]. Simple diffusion through the lipid bilayer and water selective facilitated diffusion through the water channels (aquaporins) are the main pathways for water permeation during osmotic perturbations [156, 158]. Coherent anti-Stokes Raman scattering (CARS) microscopy allows observation of intracellular hydrodynamics by monitoring H_2O/D_2O exchange in living cells [159]. Using CARS, recent experimental measurements found that for Hela S3 cells it takes less than ~ 100 ms for water to fully permeate across the plasma membrane and fully exchange, much shorter than our measured relaxation times (>> 1 s) for the volumetric response of HeLa cells to osmotic perturbations. Therefore, in addition to diffusional effects, mechanical factors also play an important role in setting the relaxation time. Furthermore, considering a cell height of ~ 4 μm and a poroelastic diffusion coefficient ~ 40 $\mu m^2.s^{-1}$ yields the ratio of D_p / h ~ 10 $\mu m.s^{-1}$ which is of the magnitude as the measured membrane diffusional permeability ~ 10-40 $\mu m.s^{-1}$ [156, 159] suggesting that the solid phase of cytoplasm has a similar

contribution in limiting the rate of water permeation to the membrane. I conclude that the simple concept of a water-filled container surrounded by membrane, cannot fully explain the volumetric response of cell to osmotic perturbations and that the solid phase of cytoplasm contributes significantly in this response. I suggest that poroelastic model for the cytoplasm is a more physical concept that inherently considers the gel-like nature of cytoplasm and can help explain the dynamics of volume changes. However, further experiments suggested in Chapter 6 are required to precisely dissect the role of the membrane and different parts of the solid phase in determining the cell's response to osmotic shocks.

Chapter 5

Poroelastic properties of cytoplasm: Osmotic perturbations and the role of cytoskeleton

Equation Chapter (Next) Section 1

It has been shown in the previous chapter that the framework of poroelasticity is well suited to understanding the time-dependent mechanical properties of cells. In this framework, the cytoplasm comprises two phases: a porous solid phase (cytoskeleton, organelles, macromolecules) and a fluid phase (cytosol). The conceptual advantage of such a description is that cellular rheology can be related to measurable cellular parameters (elastic modulus E, hydraulic pore size ξ, and cytosolic viscosity μ) using a simple scaling law $D_p \sim E\xi^2/\mu$ and therefore changes in rheology resulting from changes in cellular organisation can be qualitatively predicted. In this chapter, AFM indentation tests were utilized to measure cellular stress-relaxation in response to rapid

local force application in conjunction with chemical, genetic, and osmotic treatments to modulate two of the parameters that scaling law predicts should influence cellular time-dependent mechanical properties: pore size ξ and the elasticity E.

5.1 Determination of cellular elastic, viscoelastic and poroelastic parameters from AFM measurements

To provide baseline behaviour for perturbation experiments, I measured the elastic, viscoelastic and poroelastic properties of MDCK, HeLa, and HT1080 cells by fitting force-indentation (Figure 3-3) and force-relaxation (Figure 5-1) curves with Hertzian and viscoelastic or poroelastic models, respectively. Measurement of average cell thickness suggested that for time-scales shorter than 0.5 s, cells could be considered semi-infinite and forces relaxed according to an exponential relationship with $F(t) = \exp(-D_p t / l^2)$ (see Chapter 2.4, 5, Figure 2-5 and Figure 2-7C). In our experimental conditions (3.5-6 nN force resulting in indentation depths less than 25% of cell height, Figure 4-1B, C), force-relaxation with an average amplitude of 40% was observed with 80% of total relaxation occurring in ~ 0.5 s (Figure 4-4 and Figure 5-1A).

Analysis of the indentation curves yielded an elastic modulus of E = 0.9±0.4 kPa for HeLa cells (N = 189 curves on n = 25 cells), E = 0.4±0.2 kPa for HT1080 cells (N = 161 curves on n=27 cells), and E = 0.4±0.1 kPa for MDCK cells (n = 20 cells). Poroelastic models fitted experimental force-relaxation curves well (on average r^2 = 0.95, black line, Figure 5-1A) and yielded a poroelastic diffusion constant of D_p = 41±11 μm^2.s^{-1} for HeLa cells, D_p = 40±10 μm^2.s^{-1} for HT1080 cells, and D_p = 61±10 μm^2.s^{-1} for MDCK cells.

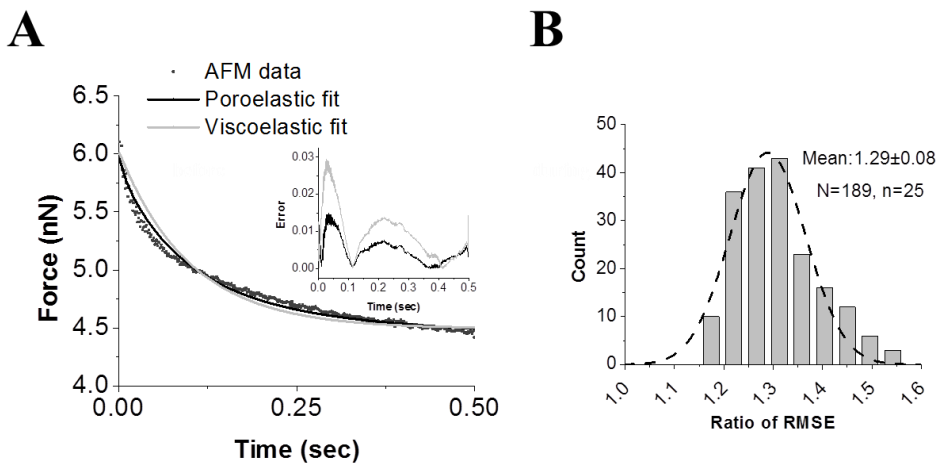

Figure 5-1 Fitting force-relaxation curves.

(A) The first 0.5 s of force-relaxation curves were fitted with the poroelastic model (black line) and the standard linear viscoelastic model (grey line). Poroelastic models fitted the data better than the single phase viscoelastic model especially at short times. Inset: the percentage error of each fit defined as $|F_{AFM} - F_{fit}|/F_{AFM}$. (B) Ratio of root mean square error (RMSE) of the viscoelastic fit to the RMSE of poroelastic fit.

Assuming that the cytoplasm behaves as a standard linear viscoelastic material and to measure the apparent viscosity of the cytoplasm, I fitted force-relaxation curves with equation (3.6) ($F(t) \sim \exp(-k_1 t/\eta)$). Using the approach phase of AFM indentation curves, I measured cellular elasticity and assumed $k_1 \sim E$. Therefore the relaxations predicted by a viscoelastic formulation depend on only one free parameter: the apparent viscosity η. Since the force-relaxation curves are indentation depth dependent, to calculate the apparent viscosity I considered only the curves with indentation depths of ±10% of the mean values obtained from distribution of indentation depths (Figure 4-1B).

Viscoelastic formulations were found to replicate experimental force-relaxation curves well (on average r^2 = 0.92), but the early phase of force-relaxation was fit somewhat less accurately by viscoelastic models (gray line, Figure 5-1A) compared to poroelastic fits (black line, Figure 5-1A). Indeed, viscoelastic models gave rise to somewhat larger errors

than poroelastic models (Figure 5-1B). An average apparent viscosity of η = 166±81 Pa.s was measured for HeLa cells, η = 77±37 Pa.s for HT1080 cells and η = 50±15 Pa.s for MDCK cells.

5.2 Poroelasticity can predict changes in stress relaxation in response to volume changes

Having established that poroelastic models provide good fits for stress relaxation in cells, I examined the ability of our simple scaling law to qualitatively predict changes in D_p resulting from changes in pore size due to cell volume change. Indeed, cell volume changes should not affect cytoskeletal organisation or integrity but should alter cytoplasmic pore size. In our experiments, we exposed Hela and MDCK cells to media of different osmolarities: hyperosmotic media to decrease cell volume and hypoosmotic media to increase cell volume.

First, I measured cell volume change in response to changes in osmolarity for up to 30 min to ascertain that volume changes persisted long enough for experimental measurements to be carried out with AFM (Figure 5-2A). Indeed, cell volume stayed constant over this time frame. I verified that photobleaching due to the acquisition of confocal stacks over an extended period of time did not artefactually affect our measurement of cell volume (control, n = 6 cells, Figure 5-2A). Cells regulate their volume tightly to be able to tolerate extracellular environments of different osmolarities. When osmolarity is perturbed, flow of water across cell membrane causes cell swelling or shrinkage. However, the cell can restore its original volume by activation of channels or transporters (typically K+, Cl and organic osmolytes) to lose or gain sufficient amount of osmolytes to return to its preferred volume. To ensure a stable volume increase under hypoosmotic conditions over the timescale necessary for AFM experiments (~ 30 min), cells were treated simultaneously with regulatory volume decrease (RVD) inhibitors

[160]. Also, MDCK cells were treated with regulatory volume increase (RVI) inhibitors to ensure a stable decrease in cell volume after shrinkage. Under these conditions, a stable increase of 22±2% in cell volume was measured after hypoosmotic treatment (n = 3 cells, Figure 5-2A). Conversely, upon addition of 240 mM sucrose, cell volume decreased by 21±6% (n = 10 cells, Figure 5-2A) and upon addition of PEG-400 (30% volumetric concentration), cell volume decreased drastically to 46±3% of the original volume (N = 6 cells, Figure 5-2A)[†].

Next, using AFM indentations I investigated whether changes in cell volume resulted in changes in the poroelastic diffusion constant. Increases in cell volume resulted in a significant increase (55%) in poroelastic diffusion constant D_p and in a significant decrease (-20%) in cellular elasticity E (N = 92 measurements on n = 33 cells, p < 0.01 when compared to control for both E and D_p, Figure 5-2B). In contrast, cells exposed to PEG-400 exhibited a two-fold lower diffusion constant (p < 0.01 when compared to controls) than control cells and a 50% larger elasticity (p < 0.01, N = 176 measurements on n = 17 cells) (Figure 5-2B). Addition of sucrose with low concentrations (<<250 mM) resulted in no significant changes in elasticity or diffusion constant (p = 0.53 for E and p = 0.89 for D_p).

As will be examined in detail in next section, there are spatial inhomogeneities in shape architecture and mechanical properties of HeLa cells spread on glass substrates. To increase the accuracy of the measurements and decrease the uncertainties arising from spatial inhomogeneities, similar experiments were performed on MDCK cells with 8 data points corresponding to sampling different medium osmolarities (Figure 5-2C). Qualitatively, both cell types had the same behaviour, confirming the generality of our results (Figure 5-2C, D).

[†] I would like to acknowledge the preliminary data from report of L. Valon.

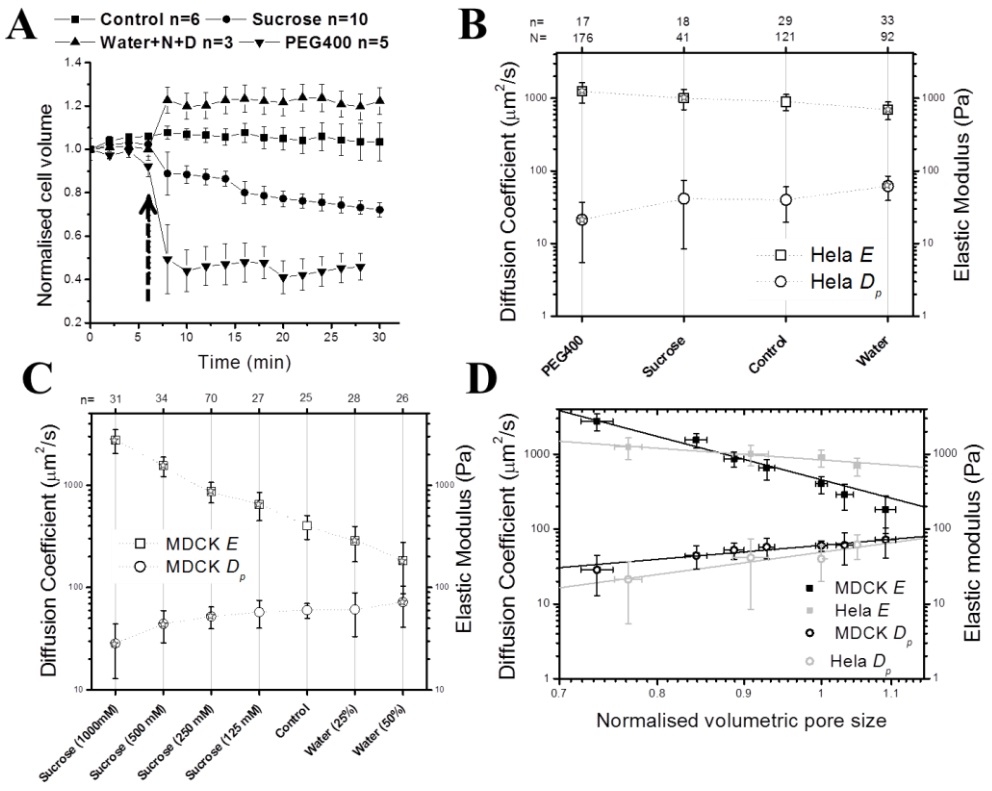

Figure 5-2 Poroelastic and elastic properties change in response to changes in cell volume.

In all graphs, error bars indicate the standard deviation and, in graphs B and C, asterisks indicate significant changes compared to control (p < 0.01). N indicates the total number of measurements and n indicates the number of cells. In hypoosmotic shock experiments, cells were incubated with NPPB and DCPIB (N+D on the graph), inhibitors of RVD. In hyperosmotic shock experiments, MDCK cells were incubated with RVI inhibitors (EIPA). (A) Cell volume change over time in response to changes in extracellular osmolarity. The volume was normalized to the initial cell volume at t = 0 s. The arrow indicates the time of addition of osmolytes. (B) Effect of osmotic treatments on the elasticity E (squares) and poroelastic diffusion constant D_p (circles) in HeLa cells. (C) Effect of osmotic treatments on the elasticity E (squares) and poroelastic diffusion constant D_p (circles) in MDCK cells. (D) D_p and E plotted as a function of the normalised volumetric pore size $\psi \sim (V/V_0)^{1/3}$ in log-log plots for MDCK cells (black squares and circles) and HeLa cells (grey squares and circles). Straight lines were fitted to the experimental data points weighted by the number of measurements to reveal the scaling of D_p and E with changes in volumetric pore size (grey lines for HeLa cells, $E \sim \psi^{-1.6}$ and $D_p \sim \psi^{2.9}$ and black lines for MDCK cells, $E \sim \psi^{-5.9}$ and $D_p \sim \psi^{1.9}$).

Consistent with results reported by others [125], our experiments revealed that cells relaxed less rapidly and became stiffer with decreasing fluid fraction. Increases in cell volume resulted in a significant increase in poroelastic diffusion constant D_p and a significant decrease in cellular elasticity E (Figure 5-2B, C). In contrast, a decrease in cell volume decreased the diffusion constant and increased elasticity (Figure 5-2B, C). Because the exact relationship between hydraulic pore size ξ and cell volume is unknown, D_p and E were plotted as a function of the change in the volumetric pore size $\psi \sim (V / V_0)^{1/3}$. As shown in the log-log plot in Figure 5-2D, for both MDCK and HeLa cells, D_p scaled with ψ and the cellular elasticity E scaled inversely with ψ. In summary, an increase in cell volume increased the poroelastic diffusion constant and decrease in cell volume decreased D_p qualitatively consistent with our simple scaling law.

To exclude any possible indirect effect of volume change due to changes in cytoskeletal organisation, I verified that cytoskeletal structure was not perturbed by changes in cell volume (Figure 5-3 for actin).

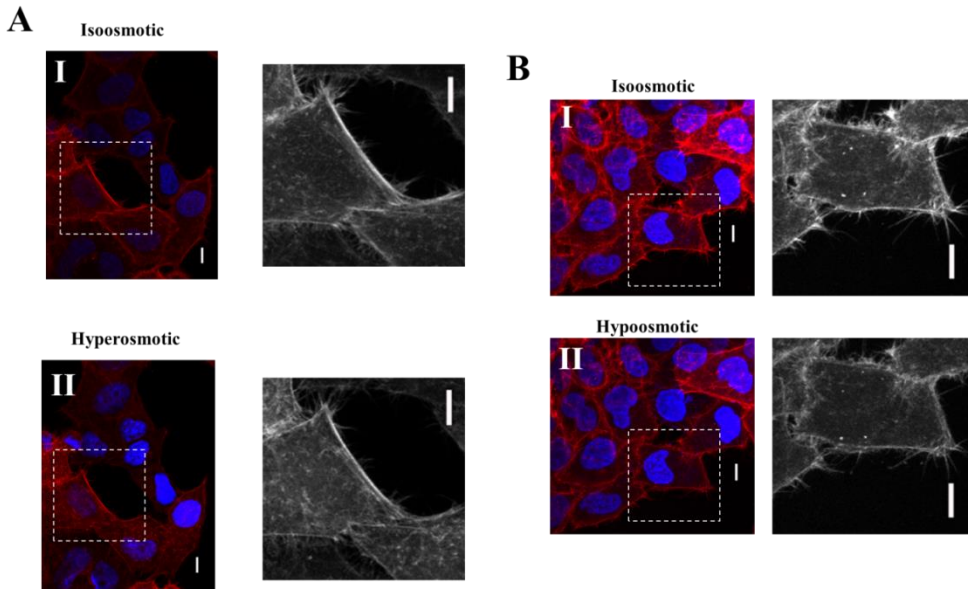

Figure 5-3 Effects of hypoosmotic or hyperosmotic shock on HeLa cells F-actin structural organization.

The F-actin cytoskeleton does not reorganise in response to hypoosmotic treatment (A) or hyperosmotic treatment (B). All images are maximum projections of a confocal image stack of cells expressing Life-act ruby (red). Nuclei were stained with Hoechst 34332 (blue). In A and B, image (I) shows the cell before addition of osmolyte and image (II) after addition. Scale bar = 10 µm. No dramatic changes in structure of actin filaments could be observed after hypoosmotic (A) or hyperosmotic (B) shock.

5.3 Changes in cell volume result in changes in cytoplasmic pore size.

Having shown that changes in cell volume result in changes in the poroelastic diffusion constant without affecting cytoskeletal structure, I tried to directly detect if the volume perturbations resulted in changes of pore size. As shall be described in the following, experiments examining the mobility of microinjected quantum dots (qdots) and photobleaching experiments were performed to show that osmotic perturbations and the concomitant volume changes directly affect the cytoplasmic pore size. Furthermore, as poroelasticity is related to fluid redistribution phenomena, I verified the existence of a

fluid phase in cells under extreme shrinkage conditions by photobleaching of small cytoplasmic fluorescein analogs.

5.3.1 Hyperosmotic shock halts movement of quantum dots inside cytoplasm

PEG-passivated qdots (nanoparticles made of a semiconductor material with unique optical and electrical properties, ~ 14 nm hydrodynamic radius with the PEG-passivation layer [161]) were microinjected into cells and their mobility was examined before and after application of hyperosmotic shock. Under isoosmotic condition, qdots rapidly diffused throughout the cell; however, upon addition of PEG-400, they became immobile (supplementary video 1, Figure 5-5A-I, n = 7 cells examined). Hence, cytoplasmic pore size decreased in response to cell volume decrease trapping qdots in the cytoplasmic solid fraction and immobilising them (Figure 5-5A-II). This suggested that the isoosmotic pore radius ξ was larger than 14 nm, consistent with our estimates from poroelasticity (see section 5.5).

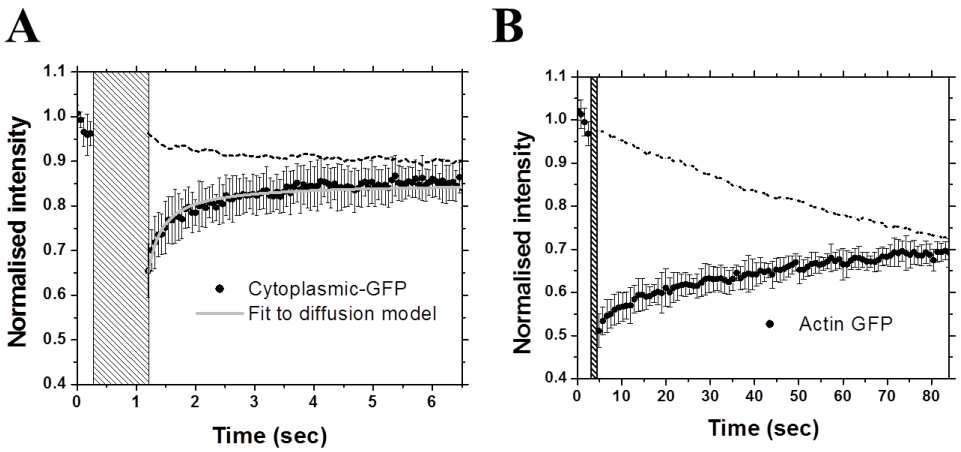

Figure 5-4 Fluorescence recovery after photobleaching in HeLa cells.

(A) Fluorescence recovery after photobleaching of monomeric free diffusing GFP in isosmotic conditions. Solid lines indicate fluorescence recovery after photobleaching and are the average of N = 18 measurements on n = 7 cells. The experimental recovery was fitted with the theoretical model described in Chapter 3.11 (grey line). (B) Fluorescence recovery after photobleaching of GFP-actin in the cortex of HeLa cells blocked in prometaphase. Solid lines indicate fluorescence recovery after photobleaching and are the average of N = 10 measurements on n = 4 cells. A half time recovery of $t_{1/2,\,F-actin}$ = 11.2±3 s was obtained. In (A) and (B), dashed lines indicate loss of fluorescence due to imaging in a region outside of the zone of FRAP, error bars indicate the standard deviation for each time point, and the greyed area indicates the duration of photobleaching.

5.3.2 Translational diffusion of fluorescent probes affected by osmotic perturbations

5.3.2.1 Effective bleach radius in FRAP experiments.

To derive quantitative measurements of the translational diffusion constants of molecules within the cytoplasm using the methods described in [141], I experimentally determined the effective bleach radius in the first post-bleach image for a nominal bleaching zone of diameter 0.5 µm (Figure 3-7III). Averaging over all diameters passing through the centre

of the nominal bleach regions yielded an experimental curve that could be fit with equation (3.11) to find r_e = 1.5±0.2 µm (S5A-V, N = 6 measurements on n = 6 cells).

5.3.2.2 Measurement of translational diffusion constants in cells.

To validate my estimations of the translational diffusion constant D_T using the analytical procedures described in Chapter 3.11, I first measured D_T for GFP molecules and small fluorescein analogs (CMFDA, hydrodynamic radius R_h ~ 0.9 nm [162]) freely diffusing in the cytoplasm. For cytoplasmic GFP molecules, I found $D_{T,GFP}$ ~ 25 µm^2.s^{-1} (Figure 5-4A, N = 18 measurements on n = 7 cells), consistent with values reported by others [141]. I also estimated a translational diffusion constant $D_{T,CMFDA}$ ~ 38 µm^2.s^{-1} for CMFDA (N = 19 measurements on n = 7 cells) which is in a good agreement with published values in cells (Figure 5-5B, D_T = 24-40 µm^2.s^{-1}, [162]). Indeed, effects of molecular crowding and hindered diffusion inside the cell slow the diffusion of GFP and CMFDA by more than ~3 fold compared to diffusion of these analogs in aqueous solutions ($D_{T,GFP,\ aqueous}$ ~ 90 µm^2.s^{-1} and $D_{T,CMFDA,\ aqueous}$ ~ 240 µm^2.s^{-1} [162, 163]). It should be noted that with CMFDA loss of fluorescence due to imaging is very high (also reported by others, Figure 5-5B). Therefore, only data points up to a total fluorescence loss of 15% due to imaging were utilised to estimate the translational diffusion of fluorophores in cells in normal isotonic condition.

5.3.2.3 Osmotic perturbations change the cytoplasmic pore size

In isoosmotic conditions, CMFDA recovered rapidly after photobleaching (black line, Figure 5-5B, Table 5-1) whereas recovery slowed three fold in the presence of PEG-400 consistent with [164] (grey line, Figure 5-5B and Table 5-1). Recovery after photobleaching of CMFDA under strong hyperosmotic conditions confirmed the presence of a fluid-phase indicating that under severe hyperosmotic conditions cells still retained a significant fluid fraction. To estimate the reduction in translational diffusion of CMFDA

in cells under hyperosmotic conditions, I normalised the data following the procedures described in [165] and this gave an estimated value of $D_{T,CMFDA,Hyper}$ ~ 14 μm^2.s^{-1} (N = 20 measurements on n = 5 cells). The measured decrease in translational diffusion suggested a reduction in the cytoplasmic pore size with dehydration. Indeed, translational diffusion is related to the solid fraction ϕ via the empirical relation $D_T / D_{T\infty} \sim \exp(-\phi)$ with $D_{T\infty}$ the translational diffusion constant of the molecule in a dilute isotropic solution [166]. Assuming that the fluid is contained in N pores of equal radius ξ, the solid fraction is $\phi \sim V_s / (V_s + N\xi^3)$ with V_s the volume of the solid fraction, a constant. $D_T / D_{T\infty}$ is therefore a monotonic increasing function of ξ. Therefore the decrease in D_T measured in response to hyperosmotic shock suggests a decrease in ξ. To examine the effect of volume increase on pore size, I examined the fluorescence recovery after photobleaching of a cytoplasmic GFP decamer (EGFP-10x, R_h ~ 7.5 nm). Increases in cell volume resulted in a significant ~ 2-fold increase in D_T (p < 0.01, Figure 5-5C, Table 5-1), suggesting that pore size did increase. Together, our experiments show that changes in cell volume modulate cytoplasmic pore size ξ consistent with estimates from AFM measurements (Figure 5-11).

Table 5-1 Effects of osmotic perturbations on translational diffusion coefficients.
Translation diffusional coefficients D_T are reported with unit of (μm^2.s^{-1}).

GFP	CMFDA	CMFDA	EGFP10x	EGFP10x
Control	Control	PEG-400	Control	Water+N+D
N = 18, n = 7	N = 19, n = 7	N = 20, n = 5	N = 17, n = 6	N = 23, n = 7
24.9±7	38.3±8	13.7±4	8.6±2	15.5±5

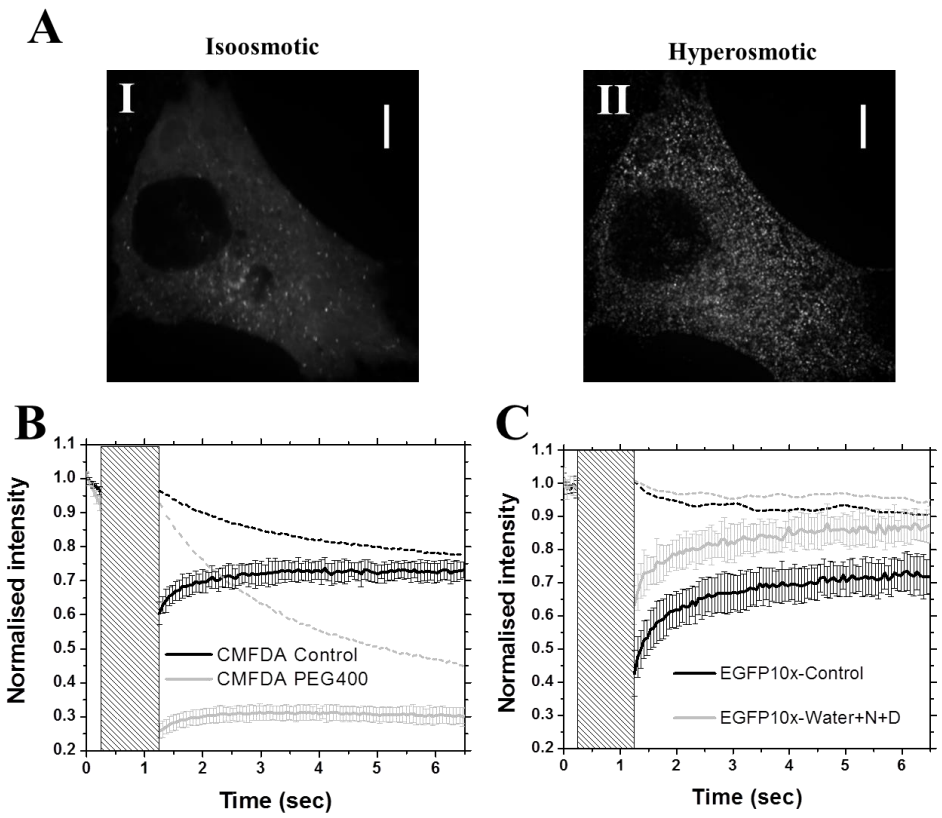

Figure 5-5 Changes in cell volume change cytoplasmic pore size.

(A) Movement of PEG-passivated quantum dots microinjected into HeLa cells in isoosmotic conditions (I) and in hyperosmotic conditions (II). Both images are a projection of 120 frames totalling 18 s (Supplementary movie). In isoosmotic conditions, quantum dots moved freely and the time-projection appeared blurry (I); whereas in hyperosmotic conditions, quantum dots were immobile and the time-projected image allowed individual quantum dots to be identified (II). Images A-I and II are single confocal sections. In (B) and (C), dashed lines indicate loss of fluorescence due to imaging in a region outside of the zone where fluorescence recovery after photobleaching (FRAP) was measured, solid lines indicate fluorescence recovery after photobleaching and are the average of N measurements and error bars indicate the standard deviation for each time point. The greyed area indicates the duration of photobleaching. (B) FRAP of CMFDA (a fluorescein analog) in isoosmotic (black, N = 19 measurements on n = 7 cells) and hyperosmotic conditions (grey, N = 20 measurements on n = 5 cells). In both conditions, fluorescence recovered after photobleaching but the rate of recovery was decreased significantly in hyperosmotic conditions. (C) FRAP of EGFP-10x (a GFP decamer) in isoosmotic (black, N = 17 measurements on n = 6 cells) and hypoosmotic conditions (grey, N = 23 measurements on n = 7 cells). The rate of recovery was increased significantly in hypoosmotic conditions.

5.4 Estimation of the hydraulic pore size from experimental measurements of D_p.

To estimate HeLa cells hydraulic pore size, equation (2.38), $D_p = \alpha E_s \xi^2 / \mu$, can be used. As a first approximation, I considered ν_s ~ 0.3 and a fluid fraction of φ ~ 0.75 for cells in isotonic conditions which yields a Kozney constant of κ ~ 4 assuming the lower bound for a random distribution of particulate spheres [167]. These values yield an estimate of ~ 0.05 for α in isotonic conditions. Multiple experimental reports have shown that for small molecules the viscosity μ (~ 0.001 Pa.s) of the fluid-phase of cytoplasm (cytosol) is 2-3 fold higher in cells than in aqueous media [71, 168]. Using $D_p = \alpha E_s \xi^2 / \mu$, together with our experimental measurements of D_p ~ 40 $\mu m^2.s^{-1}$ and E_s ~ 1 kPa in HeLa cells yields a hydraulic pore size ξ of ~ 15 nm, comparable to the value estimated in section 5.3.

5.5 Spatial variations in poroelastic properties

Maps of cellular elasticity measured by AFM show that E is strongly dependent upon location within the cell with actin-rich organelles (lamellipodium, actin stress fibres) appearing significantly stiffer than other parts of the cell [169]. Hence, I asked if something similar could be observed for poroelastic properties by measuring the cellular poroelastic properties at different locations along the cell long axis (Figure 3-5). I performed N = 386 total measurements on n = 30 cells and displayed the measurements averaged over 2 μm bins as a function of distance to the centroid of the nucleus. Cell height decreased significantly with increasing distance from the nucleus (Figure 5-6A) and this measurement enabled us to exclude low areas of the cell that are prone to measurement artefacts due to the limited thickness. The poroelastic diffusion constant D_p decreased slightly, but not significantly, away from the nucleus going from 40 $\mu m^2.s^{-1}$ to

~ 30 μm^2.s^{-1} (p > 0.02, Figure 5-6C). In contrast, elasticity increased significantly away from the nucleus increasing from ~ 500 Pa to ~ 1200 Pa in lower areas (Figure 5-6B). Finally, the lumped pore size estimated from the ratio $\mu D_p / E^{1/2}$ also decreased significantly away from the nucleus (Figure 5-6D).

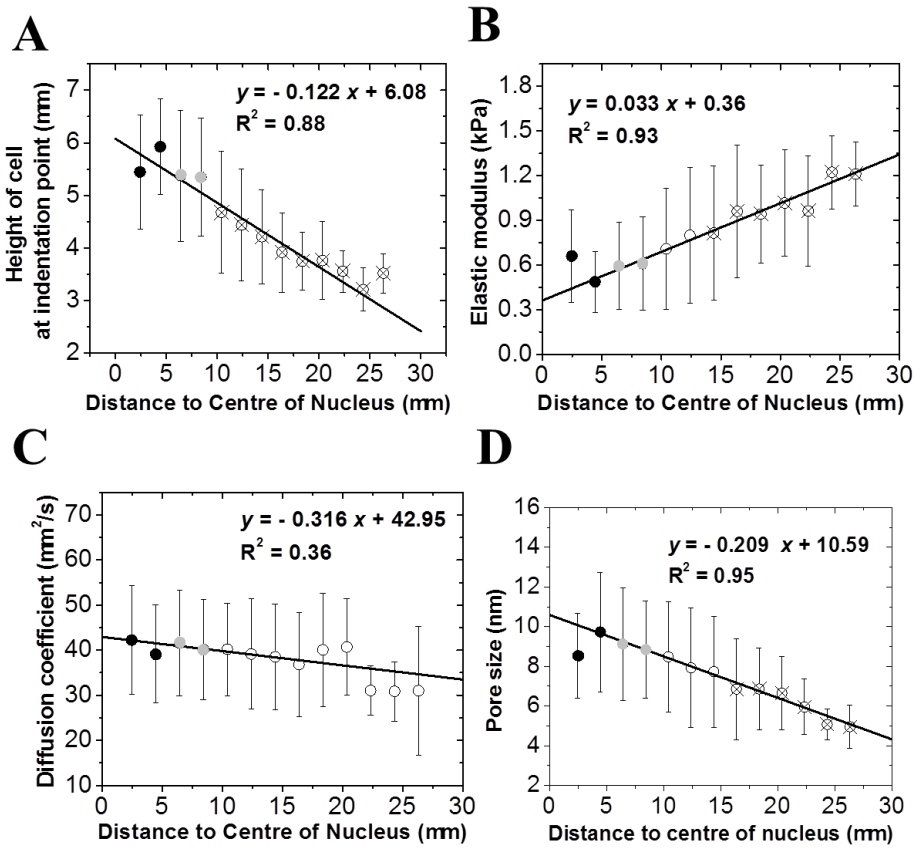

Figure 5-6 Spatial distribution of cellular rheological properties.

(A-D) Scatter plots of the average cell height h, elasticity E, poroelastic diffusion constant D_p, and lumped pore size $\mu D_p / E^{1/2}$ as a function of distance to the centre of nucleus. Each scatter graph is generated by averaging values of each variable over 2 μm wide bins. Filled black circles indicate locations above the nucleus, white unfilled circles in the cytoplasm, and grey filled circles boundary areas. The lines indicate the weighted least-square fit of the scattered data. Unfilled circles with a cross superimposed indicate measurements significantly different (p < 0.01) from those obtained above the nucleus.

5.6 Poroelastic properties are influenced by cytoskeletal integrity

It has been shown previously that cellular poroelastic properties are affected by the cell cycle state of the cell [101]. Specifically, in mitotic cells blocked in metaphase (F-actin and vimentin intermediate filaments concentrate at the cell periphery, microtubules reorganize to form the mitotic spindle and cytokeratin filaments disassemble) a ~ two fold larger poroelastic diffusion constant was measured compared to interphase cells [101]. It has been hypothesized that this may be due to the dramatic reorganization of the cytoskeleton concomitant with metaphase [101]. Cytoskeletal organisation strongly influences cellular elasticity E [169-171], and is also likely to affect the cytoplasmic pore size ξ (Figure 5-7A-C). As both factors (elasticity and pore size) play antagonistic roles in setting D_p, in the following I examined the effect of disruption of the cytoskeleton on the cellular poroelastic properties using chemical and genetic treatments.

5.6.1 Chemical treatments

Treatment of cells with 750 nM latrunculin, a drug that depolymerises the actin cytoskeleton, resulted in a significant decrease in the cellular elastic modulus (Figure 5-9A, consistent with [169]), a ~ two-fold increase in the poroelastic diffusion coefficient (Figure 5-9B), and a significant increase in the lumped pore size (Figure 5-11C). Depolymerisation of microtubules by treatment with 5 μM nocodazole had no significant effect (Figure 5-9 and Figure 5-11C). Stabilisation of microtubules with 350 nM taxol resulted in a small (-16%) but significant decrease in elasticity but did not alter D_p (Figure 5-9 and Figure 5-11C). Perturbation of contractility with the myosin II ATPase inhibitor blebbistatin (100 μM) lead to a 50% increase in D_p, a 70% decrease in E, and a significant increase in lumped pore size (Figure 5-9 and Figure 5-11C)[‡].

[‡] I would like to acknowledge the preliminary data from report of L. Valon.

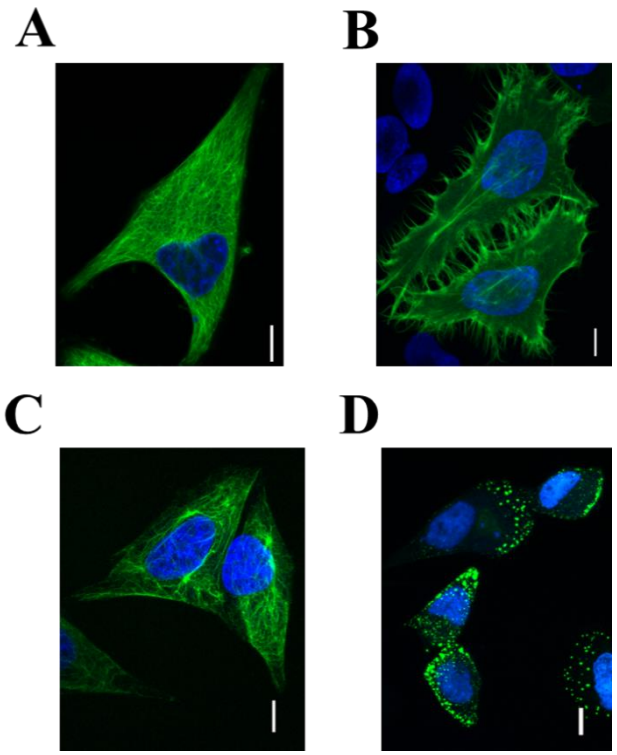

Figure 5-7 Cellular distribution of cytoskeletal fibres.

Scale bars = 10 µm. Nuclei are shown in blue and GFP-tagged cytoskeletal fibres are shown in green. (A) Maximum projection of a cell expressing tubulin-GFP. GFP-α-tubulin was homogenously localised throughout the cell body. (B) Maximum projection of cells expressing Life-act-GFP, an F-actin reporter construct. F-actin was enriched in cell protrusions but was also present in the cell body. (C) Maximum projection of cells expressing keratin18-GFP. Intermediate filaments (keratin 18) were homogenously distributed throughout the cell body. (D) Overexpression of the dominant mutant Keratin 14 R125C resulted in aggregation of the cellular keratin network. (A&B were acquired by L. Valon).

5.6.2 Genetic modification

In light of the dramatic effect of F-actin depolymerisation on D_p and ξ, we attempted to decrease the pore size by expressing a constitutively active mutant of WASp (WASp I294T, CA-WASp) that results in excessive polymerization of F-actin in the cytoplasm through ectopic activation of the arp2/3 complex, an F-actin nucleator (Figure 5-8, [26]). Increased cytoplasmic F-actin due to CA-WASp resulted in a significant decrease in the

poroelastic diffusion coefficient (-43%, p < 0.01, Figure 5-9B), a significant increase in cellular elasticity (+33%, p < 0.01, Figure 5-9A), and a significant decrease in the lumped pore size (-38%, p < 0.01, Figure 5-11C). Similar results were also obtained for HT1080 cells (-49% for D_p, +68% for E and -38% for lumped pore size, p < 0.01).

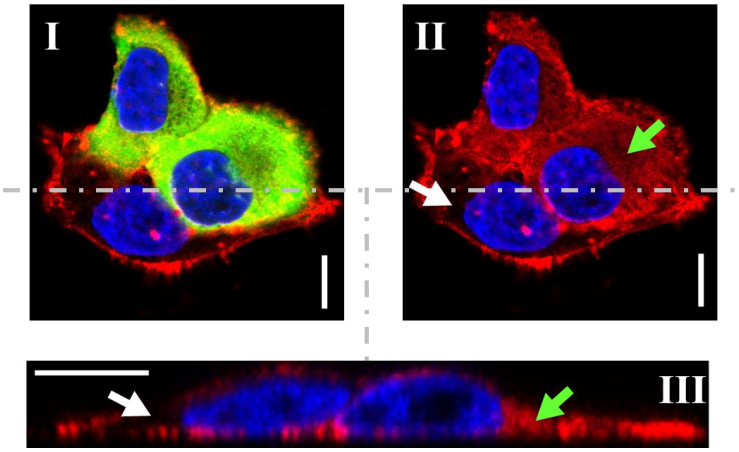

Figure 5-8 Ectopic polymerization of F-actin due to CA-WASp.

HeLa cells were transduced with a lentivirus encoding GFP-CA-WASp (in green) and stained for F-actin with Rhodamine-Phalloidin (in red). Cells expressing high levels of CA-WASp (green, I) had more cytoplasmic F-actin (red, II, green arrow) than cells expressing no CA-WASp (II, white arrow). (III) zx profile of the cells shown in (I) and (II) taken along the dashed line. Cells expressing CA-WASp displayed more intense cytoplasmic F-actin staining (green arrow) than control cells (white arrow). Cortical actin fluorescence levels appeared unchanged. Nuclei are shown in blue. Images I and II are single confocal sections acquired with kind helps from Dr. Moulding. Scale bars = 10 μm.

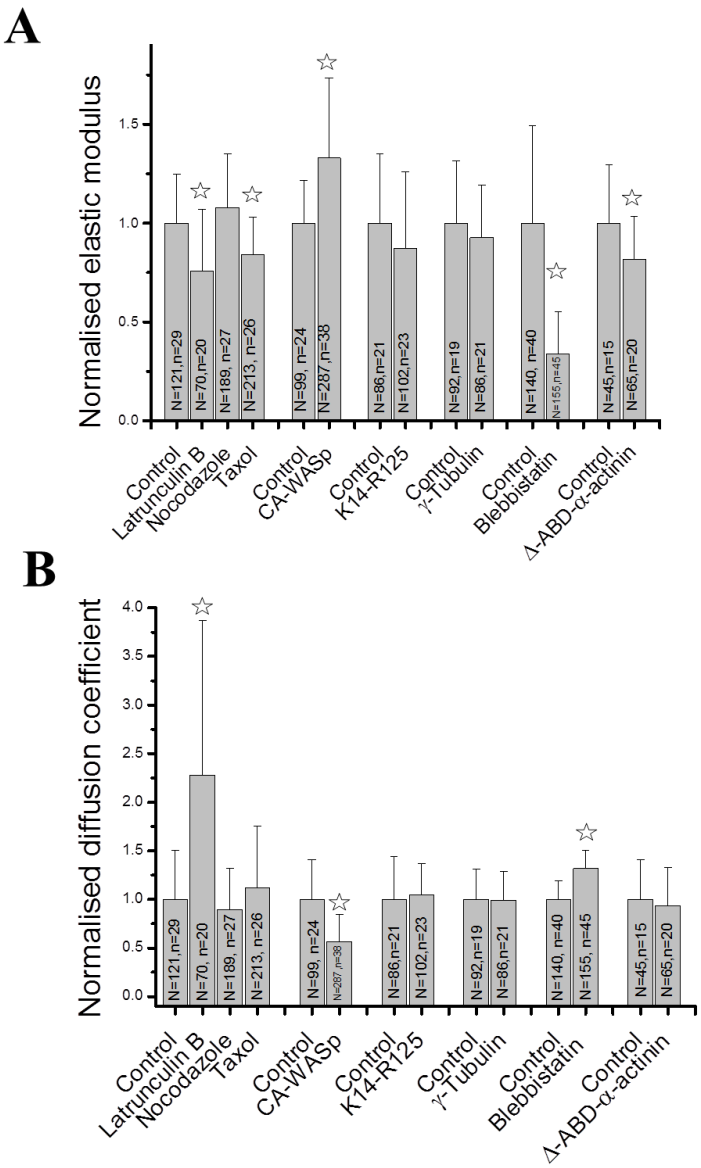

Figure 5-9 Effect of drug treatments and genetic perturbations on poroelastic properties.

Effect of F-actin depolymerisation (Latrunculin treatment), F-actin overpolymerisation (overexpression of CA-WASp), myosin inhibition (blebbistatin treatment), microtubule stabilisation (Taxol treatment), microtubule over-polymerisation (overexpression of γ-tubulin), microtubule depolymerisation (nocodazole treatment), intermediate filaments aggregation (expression of Keratin 14 R125C) and crosslinking perturbation (overexpression of ΔABD-α-actinin) on the cellular elasticity E in (A) and poroelastic diffusion constant D_p in (B). Asterisks indicate significant changes (p < 0.01). N is the total number of measurements and n the number of cells examined.

Then, we attempted to change cell rheology without affecting intracellular F-actin concentration by perturbing crosslinking or contractility. To perturb crosslinking, we overexpressed a deletion mutant of α-actinin (ΔABD-α-actinin) that lacks an actin-binding domain but can still dimerize with endogenous protein [172], reasoning that this should either increase the F-actin gel entanglement length λ or reduce the average diameter of F-actin bundles b (the inverse scenario is depicted in Figure 5-12B). Overexpression of ΔABD-α-actinin led to a significant decrease in E but no change in D_p or lumped pore size (Figure 5-9 and Figure 5-11C). To determine if ectopic polymerisation of microtubules had similar effects to CA-WASp, we overexpressed γ-tubulin, a microtubule nucleator [173], but found that this had no effect on cellular elasticity, poroelastic diffusion constant, or lumped pore size (Figure 5-9 and Figure 5-11C). Finally, expression of a dominant keratin mutant (Keratin 14 R125C, [130]) that causes aggregation of the cellular keratin intermediate filament network had no effect on E, D_p, or lumped pore size (Figure 5-9 and Figure 5-11C).

5.6.2.1 Clinical relevance: Mechanical disruption of mitosis in cells with dysregulated F-actin production:

Dynamic events during cell division, such as the poleward movement of chromosomes or the closure of the cleavage furrow, are mechanical processes that are intrinsically linked to the physical properties of the cell. It is well established that actin is the main cytoskeletal determinant of cellular rheology (as in this thesis under framework of poroelasticity), and provides the physical support to maintain cell shape and drive shape change [169-171]. In some patients, malfunctioning of the WASp protein can lead to severe immunodeficiency, known as x-linked neutropenia. CA-WASp (a constitutive WASp activation) causes increased F-actin production through dysregulated activation of the Arp2/3 complex throughout the cytoplasm, which results in loss of proliferation, high levels of apoptosis, cell division defects and chromosomal instability [26, 27]. In a very recent study, we investigated the role of WASp in cell division and asked if an increased

abundance of F-actin in CA-WASp could cause these defects (Moulding et al, Blood, 2012). We showed that excessive cytoplasmic F-actin increases the elasticity and apparent viscosity of the cytoplasm and mechanically impedes chromosome separation and furrow closure during mitosis. Inhibition of the Arp2/3 complex reduced the change in viscosity, restored the velocity of chromosome movement and reversed the XLN phenotype. Taken together, these results show that non-specific alterations to cellular rheology can lead to disease by perturbing critical functions such as mitosis.

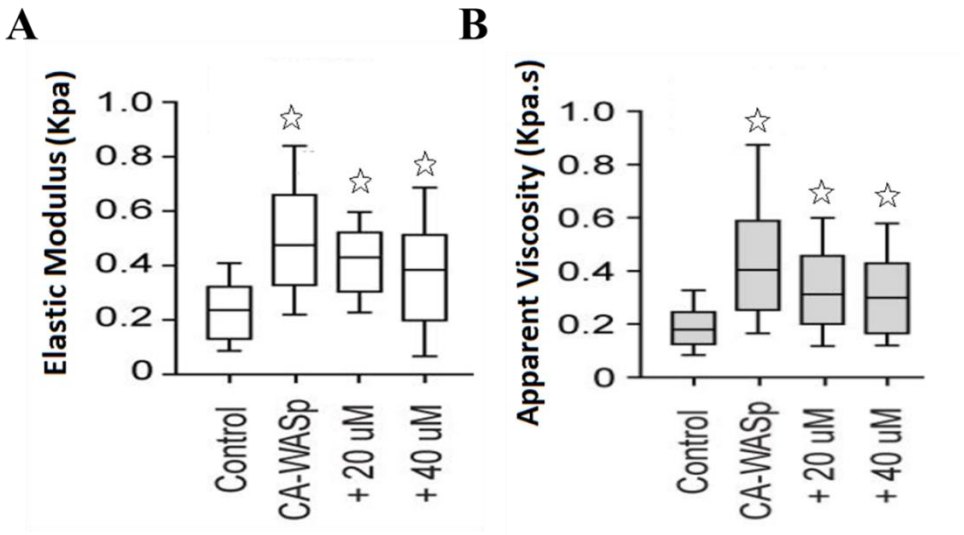

Figure 5-10 Cell rheology and disease.

AFM measurements on HT1080 cells revealed a ~ two-fold increase in both cellular elasticity and apparent cellular viscosity due to CA-WASp expression. Inhibition of the Arp2/3 complex using different concentration of the CK666 drug reduced the amount of cytoplasmic F-actin in CA-WASp cells, leading to partial recovery of the cell rheological properties and reducing cell division defects (Moulding et al, Blood, 2012)

5.7 Discussion and conclusions

I have shown that water redistribution plays a significant role in cellular responses to mechanical stresses and that the effect of osmotic and cytoskeletal perturbations on cellular rheology can be understood in the framework of poroelasticity through a simple scaling law $D_p \sim E\xi^2 / \mu$. I tested the dependence of D_p on the hydraulic pore size ξ by modulating cell volume and showed that D_p scaled proportionally to volume change, consistent with a poroelastic scaling law. Changes in cell volume did not affect cytoskeletal organisation but did modulate pore size. Experiments monitoring the mobility of microinjected quantum dots suggested that ξ was ~ 14 nm consistent with estimates based on measured values for D_p and E. I also confirmed that cellular elasticity scaled inversely with volume change as shown experimentally [125, 174] and theoretically [84] for F-actin gels and cells. However, the exact relationship between the poroelastic diffusion constant D_p and the hydraulic pore size ξ could not be tested experimentally because the relationship between volumetric change and change in ξ is unknown due to the complex nature of the solid phase of the cytoplasm (composed of the cytoskeletal gel, organelles, and macromolecules, Figure 5-12A, [175]). Taken together, the results show that, for time-scales up to ~ 0.5 s, the dynamics of cellular force-relaxation is consistent with a poroelastic behaviour for cells and that changes in cellular volume resulted in changes in D_p due to changes in ξ.

Although the cytoskeleton plays a fundamental role in modulating cellular elasticity and rheology, our studies (it should be note that the indentation method that is used here only probes local rheological properties of the cell) show that microtubules and keratin intermediate filaments do not play a significant role in setting cellular rheological properties (Figure 5-9 and Figure 5-11C). In contrast, both the poroelastic diffusion constant and elasticity strongly depended on actomyosin (Figure 5-9). The experiments

qualitatively illustrate the relative importance of ξ and E in determining D_p. Depolymerising the F-actin cytoskeleton decreased E and increased pore size resulting in an overall increase in D_p. Conversely, when actin was ectopically polymerised in the cytoplasm by arp2/3 activation by CA-WASp (Figure 5-8), E increased and the pore size decreased resulting in a decrease in D_p. For both perturbations, changes in pore size ξ dominated over changes in cellular elasticity in setting D_p. For dense crosslinked F-actin gels, theoretical relationships between the entanglement length λ and the elasticity E suggest that $E \sim \kappa^2 / (k_B T \lambda^5)$ with κ the bending rigidity of the average F-actin bundle of diameter b, k_B the Boltzmann constant, and T the temperature [84] (Figure 5-12A). If the hydraulic pore size ξ and the cytoskeletal entanglement length λ were identical, D_p would scale as $D_p \sim \kappa^2 / (\mu k_B T \lambda^3)$ implying that changes in elastic modulus would dominate over changes in pore size, in direct contradiction with our results. Hence, ξ and λ are different and ξ may be influenced both by the cytoskeleton and macromolecular crowding [175] (Figure 5-12A).

To decouple changes in elasticity from gross changes in intracellular F-actin concentration, we decreased E by reducing F-actin crosslinking through overexpression of a mutant α-actinin [172] that can either increase the entanglement length λ or decrease the bending rigidity κ of F-actin bundles by diminishing their average diameter b (Figure 5-12). Overexpression of mutant α-actinin led to a decrease in E but no detectable change in D_p or ξ confirming that pore size dominates over elasticity in determining cell rheology. Finally, myosin inhibition led to an increase in D_p, a decrease in E, and an increase in ξ, indicating that myosin contractility participates in setting rheology through application of pre-stress to the cellular F-actin mesh [176], something that results directly or indirectly in a reduction in pore size (Figure 5-12B, [176, 177]). Taken together, these results show that F-actin plays a fundamental role in modulating cellular rheology but further work will be necessary to understand the relationship

between hydraulic pore size ξ, cytoskeletal entanglement length λ, crosslinking, and contractility in living cells.

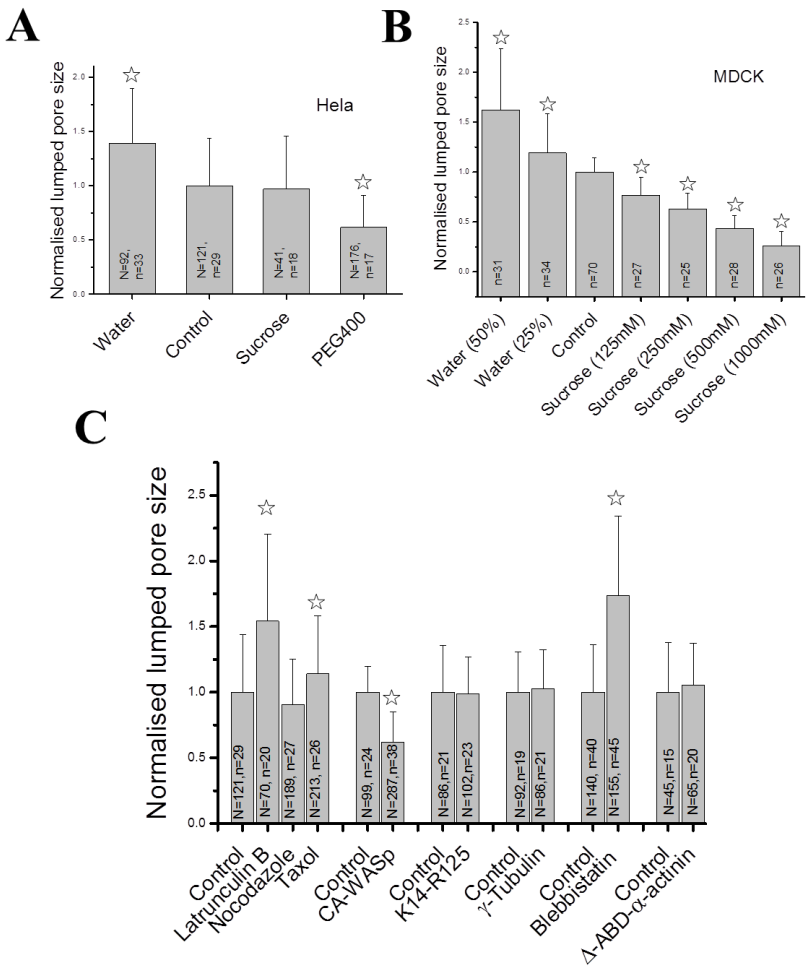

Figure 5-11 Effect of volume changes, chemical and genetic treatments on the lumped pore size.

Effect of volume changes, on lumped pore size of HeLa cells in (A) and MDCK cells in (B). (C) Effect of drug treatments and genetic perturbations on the lumped pore size of Hela cells. The lumped pore size was estimated from the ratio $(D_p\mu/E)^{1/2}$. Asterisks indicate significant changes (p < 0.01). N is the total number of measurements and n the number of cells examined.

Recent experiments using magnetic bead twisting rheometry have demonstrated the existence of at least two regimes in the rheology of living cells [80, 178] and in vitro cytoskeletal networks of actomyosin [176]. At high frequencies (5 Hz - 10 kHz), the cellular dynamic modulus increased with frequency; whereas at lower frequencies (0.1-5Hz) it appeared to be frequency independent. At high frequencies (~ 1 kHz), fast thermal fluctuations give rise to bending of cytoskeletal filaments and determine the cellular mechanical properties [80]. However, at longer time-scales (0.2 s to hundreds of s) cytoskeletal turnover or water movement may influence cell rheology. Measurements of cell rheology obtained using different techniques over time-scales of 1-100 s reveal the existence of different regimes: one with a short time-scale (~ 1 s) and the other with a long time-scale (~ 10 s) [51, 52, 68]. Over the time-scales of the experiments described in this thesis (~ 5 s), other factors such as turnover of cytoskeletal fibres and cytoskeletal network rearrangements due to crosslinker exchange or myosin contractility might also in principle influence cell rheology. In the cells studied here, F-actin, the main cytoskeletal determinant of cellular rheology (Figure 5-9 and [62, 179]), turned over with a half-time of ~ 11 s (Figure 5-4B), crosslinkers turned over in ~ 20 s [180], and myosin inhibition led to faster force-relaxation. Hence, active biological remodelling cannot account for the dissipative effects observed in our force-relaxation experiments. Taken together, the time-scale of force-relaxation, the functional form of force-relaxation, and the qualitative agreement between the theoretical scaling of D_p with experimental changes to E and ξ support our hypothesis that water redistribution is the principal source of dissipation at short time-scales contributing ~ 50% of total relaxation in ~ 0.2 s in our experiments.

In both viscoelastic and poroelastic models, force decays exponentially with time during stress-relaxation (see equations (3.5) and (3.6)). Hence, equating the exponents and recalling $k_1 \sim E$, I obtain the following relationship for a length-scale dependent effective cellular viscosity η:

$$\eta \sim \mu\left(\frac{L}{\xi}\right)^2 \tag{5.1}$$

with L the characteristic length-scale and μ the viscosity of cytosol. The dependence of η on the ratio of a mesoscopic length-scale to a microscopic length-scale in the system may explain the large spread in reported measurements of cytoplasmic viscosities [58, 68] (ranging from ~ 0.1 to 500 pa.s using different rheological measurements such as magnetic twisting cytometry [33] and AFM indentation [51, 54] experiments).

Within the poroelastic regime, further intuition for the complexity and variety of length scales involved in setting cellular rheology (Figure 5-12A) can be gained by recognising that the effective viscosity μ experienced by a particle diffusing in the cytosol will depend on its size (Figure 5-5, [70, 72]). Within the cellular fluid fraction, there exists a wide distribution of particle sizes with a lower limit on the radius set by the radius of water molecules. Whereas measuring the poroelastic diffusion constant D_p remains challenging, the diffusivity D_m of any given particle can be measured accurately in cells with experimental techniques such as the presented FRAP technique. For a molecule of radius a, the Stokes-Einstein relationship gives $D_m = k_B T/(6\pi\mu a)$ or $\mu(a) = k_B T/(6\pi D_m a)$. Any interaction between the molecule and its environment (e.g. reaction with other molecules, crowding and hydrodynamic interactions [181], size-exclusion [70]) will result in a deviation of the experimentally determined D_m from this relationship. Using the relationship for elasticity of gels $E \sim \kappa^2/(k_B T\lambda^5)$ and recalling that the bending rigidity of filaments scales as $\kappa \sim E_{polymer} b^4$ (with b the average

diameter of a filament –or bundle of filaments-, and $E_{polymer}$ the elasticity of the polymeric material [182]), yields the relationship

$$D_p \sim \left(\frac{\xi^2 a E_{polymer}^2 b^8}{(k_B T)^2 \lambda^5} \right) D_m \tag{5.2}$$

in which four different length-scales contribute to setting cellular rheology. We see that the average filament bundle diameter b, the size of the largest particles in the cytosol a (and indeed the particle size distribution in the cytosol), the entanglement length λ, and the hydraulic pore size b conspire to determine the geometric, transport, and rheological complexity of the cell (Figure 5-12A). Since all these parameters can be dynamically controlled by the cell, it is perhaps not surprising that a rich range of rheologies has been experimentally observed in cells [32, 33, 56, 58, 63-65, 68, 79, 80].

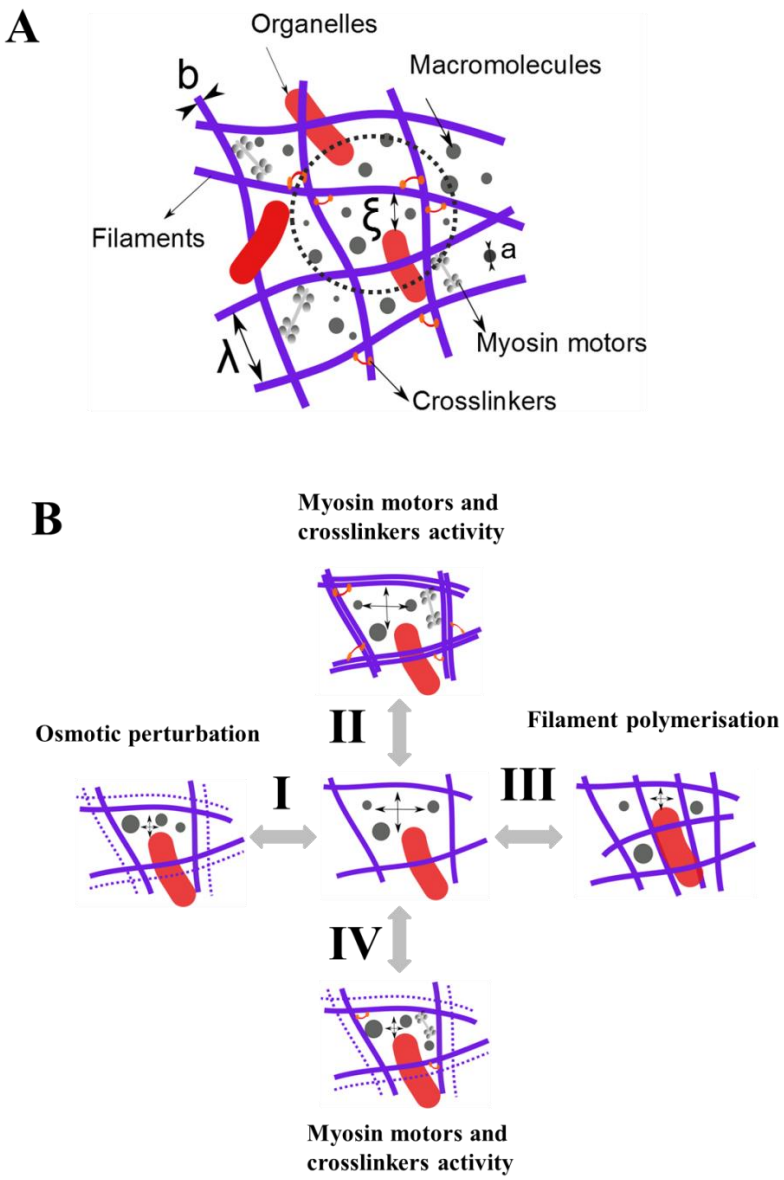

Figure 5-12 Schematic representation of the cytoplasm and effects of different cellular perturbations.

(A) The cytoskeleton and macromolecular crowding participate in setting the hydraulic pore size through which water can diffuse. The length-scales involved in setting cellular rheology are the average filament diameter b, the size a of particles in the cytosol, the hydraulic pore size ξ, and the entanglement length λ of the cytoskeleton. (B) Effects of different perturbations on cell rheology. (I, III) Reduction in cell volume (I) or increase in F-actin concentration (III) causes a decrease in cytoskeletal mesh size λ and an increase in crowding which combined lead to a decrease in hydraulic pore size ξ. (II, IV) Increase in activity of myosin motors or crosslinkers lead to either contraction of F-actin network (decrease in mesh size) or increase in bending rigidity of actin cytoskeleton, which combined results in an increase in the elasticity E of the network and a decrease in the hydraulic pore size ξ.

Chapter 6

General discussion and future work

6.1 Further discussion

6.1.1 Cell rheology and its complexity

Living cells are complex materials displaying a high degree of structural hierarchy and heterogeneity coupled with active biochemical processes that constantly remodel their internal structure. Therefore, perhaps unsurprisingly, they display an astonishing variety of rheological behaviours depending on amplitude, frequency and spatial location of loading. Over the years, a rich phenomenology of rheological behaviours has been uncovered in cells such as scale-free power law rheology, strain stiffening, anomalous diffusion, and rejuvenation (see Chapter 1.4.3 and [56, 58, 63-65]).

Several theoretical models have been proposed to explain the observed behaviours but finding a unifying theory has been difficult because different microrheological

measurement techniques excite different modes of relaxation [58]. These rheological models range from those that treat the cytoplasm as a single phase material whose rheology is described using networks of spring and dashpots [68, 79], to the sophisticated soft glassy rheology (SGR) models that describe cells as being akin to soft glassy materials close to a glass transition [33, 80]; in either case, the underlying geometrical and biophysical phenomena remain poorly defined [58, 63, 64]. Furthermore, none of the models proposed, account for dilatational changes in the multiphase material that is the cytoplasm; these volumetric deformations are ubiquitous in the context of phenomena such as blebbing, cell oscillations or cell movement [100, 150], and in gels of purified cytoskeletal proteins [32] whose macroscopic rheological properties depend on the gel structural parameters and its interaction with an interstitial fluid [81, 84, 176]. Any unified theoretical framework that aims to capture the rheological behaviours of cells and links these behaviours to cellular structural and biological parameters must account for both the shear and dilatational effects seen in cell mechanics as well as account for the role of crowding and active processes in cells.

6.1.2 Why poroelasticity?

The flow of water plays a critical part in such processes. Recent experiments suggest that pressure equilibrates slowly within cells (~10s) [100, 101, 103] giving rise to intracellular flows of cytosol [150, 183] that cells may exploit to create lamellipodial protrusions [150] or blebs [100, 102] for locomotion [184]. Furthermore, the resistance to water flow through the soft porous structure serves to slow motion in a simple and ubiquitous way that does not depend on the details of structural viscous dissipation in the cytoplasmic network. Based on these observations, a coarse-grained biphasic description of the cytoplasm as a porous elastic solid meshwork bathed in an interstitial fluid (e.g. poroelasticity [116] or the two-fluid model [185]) has been proposed as a minimal framework for capturing the essence of cytoplasmic rheology [59, 100, 101]. In the framework of poroelasticity, coarse graining of the physical parameters dictating cellular

rheology accounts for the effects of the interstitial fluid and related volume changes, macromolecular crowding and a cytoskeletal network [100, 101, 105], consistent with the rheological properties of the cell on the time-scales needed for redistribution of intracellular fluids in response to localised deformation. The response of cells to deformation then depends only on the poroelastic diffusion constant D_p, with larger values corresponding to more rapid stress relaxations. This single parameter scales as $D_p \sim E\xi^2/\mu$, allowing changes in cellular rheology to be predicted in response to changes in E, ξ, and μ.

The principal shortcoming of most models of cell rheology is that they do not relate the measured rheological properties to structural or biological parameters within the cell meaning that they lack predictive power. As a coarse-grained bottom-up approach, one advantage of using poroelasticity over other phenomenological models is that it allows cellular rheology to be related to observable physical and biological parameters, making it mechanistic and thus giving it predictive power (see Figure 6-1). In this work, I sought to understand cell rheology at physiologically relevant time-scales and to attempt to understand the cellular biological and physical variables that affect it. By nature, cellular rheology is bound to be extremely complex but my goal was to capture its essence with as few physical parameters as possible. The poroelastic model of the cytoplasm presented here is a first step in this direction. It takes as inputs measurable geometric and physical parameters and leads to falsifiable predictions (see Figure 6-1). This represents a conceptual advance and a step towards describing the experimental observations with the fewest physiologically and biologically relevant parameters possible.

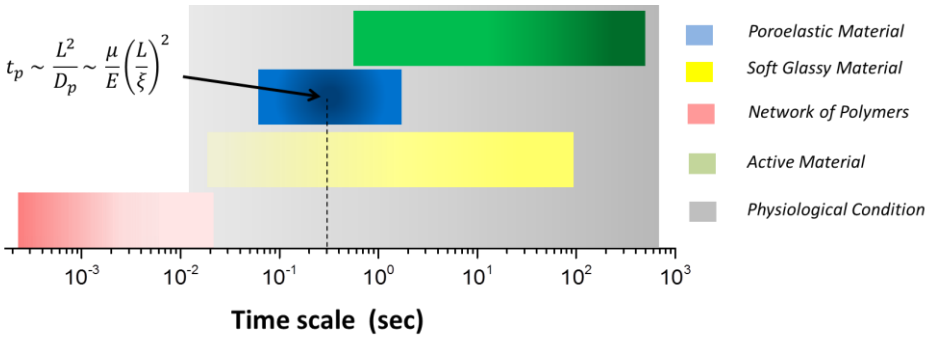

Figure 6-1 Microstructural parameters and mesoscopic length scale set the poroelastic time scale.

Different timescales associated with different rheological models are involved in setting cell rheology. The time-dependent mechanics of cells arise from the combination of several distinct rheological behaviours. These rheological behaviours give rise to different dynamics that coexist but each dominates over a range of timescales. At very short time scales, the behaviour of network of semiflexible filaments (entropic and enthalpic fluctuations) sets the rheology of the cytoplasm [80]. At long timescales, the cytoplasm exhibits inelastic structural rearrangements and behaves as a soft glassy material [80]. At very long timescales the cell can no longer be considered as a passive material and active processes such as molecular motor activities and cytoskeletal filament turnover come into play. Depending on the length scale and time scale, cytosolic flows and intracellular fluid redistribution (poroelastic effects) can affect the rheological behaviour of the cell. The mesoscopic length scale of the system L, the elastic modulus of cell E, the hydraulic pore size of the cytoplasm ξ, and the cytosolic viscosity μ set the characteristic poroelastic timescale t_p ($t_p \sim 0.2$ s in my AFM indentation experiments).

Time dependent mechanics of cells is the manifestation of several cell rheological behaviours and these rheological behaviours give rise to different dynamics that could coexist but each dominates on different timescales. In particular, poroelastic cellular behaviours, in which dissipations are due to water redistribution, are both timescale and lengthscale dependent allowing us to tune the experimental setup in such a way that we observe weak or strong poroelastic effects accordingly. The idea of designing this study was to consider a minimal poroelastic model under optimised experimental conditions, and determine whether this minimal model was sufficient to grasp the essence of cellular rheology and predict changes in rheology in response to perturbations. Extra complexity could be added to the model to take into account more complex properties of the cytoskeleton and cytoplasm or network tension: we could consider a solid phase with

intrinsic viscoelasticity and/or granularity instead of a simple linear elastic meshwork. However, this would come at the expense of introducing more parameters and extra uncertainty as one would have to make many more assumptions about cell mechanics and the end result would not necessarily draw a clearer description of cell rheology and its origins. In particular, because the exact relationship between fluid fraction, volumetric pore size ψ, hydraulic pore size ξ, and cytoskeletal entanglement length λ is still unknown for living cells, rather than making complex hypotheses about the poroelastic scaling law, the trends of my experimental results were validated.

Future studies should concentrate on implementing more realistic cytoskeletal and cytoplasmic properties. However addition of extra complexity should be coupled with experimental determination/validation of all newly introduced variables and this might require much more sophisticated experiments.

6.1.3 Direct physiological relevance

To gain an understanding of how widespread poroelastic effects are in the rheology of isolated cells and cells within tissues, we can compute the poroelastic Péclet number $\mathrm{P_e} = (VL)/D_p$, with V a characteristic velocity (due to active movement, external loading, etc). For $\mathrm{P_e}$ large compared to 1, poroelastic effects dominate the viscoelastic response of the cytoplasm to shape change due to externally applied loading or intrinsic cellular forces. In isolated cells, poroelastic effects have been implicated in the formation of protrusions such as lamellipodia or blebs [100]. For these, the rate of protrusion growth can be chosen as a characteristic velocity. In rapidly moving cells, forward-directed intracellular water flows [150, 183] resulting from pressure gradients due to myosin contraction of the cell rear have been proposed to participate in lamellipodial protrusion [150, 186]. Assuming a representative lamellipodium length of L ~10 μm and protrusion velocities of V ~ 0.3 μm.s^{-1}, poroelastic effects will play an important role if $D_p \leq 3$ μm^2.s^{-1}, lower than measured in the cytoplasm but consistent with the far higher F-actin

density observed in electron micrographs of the lamellipodium [184]. Furthermore, cells can also migrate using blebbing motility [107] where large quasi-spherical blebs (L ~10μm) arise at the cell front with protrusion rates of V ~ 1 μm.s^{-1} giving an estimate of D_p ~ 10 μm^2.s^{-1} (comparable to the values reported in previous Chapter) to obtain $\mathrm{P_e} \geq 1$.

During normal physiological function, cells within tissues of the respiratory and cardiovascular systems are subjected to strains ε > 20% applied at strain rates ε_t > 20%. s^{-1}. As a first approximation, we assume that these cells, with a representative length L_{cell}, undergo a length change $L \sim \varepsilon L_{\mathrm{cell}}$ applied with a characteristic velocity $V \sim \varepsilon_t L_{\mathrm{cell}}$. For cells within the lung alveola [155], L_{cell} ~ 30 μm, ε ~ 20%, ε_t ~ 20%. s^{-1} and assuming D_p ~ 10 μm^2.s^{-1} (based on our measurements), we find $\mathrm{P_e}$ ~ 3. Hence, these simple estimates of $\mathrm{P_e}$ suggest that water redistribution participates in setting the rheology of cells within tissues under normal physiological conditions.

6.2 Future work

6.2.1 Stress and pressure wave propagation in cells

It is well established that cells can sense mechanical forces, react to them, and adapt to them [58]. However, how these forces are sensed and in particular what physical variable is detected by cells remains unclear. A better understanding of cell rheology will allow us to predict the intracellular stress distribution induced by extracellular application of force.

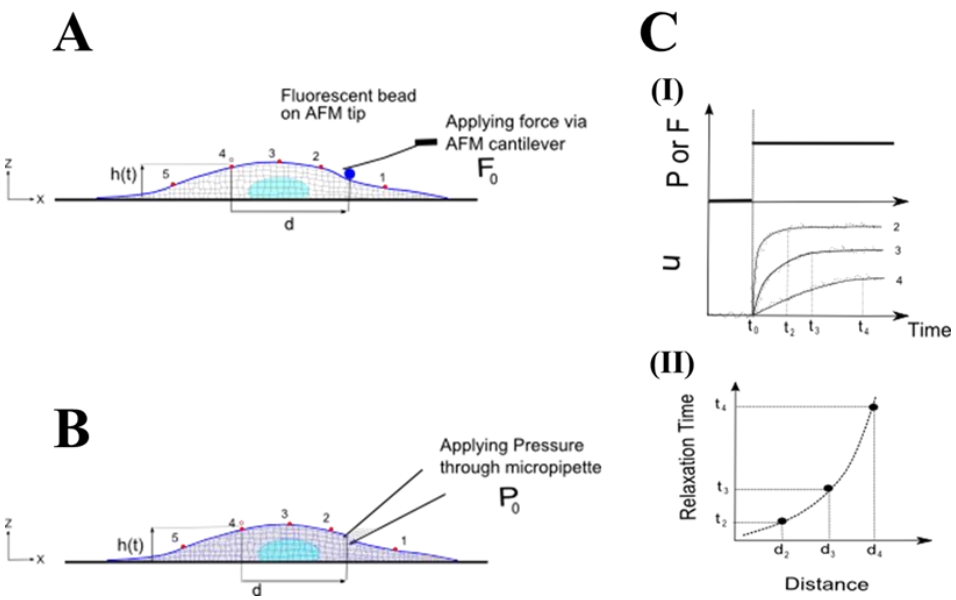

Figure 6-2 Stress and pressure wave propagation in cells

Application of step force/pressure via AFM cantilever (A) or through micropipette (B). Upon application of force/pressure the stress and pressure propagate intracellularly. (C-I) The displacement of each fluorescent bead in the z direction is monitored as a function of time and the bead distance from the force/pressure application point is measured. The bead displacement relaxation time increases with distance from the source. (C-II) Expected curve for the relaxation time as a function of distance. This curve can provide information about how fast stress/pressure propagates through the cytoplasm. Comparing these experimental data with viscoelastic and poroelastic models will provide information about the physical nature of force transmission inside the cytoplasm.

In the future, matching the temporal evolution of this intracellular stress distribution with biological readouts (such as the intracellular calcium concentration or the turnover rates of cytoskeletal proteins) should allow us to better understand what physical variable cells sense and how it is sensed at the molecular level prior to conversion into a biochemical signal. In particular, recent experiments suggest that poroelastic effects lead to slow stress propagation within living cells [103]. In an attempt to understand how stresses propagate inside the cytoplasm, future work will try to apply localized force or pressure onto the cell via an AFM cantilever or through a micropipette (see Figure 6-2A, B). The particle

tracking technique as described in Chapter 3.10 will be used to monitor motion of attached beads at different distances from the point of exerted force/pressure. Studying the relaxation curves as a function of distance (see Figure 6-2C) will provide information about how fast stress/pressure propagates through the cytoplasm. Comparing these experimental data with viscoelastic and poroelastic models will provide useful information about which physical mechanism are effectively involved in force transmission inside the cytoplasm.

6.2.2 Cells as multi-layered poroelastic materials

From a hydrodynamic perspective, the cell can be viewed as a multilayer composite composed of plasma membrane attached to the subcortical actin gel surrounding a molecularly crowded environment saturated with cytosol. One future challenge will be to dissect the contribution of each layer of the cell to cell rheology. In Chapter 5, AFM indentation tests identified the actin cytoskeleton as the main component of the cytoplasm that affected the poroelastic rheology of the cell. It would be interesting to investigate the contribution of the different layers of the cell to the swelling/shrinking experiments presented in Chapter 4.2. In particular, my preliminary experimental results (not presented here) suggested that the plasma membrane can play a significant role in setting the dynamics of cell swelling/shrinking.

I propose to use defocusing microscopy to study the kinetics of cell swelling/shrinking under different types of perturbations to investigate the multi-layered poroelastic nature of the cell and to see if the contribution of each layer in cell rheology can be dissected. First, to examine the role of membrane permeability, cells can be treated with small concentration of mild detergents or pore forming proteins such as Digitonin or Amphotericin B to make small holes in the membrane. It should be noted that after membrane permeabilisation the cell will start swelling. As examined in Chapter 5, swelling can affect the poroelastic properties (specifically pore size) significantly and therefore to counterbalance the effects of cell swelling upon membrane permeabilisation,

a small concentration of osmolyte such as sucrose must be added to retain the isoosmotic cell volume. I would expect the poroelastic diffusion coefficient to increase when the membrane is permeabilised but the extent to which it increases will tell us about the importance of membrane. Next, the effects of macromolecular crowding can be envisaged by using higher concentrations of detergents to create holes large enough for macromolecules to escape (up to micrometres in size). It should be noted that creation of large holes in membrane might result in clearance of some of the basic components of the cytoskeleton (such as actin monomers) that will affect the structure of filaments and consequently the the cellular poroelastic properties.

Second, I will investigate the contribution of the actin cytosleketon to swelling/shrinking dynamics by using drugs such as latrunculin B to depolymerise the actin filaments or performing genetic treatments (as explained in Chapter 3.2) to induce excessive polymerization of F-actin in the cytoplasm. Treatment of cells with drugs such as latrunculin B will affect the structure of the whole actin cytoskeleton including the organization of cortical actin. Therefore, to study the role of cell cortex in setting cell rheology and poroelastic properties separately and in particular to solely perturb structure and organization of the cortical actin, it would be very interesting to conduct more targeted perturbations such as shRNA gene depletion to knock down the protein Diaph1 (a protein shown by other members of the laboratory to be responsible for polymerisation of actin filaments in the cortex) or using the drug CK666 to inhibit the Arp2/3 complex that alsoregulates the structure of the actin network.

6.3 Conclusions

The main conclusions arising from this work may be summarised as follows:

- The time-dependent mechanics of living cells exhibit poroelastic behaviours similar to poroelastic physical gels.
- The dynamics of cell swelling and shrinking can be well described under the framework of poroelasticity.
- Poroelasticity predicts changes in rheology due to cell volume changes and cytoskeletal disruption.
- F-actin and molecular crowding are the main cytoskeletal contributors of poroelastic cellular rheology and together they set the rheological properties of the cell.
- In my experiments, the observed short timescale (0.1-1 s) cellular viscosity is due to water redistribution in the cell.

References

[1] Boal DH (2002) *Mechanics of the Cell* (Cambridge Univ Pr).

[2] Howard J (2001) Mechanics of motor proteins and the cytoskeleton.

[3] Alberts B, Johnson A, Lewis J, Raff M, Roberts K, & Walter P (2002) *Molecular biology of the cell* (Garland Science).

[4] Mofrad MRK & Kamm RD (2006) Cytoskeletal Mechanics - Models and Measurements. (Cambridge University Press).

[5] Bray D (2001) *Cell movements: from molecules to motility* (Routledge).

[6] Desai A & Mitchison TJ (1997) Microtubule polymerization dynamics. *Annual review of cell and developmental biology* 13(1):83-117.

[7] Brangwynne CP, MacKintosh FC, Kumar S, Geisse NA, Talbot J, Mahadevan L, Parker KK, Ingber DE, & Weitz DA (2006) Microtubules can bear enhanced compressive loads in living cells because of lateral reinforcement. *The Journal of cell biology* 173(5):733.

[8] Herrmann H, Bär H, Kreplak L, Strelkov SV, & Aebi U (2007) Intermediate filaments: from cell architecture to nanomechanics. *Nature Reviews Molecular Cell Biology* 8(7):562-573.

[9] Kölsch A, Windoffer R, Würflinger T, Aach T, & Leube RE (2010) The keratin-filament cycle of assembly and disassembly. *Journal of Cell Science* 123(13):2266.

[10] Goldman RD, Clement S, Khuon S, Moir R, Trejo-Skalli A, Spann T, & Yoon M (1998) Intermediate filament cytoskeletal system: dynamic and mechanical properties. *Biological Bulletin* 194(3):361-363.

[11] Theriot JA, Mitchison TJ, Tilney LG, & Portnoy DA (1992) The rate of actin-based motility of intracellular Listeria monocytogenes equals the rate of actin polymerization. *Nature* 357(6375):257-260.

[12] Theriot JA & Mitchison TJ (1991) Actin microfilament dynamics in locomoting cells. *Nature* 352(6331):126-131.

[13] Watanabe N & Mitchison TJ (2002) Single-molecule speckle analysis of actin filament turnover in lamellipodia. *Science* 295(5557):1083.

[14] Tseng Y, Kole TP, Lee JSH, Fedorov E, Almo SC, Schafer BW, & Wirtz D (2005) How actin crosslinking and bundling proteins cooperate to generate an enhanced cell mechanical response. *Biochemical and biophysical research communications* 334(1):183-192.

[15] Edlund M, Lotano MA, & Otey CA (2001) Dynamics of α-actinin in focal adhesions and stress fibers visualized with α-actinin-green fluorescent protein. *Cell motility and the cytoskeleton* 48(3):190-200.

[16] Sanger JM, Mittal B, Pochapin MB, & Sanger JW (1987) Stress fiber and cleavage furrow formation in living cells microinjected with fluorescently labeled α-actinin. *Cell motility and the cytoskeleton* 7(3):209-220.

[17] Lieleg O, Claessens MMAE, & Bausch AR (2010) Structure and dynamics of cross-linked actin networks. *Soft Matter* 6(2):218-225.

[18] Bendix PM, Koenderink GH, Cuvelier D, Dogic Z, Koeleman BN, Brieher WM, Field CM, Mahadevan L, & Weitz DA (2008) A quantitative analysis of contractility in active cytoskeletal protein networks. *Biophysical journal* 94(8):3126-3136.

[19] Geiger B, Spatz JP, & Bershadsky AD (2009) Environmental sensing through focal adhesions. *Nature Reviews Molecular Cell Biology* 10(1):21-33.

[20] Chen CS (2008) Mechanotransduction–a field pulling together? *Journal of Cell Science* 121(20):3285-3292.
[21] Hoffman BD, Grashoff C, & Schwartz MA (2011) Dynamic molecular processes mediate cellular mechanotransduction. *Nature* 475(7356):316-323.
[22] Engler AJ, Sen S, Sweeney HL, & Discher DE (2006) Matrix elasticity directs stem cell lineage specification. *Cell* 126(4):677-689.
[23] Trappmann B, Gautrot JE, Connelly JT, Strange DGT, Li Y, Oyen ML, Stuart MAC, Boehm H, Li B, & Vogel V (2012) Extracellular-matrix tethering regulates stem-cell fate. *Nature materials* 11(7):642-649.
[24] Li YS, Haga JH, & Chien S (2005) Molecular basis of the effects of shear stress on vascular endothelial cells. *J Biomech* 38(10):1949-1971.
[25] Malek AM, Alper SL, & Izumo S (1999) Hemodynamic shear stress and its role in atherosclerosis. *JAMA: the journal of the American Medical Association* 282(21):2035.
[26] Moulding DA, Blundell MP, Spiller DG, White MRH, Cory GO, Calle Y, Kempski H, Sinclair J, Ancliff PJ, & Kinnon C (2007) Unregulated actin polymerization by WASp causes defects of mitosis and cytokinesis in X-linked neutropenia. *The Journal of experimental medicine* 204(9):2213-2224.
[27] Thrasher AJ & Burns SO (2010) WASP: a key immunological multitasker. *Nature Reviews Immunology* 10(3):182-192.
[28] Goldmann WH, Galneder R, Ludwig M, Xu W, Adamson ED, Wang N, & Ezzell RM (1998) Differences in elasticity of vinculin-deficient F9 cells measured by magnetometry and atomic force microscopy. *Experimental cell research* 239(2):235-242.
[29] Lekka M, Laidler P, Gil D, Lekki J, Stachura Z, & Hrynkiewicz A (1999) Elasticity of normal and cancerous human bladder cells studied by scanning force microscopy. *European Biophysics Journal* 28(4):312-316.
[30] Cross SE, Jin YS, Rao J, & Gimzewski JK (2007) Nanomechanical analysis of cells from cancer patients. *Nature nanotechnology* 2(12):780-783.
[31] Iyer S, Gaikwad R, Subba-Rao V, Woodworth C, & Sokolov I (2009) Atomic force microscopy detects differences in the surface brush of normal and cancerous cells. *Nature nanotechnology* 4(6):389-393.
[32] Bausch AR & Kroy K (2006) A bottom-up approach to cell mechanics. *Nature Physics* 2(4):231-238.
[33] Fabry B, Maksym GN, Butler JP, Glogauer M, Navajas D, & Fredberg JJ (2001) Scaling the microrheology of living cells. *Physical review letters* 87(14):148102.
[34] Wang N, Butler JP, & Ingber DE (1993) Mechanotransduction across the cell surface and through the cytoskeleton. *Science* 260(5111):1124-1127.
[35] Bausch AR, Ziemann F, Boulbitch AA, Jacobson K, & Sackmann E (1998) Local measurements of viscoelastic parameters of adherent cell surfaces by magnetic bead microrheometry. *Biophysical journal* 75(4):2038-2049.
[36] Dai J & Sheetz MP (1995) Mechanical properties of neuronal growth cone membranes studied by tether formation with laser optical tweezers. *Biophysical journal* 68(3):988-996.
[37] Yost MJ, Simpson D, Wrona K, Ridley S, Ploehn HJ, Borg TK, & Terracio L (2000) Design and construction of a uniaxial cell stretcher. *American Journal of Physiology-Heart and Circulatory Physiology* 279(6):H3124-H3130.
[38] Ellis E, McKinney J, Willoughby K, Liang S, & Povlishock J (1995) A new model for rapid stretch-induced injury of cells in culture: characterization of the model using astrocytes. *Journal of neurotrauma* 12(3):325-339.
[39] Usami S, Chen HH, Zhao Y, Chien S, & Skalak R (1993) Design and construction of a linear shear stress flow chamber. *Annals of biomedical engineering* 21(1):77-83.
[40] Lu H, Koo LY, Wang WM, Lauffenburger DA, Griffith LG, & Jensen KF (2004) Microfluidic shear devices for quantitative analysis of cell adhesion. *Analytical chemistry* 76(18):5257-5264.
[41] Tan JL, Tien J, Pirone DM, Gray DS, Bhadriraju K, & Chen CS (2003) Cells lying on a bed of microneedles: an approach to isolate mechanical force. *Proceedings of the National Academy of Sciences* 100(4):1484-1489.

[42] Munevar S, Wang Y, & Dembo M (2001) Traction force microscopy of migrating normal and H-ras transformed 3T3 fibroblasts. *Biophysical journal* 80(4):1744-1757.
[43] Wirtz D (2009) Particle-tracking microrheology of living cells: principles and applications. *Annual review of biophysics* 38:301-326.
[44] Lim CT, Zhou EH, & Quek ST (2006) Mechanical models for living cells--a review. *Journal of biomechanics* 39(2):195-216.
[45] Janmey PA & McCulloch CA (2007) Cell mechanics: integrating cell responses to mechanical stimuli. *Annu. Rev. Biomed. Eng.* 9:1-34.
[46] Bao G & Suresh S (2003) Cell and molecular mechanics of biological materials. *Nature materials* 2(11):715-725.
[47] Binnig G, Quate CF, & Gerber C (1986) Atomic force microscope. *Physical review letters* 56(9):930-933.
[48] Morris VJ, Kirby AR, Gunning AP, & World S (1999) *Atomic force microscopy for biologists* (Imperial College Press London).
[49] Kunda P, Rodrigues NTL, Moeendarbary E, Liu T, Ivetic A, Charras G, & Baum B (2011) PP1-Mediated Moesin Dephosphorylation Couples Polar Relaxation to Mitotic Exit. *Current Biology*.
[50] Alessandrini A & Facci P (2005) AFM: a versatile tool in biophysics. *Measurement science and technology* 16:R65.
[51] Moreno-Flores S, Benitez R, Vivanco MM, & Toca-Herrera JL (2010) Stress relaxation and creep on living cells with the atomic force microscope: a means to calculate elastic moduli and viscosities of cell components. *Nanotechnology* 21:445101.
[52] Moreno-Flores S, Benitez R, Vivanco MM, & Toca-Herrera JL (2010) Stress relaxation microscopy: Imaging local stress in cells. *Journal of biomechanics* 43(2):349-354.
[53] Darling EM, Zauscher S, & Guilak F (2006) Viscoelastic properties of zonal articular chondrocytes measured by atomic force microscopy. *Osteoarthritis and Cartilage* 14(6):571-579.
[54] Darling EM, Zauscher S, Block JA, & Guilak F (2007) A thin-layer model for viscoelastic, stress-relaxation testing of cells using atomic force microscopy: do cell properties reflect metastatic potential? *Biophysical journal* 92(5):1784-1791.
[55] Kasza KE, Rowat AC, Liu J, Angelini TE, Brangwynne CP, Koenderink GH, & Weitz DA (2007) The cell as a material. *Curr Opin Cell Biol* 19(1):101-107.
[56] Fletcher DA & Geissler PL (2009) Active biological materials. *Annual review of physical chemistry* 60:469-486.
[57] Julicher F, Kruse K, Prost J, & Joanny JF (2007) Active behavior of the cytoskeleton. *Physics reports* 449(1-3):3-28.
[58] Hoffman BD & Crocker JC (2009) Cell mechanics: dissecting the physical responses of cells to force. *Annual review of biomedical engineering* 11:259-288.
[59] Mitchison TJ, Charras GT, & Mahadevan L (2008) Implications of a poroelastic cytoplasm for the dynamics of animal cell shape. *Seminars in cell & developmental biology*, (Elsevier), pp 215-223.
[60] Kumar S, Maxwell IZ, Heisterkamp A, Polte TR, Lele TP, Salanga M, Mazur E, & Ingber DE (2006) Viscoelastic retraction of single living stress fibers and its impact on cell shape, cytoskeletal organization, and extracellular matrix mechanics. *Biophysical journal* 90(10):3762-3773.
[61] Bursac P, Lenormand G, Fabry B, Oliver M, Weitz DA, Viasnoff V, Butler JP, & Fredberg JJ (2005) Cytoskeletal remodelling and slow dynamics in the living cell. *Nature materials* 4(7):557-561.
[62] Trepat X, Deng L, An SS, Navajas D, Tschumperlin DJ, Gerthoffer WT, Butler JP, & Fredberg JJ (2007) Universal physical responses to stretch in the living cell. *Nature* 447(7144):592-595.
[63] Chen DTN, Wen Q, Janmey PA, Crocker JC, & Yodh AG (2010) Rheology of soft materials. *Condensed Matter Physics* 1.
[64] Kollmannsberger P & Fabry B (2011) Linear and nonlinear rheology of living cells. *Annual Review of Materials Research* 41:75-97.

[65] Trepat X, Lenormand G, & Fredberg JJ (2008) Universality in cell mechanics. *Soft Matter* 4(9):1750-1759.
[66] Ingber DE (2003) Tensegrity I. Cell structure and hierarchical systems biology. *Journal of Cell Science* 116(7):1157.
[67] Sollich P (1998) Rheological constitutive equation for a model of soft glassy materials. *Physical Review E* 58(1):738.
[68] Bausch AR, Möller W, & Sackmann E (1999) Measurement of local viscoelasticity and forces in living cells by magnetic tweezers. *Biophysical journal* 76(1):573-579.
[69] Bausch AR, Hellerer U, Essler M, Aepfelbacher M, & Sackmann E (2001) Rapid stiffening of integrin receptor-actin linkages in endothelial cells stimulated with thrombin: a magnetic bead microrheology study. *Biophysical journal* 80(6):2649-2657.
[70] Dix JA & Verkman AS (2008) Crowding effects on diffusion in solutions and cells. *Annu. Rev. Biophys.* 37:247-263.
[71] Mastro AM, Babich MA, Taylor WD, & Keith AD (1984) Diffusion of a small molecule in the cytoplasm of mammalian cells. *Proceedings of the National Academy of Sciences* 81(11):3414.
[72] Luby-Phelps K, Castle PE, Taylor DL, & Lanni F (1987) Hindered diffusion of inert tracer particles in the cytoplasm of mouse 3T3 cells. *Proceedings of the National Academy of Sciences* 84(14):4910-4913.
[73] Hoffman BD, Massiera G, Van Citters KM, & Crocker JC (2006) The consensus mechanics of cultured mammalian cells. *Proceedings of the National Academy of Sciences* 103(27):10259-10264.
[74] Grünewald K, Medalia O, Gross A, Steven AC, & Baumeister W (2003) Prospects of electron cryotomography to visualize macromolecular complexes inside cellular compartments: implications of crowding* 1. *Biophysical chemistry* 100(1-3):577-591.
[75] Medalia O, Weber I, Frangakis AS, Nicastro D, Gerisch G, & Baumeister W (2002) Macromolecular architecture in eukaryotic cells visualized by cryoelectron tomography. *Science* 298(5596):1209.
[76] Wong IY, Gardel ML, Reichman DR, Weeks ER, Valentine MT, Bausch AR, & Weitz DA (2004) Anomalous diffusion probes microstructure dynamics of entangled F-actin networks. *Physical review letters* 92(17):178101.
[77] Novak IL, Kraikivski P, & Slepchenko BM (2009) Diffusion in cytoplasm: effects of excluded volume due to internal membranes and cytoskeletal structures. *Biophysical journal* 97(3):758-767.
[78] Guigas G, Kalla C, & Weiss M (2007) The degree of macromolecular crowding in the cytoplasm and nucleoplasm of mammalian cells is conserved. *FEBS letters* 581(26):5094-5098.
[79] Alcaraz J, Buscemi L, Grabulosa M, Trepat X, Fabry B, Farré R, & Navajas D (2003) Microrheology of human lung epithelial cells measured by atomic force microscopy. *Biophysical journal* 84(3):2071-2079.
[80] Deng L, Trepat X, Butler JP, Millet E, Morgan KG, Weitz DA, & Fredberg JJ (2006) Fast and slow dynamics of the cytoskeleton. *Nature materials* 5(8):636-640.
[81] Gittes F, Schnurr B, Olmsted PD, MacKintosh FC, & Schmidt CF (1997) Microscopic viscoelasticity: shear moduli of soft materials determined from thermal fluctuations. *Physical review letters* 79(17):3286-3289.
[82] Morse DC (1998) Viscoelasticity of concentrated isotropic solutions of semiflexible polymers. 2. Linear response. *Macromolecules* 31(20):7044-7067.
[83] Gardel M, Valentine M, Crocker JC, Bausch A, & Weitz DA (2003) Microrheology of entangled F-actin solutions. *Physical review letters* 91(15):158302.
[84] Gardel ML, Shin JH, MacKintosh FC, Mahadevan L, Matsudaira P, & Weitz DA (2004) Elastic behavior of cross-linked and bundled actin networks. *Science* 304(5675):1301-1305.
[85] Tharmann R, Claessens M, & Bausch AR (2007) Viscoelasticity of isotropically cross-linked actin networks. *Physical review letters* 98(8):88103.
[86] Storm C, Pastore JJ, MacKintosh FC, Lubensky TC, & Janmey PA (2005) Nonlinear elasticity in biological gels. *Nature* 435(7039):191-194.

[87] Rubenstein M & Colby RH (2003) Polymer Physics. (Oxford Univ. Press: New York).
[88] Wilhelm J & Frey E (2003) Elasticity of stiff polymer networks. *Physical review letters* 91(10):108103.
[89] Head DA, Levine AJ, & MacKintosh FC (2003) Deformation of cross-linked semiflexible polymer networks. *Physical review letters* 91(10):108102.
[90] Levine AJ & Lubensky T (2001) Response function of a sphere in a viscoelastic two-fluid medium. *Physical Review E* 63(4):041510.
[91] De Gennes PG, Pincus P, Velasco R, & Brochard F (1976) Remarks on polyelectrolyte conformation. *Journal de physique* 37(12):1461-1473.
[92] Xu K, Babcock HP, & Zhuang X (2012) Dual-objective STORM reveals three-dimensional filament organization in the actin cytoskeleton. *Nature Methods*.
[93] Gardel M, Nakamura F, Hartwig J, Crocker J, Stossel T, & Weitz D (2006) Prestressed F-actin networks cross-linked by hinged filamins replicate mechanical properties of cells. *Proceedings of the National Academy of Sciences of the United States of America* 103(6):1762-1767.
[94] Gardel ML, Nakamura F, Hartwig J, Crocker JC, Stossel TP, & Weitz DA (2006) Stress-dependent elasticity of composite actin networks as a model for cell behavior. *Physical review letters* 96(8):88102.
[95] Ingber DE (1993) Cellular tensegrity: defining new rules of biological design that govern the cytoskeleton. *Journal of Cell Science* 104:613-613.
[96] Joanny JF & Prost J (2009) Active gels as a description of the actin-myosin cytoskeleton. *HFSP journal* 3(2):94-104.
[97] Liverpool T & Marchetti MC (2007) Bridging the microscopic and the hydrodynamic in active filament solutions. *EPL (Europhysics Letters)* 69(5):846.
[98] Liverpool T & Marchetti MC (2006) Rheology of active filament solutions. *Physical review letters* 97(26):268101.
[99] Ball P (2008) Water as an active constituent in cell biology. *Chemical reviews* 108(1):74-108.
[100] Charras GT, Yarrow JC, Horton MA, Mahadevan L, & Mitchison TJ (2005) Non-equilibration of hydrostatic pressure in blebbing cells. *Nature* 435(7040):365-369.
[101] Charras GT, Mitchison TJ, & Mahadevan L (2009) Animal cell hydraulics. *Journal of Cell Science* 122(18):3233-3241.
[102] Charras GT, Coughlin M, Mitchison TJ, & Mahadevan L (2008) Life and times of a cellular bleb. *Biophysical journal* 94(5):1836-1853.
[103] Rosenbluth MJ, Crow A, Shaevitz JW, & Fletcher DA (2008) Slow stress propagation in adherent cells. *Biophysical journal* 95(12):6052-6059.
[104] Zhang W & Robinson DN (2005) Balance of actively generated contractile and resistive forces controls cytokinesis dynamics. *Proceedings of the National Academy of Sciences of the United States of America* 102(20):7186.
[105] Dembo M & Harlow F (1986) Cell motion, contractile networks, and the physics of interpenetrating reactive flow. *Biophysical journal* 50(1):109-121.
[106] Wang H (2000) *Theory of linear poroelasticity: with applications to geomechanics and hydrogeology* (Princeton Univ Pr).
[107] Charras G & Paluch E (2008) Blebs lead the way: how to migrate without lamellipodia. *Nature Reviews Molecular Cell Biology* 9(9):730-736.
[108] Lai WM, Rubin D, & Krempl E (2009) *Introduction to continuum mechanics* (Butterworth-Heinemann).
[109] Landau L & Lifshitz E (1959) Theory of elasticity. *Pergamon Press Ltd., Oxford, U.K* 30–36.
[110] Johnson KL (1982) One hundred years of Hertz contact. *ARCHIVE: Proceedings of the Institution of Mechanical Engineers 1847-1982 (vols 1-196)* 196(1982):363-378.
[111] Christensen RM & Freund LB (1971) Theory of viscoelasticity. *Journal of Applied Mechanics* 38:720.
[112] Fabry B, Maksym GN, Butler JP, Glogauer M, Navajas D, Taback NA, Millet EJ, & Fredberg JJ (2003) Time scale and other invariants of integrative mechanical behavior in living cells. *Physical Review E* 68(4):041914.

[113] Heymans N (2004) Fractional calculus description of non-linear viscoelastic behaviour of polymers. *Nonlinear dynamics* 38(1):221-231.
[114] Mainardi F (2012) Fractional calculus: some basic problems in continuum and statistical mechanics. *Arxiv preprint arXiv:1201.0863*.
[115] Detournay E & Cheng AHD (1993) Fundamentals of poroelasticity. (Pergamon).
[116] Biot MA (1941) General theory of three-dimensional consolidation. *Journal of applied physics* 12(2):155-164.
[117] Mow VC, Kuei SC, Lai WM, & Armstrong CG (1980) Biphasic creep and stress relaxation of articular cartilage in compression: theory and experiments. *Journal of biomechanical engineering* 102:73.
[118] Scheidegger AE (1958) The physics of flow through porous media. *Soil Science* 86(6):355.
[119] Yoon J, Cai S, Suo Z, & Hayward RC (2010) Poroelastic swelling kinetics of thin hydrogel layers: comparison of theory and experiment. *Soft Matter*.
[120] Hu Y, Zhao X, Vlassak JJ, & Suo Z (2010) Using indentation to characterize the poroelasticity of gels. *Applied Physics Letters* 96:121904.
[121] Chan EP, Hu Y, Johnson PM, Suo Z, & Stafford CM (2012) Spherical indentation testing of poroelastic relaxations in thin hydrogel layers. *Soft Matter* 8(5):1492-1498.
[122] Ory DS, Neugeboren BA, & Mulligan RC (1996) A stable human-derived packaging cell line for production of high titer retrovirus/vesicular stomatitis virus G pseudotypes. *Proceedings of the National Academy of Sciences of the United States of America* 93(21):11400.
[123] Riedl J, Crevenna AH, Kessenbrock K, Yu JH, Neukirchen D, Bista M, Bradke F, Jenne D, Holak TA, & Werb Z (2008) Lifeact: a versatile marker to visualize F-actin. *Nature Methods* 5(7):605-607.
[124] Bancaud A, Huet S, Daigle N, Mozziconacci J, Beaudouin J, & Ellenberg J (2009) Molecular crowding affects diffusion and binding of nuclear proteins in heterochromatin and reveals the fractal organization of chromatin. *The EMBO journal* 28(24):3785-3798.
[125] Zhou EH, Trepat X, Park CY, Lenormand G, Oliver MN, Mijailovich SM, Hardin C, Weitz DA, Butler JP, & Fredberg JJ (2009) Universal behavior of the osmotically compressed cell and its analogy to the colloidal glass transition. *Proceedings of the National Academy of Sciences* 106(26):10632-10637.
[126] Hoffmann EK, Lambert IH, & Pedersen SF (2009) Physiology of cell volume regulation in vertebrates. *Physiological reviews* 89(1):193-277.
[127] Demaison C, Parsley K, Brouns G, Scherr M, Battmer K, Kinnon C, Grez M, & Thrasher AJ (2002) High-level transduction and gene expression in hematopoietic repopulating cells using a human imunodeficiency virus type 1-based lentiviral vector containing an internal spleen focus forming virus promoter. *Human gene therapy* 13(7):803-813.
[128] Zheng Y, Wong ML, Alberts B, & Mitchison T (1995) Nucleation of microtubule assembly by a gamma-tubulin-containing ring complex. *Nature* 378:578-583.
[129] Keppler A & Ellenberg J (2009) Chromophore-assisted laser inactivation of -and -tubulin SNAP-tag fusion proteins inside living cells. *ACS Chemical Biology* 4(2):127-138.
[130] Werner NS, Windoffer R, Strnad P, Grund C, Leube RE, & Magin TM (2004) Epidermolysis bullosa simplex-type mutations alter the dynamics of the keratin cytoskeleton and reveal a contribution of actin to the transport of keratin subunits. *Molecular biology of the cell* 15(3):990-1002.
[131] Long R, Hall MS, Wu M, & Hui CY (2011) Effects of gel thickness on microscopic indentation measurements of gel modulus. *Biophysical journal* 101(3):643-650.
[132] Gavara N & Chadwick RS (2012) Determination of the elastic moduli of thin samples and adherent cells using conical atomic force microscope tips. *Nature nanotechnology* 7(11):733-736.
[133] Lin DC, Dimitriadis EK, & Horkay F (2007) Robust strategies for automated AFM force curve analysis—I. Non-adhesive indentation of soft, inhomogeneous materials. *Journal of biomechanical engineering* 129:430.
[134] Charras GT, Hu CK, Coughlin M, & Mitchison TJ (2006) Reassembly of contractile actin cortex in cell blebs. *The Journal of cell biology* 175(3):477-490.

[135] Hui CY, Lin YY, Chuang FC, Shull KR, & Lin WC (2006) A contact mechanics method for characterizing the elastic properties and permeability of gels. *Journal of Polymer Science Part B: Polymer Physics* 44(2):359-370.
[136] Hu Y, Chen X, Whitesides GM, Vlassak JJ, & Suo Z (2011) Indentation of polydimethylsiloxane submerged in organic solvents. *Journal of Materials Research* 26(06):785-795.
[137] Kalcioglu ZI, Mahmoodian R, Hu Y, Suo Z, & Van Vliet KJ (2012) From macro-to microscale poroelastic characterization of polymeric hydrogels via indentation. *Soft Matter* 8:3393-3398.
[138] Speidel M, Jonáš A, & Florin EL (2003) Three-dimensional tracking of fluorescent nanoparticles with subnanometer precision by use of off-focus imaging. *Optics letters* 28(2):69-71.
[139] Axelrod D, Koppel D, Schlessinger J, Elson E, & Webb W (1976) Mobility measurement by analysis of fluorescence photobleaching recovery kinetics. *Biophysical journal* 16(9):1055-1069.
[140] Soumpasis D (1983) Theoretical analysis of fluorescence photobleaching recovery experiments. *Biophysical journal* 41(1):95-97.
[141] Kang M, Day CA, Drake K, Kenworthy AK, & DiBenedetto E (2009) A generalization of theory for two-dimensional fluorescence recovery after photobleaching applicable to confocal laser scanning microscopes. *Biophysical journal* 97(5):1501-1511.
[142] Chan EP, Deeyaa B, Johnson PM, & Stafford CM (2012) Poroelastic relaxation of polymer-loaded hydrogels. *Soft Matter* 8(31):8234-8240.
[143] Fredberg JJ & Stamenovic D (1989) On the imperfect elasticity of lung tissue. *Journal of applied physiology* 67(6):2408-2419.
[144] Smith BA, Tolloczko B, Martin JG, & Grütter P (2005) Probing the viscoelastic behavior of cultured airway smooth muscle cells with atomic force microscopy: stiffening induced by contractile agonist. *Biophysical journal* 88(4):2994-3007.
[145] Okajima T, Tanaka M, Tsukiyama S, Kadowaki T, Yamamoto S, Shimomura M, & Tokumoto H (2007) Stress relaxation of HepG2 cells measured by atomic force microscopy. *Nanotechnology* 18:084010.
[146] Wottawah F, Schinkinger S, Lincoln B, Ebert S, Müller K, Sauer F, Travis K, & Guck J (2005) Characterizing single suspended cells by optorheology. *Acta biomaterialia* 1(3):263-271.
[147] Desprat N, Richert A, Simeon J, & Asnacios A (2005) Creep function of a single living cell. *Biophysical journal* 88(3):2224-2233.
[148] Wottawah F, Schinkinger S, Lincoln B, Ananthakrishnan R, Romeyke M, Guck J, & Käs J (2005) Optical rheology of biological cells. *Physical review letters* 94(9):98103.
[149] Lenormand G, Millet E, Fabry B, Butler JP, & Fredberg JJ (2004) Linearity and time-scale invariance of the creep function in living cells. *Journal of The Royal Society Interface* 1(1):91-97.
[150] Keren K, Yam PT, Kinkhabwala A, Mogilner A, & Theriot JA (2009) Intracellular fluid flow in rapidly moving cells. *Nature cell biology* 11(10):1219-1224.
[151] Moreno-Flores S, Benitez R, & Toca-Herrera JL (2010) Stress relaxation and creep on living cells with the atomic force microscope: a means to calculate elastic moduli and viscosities of cell components. *Nanotechnology* 21:445101.
[152] Skotheim J & Mahadevan L (2004) Dynamics of poroelastic filaments. *Proceedings of the Royal Society of London. Series A: Mathematical, Physical and Engineering Sciences* 460(2047):1995-2020.
[153] Avril S, Schneider F, Boissier C, & Li ZY (2011) In vivo velocity vector imaging and time-resolved strain rate measurements in the wall of blood vessels using MRI. *Journal of biomechanics* 44(5):979-983.
[154] Li P, Liu A, Shi L, Yin X, Rugonyi S, & Wang RK (2011) Assessment of strain and strain rate in embryonic chick heart in vivo using tissue Doppler optical coherence tomography. *Physics in medicine and biology* 56:7081–7092.
[155] Perlman CE & Bhattacharya J (2007) Alveolar expansion imaged by optical sectioning microscopy. *Journal of applied physiology* 103(3):1037-1044.

[156] Ibata K, Takimoto S, Morisaku T, Miyawaki A, & Yasui M (2011) Analysis of Aquaporin-Mediated Diffusional Water Permeability by Coherent Anti-Stokes Raman Scattering Microscopy. *Biophysical journal* 101(9):2277-2283.
[157] Fels J, Orlov SN, & Grygorczyk R (2009) The hydrogel nature of mammalian cytoplasm contributes to osmosensing and extracellular pH sensing. *Biophysical journal* 96(10):4276-4285.
[158] Sehy JV, Banks AA, Ackerman JJH, & Neil JJ (2002) Importance of intracellular water apparent diffusion to the measurement of membrane permeability. *Biophysical journal* 83(5):2856-2863.
[159] Potma EO, De Boeij WP, van Haastert PJM, & Wiersma DA (2001) Real-time visualization of intracellular hydrodynamics in single living cells. *Proceedings of the National Academy of Sciences* 98(4):1577.
[160] Lang F, Busch GL, Ritter M, Volkl H, Waldegger S, Gulbins E, & Haussinger D (1998) Functional significance of cell volume regulatory mechanisms. *Physiological reviews* 78(1):247.
[161] Derfus AM, Chan WCW, & Bhatia SN (2004) Intracellular delivery of quantum dots for live cell labeling and organelle tracking. *Advanced Materials* 16(12):961-966.
[162] Swaminathan R, Bicknese S, Periasamy N, & Verkman AS (1996) Cytoplasmic viscosity near the cell plasma membrane: translational diffusion of a small fluorescent solute measured by total internal reflection-fluorescence photobleaching recovery. *Biophysical Journal* 71(2):1140-1151.
[163] Swaminathan R, Hoang CP, & Verkman A (1997) Photobleaching recovery and anisotropy decay of green fluorescent protein GFP-S65T in solution and cells: cytoplasmic viscosity probed by green fluorescent protein translational and rotational diffusion. *Biophysical journal* 72(4):1900-1907.
[164] Kao HP, Abney JR, & Verkman AS (1993) Determinants of the translational mobility of a small solute in cell cytoplasm. *The Journal of cell biology* 120(1):175-184.
[165] Phair RD & Misteli T (2000) High mobility of proteins in the mammalian cell nucleus. *Nature* 404(6778):604-608.
[166] Phillips RJ (2000) A hydrodynamic model for hindered diffusion of proteins and micelles in hydrogels. *Biophysical Journal* 79(6):3350.
[167] Happel J & Brenner H (1983) *Low Reynolds number hydrodynamics: with special applications to particulate media* (Springer).
[168] Persson E & Halle B (2008) Cell water dynamics on multiple time scales. *Proceedings of the National Academy of Sciences* 105(17):6266.
[169] Rotsch C & Radmacher M (2000) Drug-induced changes of cytoskeletal structure and mechanics in fibroblasts: an atomic force microscopy study. *Biophysical journal* 78(1):520-535.
[170] Rotsch C, Jacobson K, & Radmacher M (1999) Dimensional and mechanical dynamics of active and stable edges in motile fibroblasts investigated by using atomic force microscopy. *Proceedings of the National Academy of Sciences of the United States of America* 96(3):921.
[171] Wakatsuki T, Schwab B, Thompson NC, & Elson EL (2001) Effects of cytochalasin D and latrunculin B on mechanical properties of cells. *Journal of cell science* 114(Pt 5):1025.
[172] Low SH, Mukhina S, Srinivas V, Ng CZ, & Murata-Hori M (2010) Domain analysis of α-actinin reveals new aspects of its association with F-actin during cytokinesis. *Experimental cell research* 316(12):1925-1934.
[173] Shu HB & Joshi HC (1995) Gamma-tubulin can both nucleate microtubule assembly and self-assemble into novel tubular structures in mammalian cells. *The Journal of cell biology*:1137-1147.
[174] Spagnoli C, Beyder A, Besch S, & Sachs F (2008) Atomic force microscopy analysis of cell volume regulation. *Physical Review E* 78(3):31916.
[175] Albrecht-Buehler G & Bushnell A (1982) Reversible compression of cytoplasm. *Experimental cell research* 140(1):173-189.
[176] Mizuno D, Tardin C, Schmidt CF, & MacKintosh FC (2007) Nonequilibrium mechanics of active cytoskeletal networks. *Science* 315(5810):370-373.

[177] Stewart MP, Helenius J, Toyoda Y, Ramanathan SP, Muller DJ, & Hyman AA (2011) Hydrostatic pressure and the actomyosin cortex drive mitotic cell rounding. *Nature* 469(7329):226-230.
[178] Stamenovic D, Rosenblatt N, Montoya-Zavala M, Matthews BD, Hu S, Suki B, Wang N, & Ingber DE (2007) Rheological behavior of living cells is timescale-dependent. *Biophysical journal* 93(8):L39-L41.
[179] Van Citters KM, Hoffman BD, Massiera G, & Crocker JC (2006) The role of F-actin and myosin in epithelial cell rheology. *Biophysical journal* 91(10):3946-3956.
[180] Mukhina S, Wang Y, & Murata-Hori M (2007) [alpha]-Actinin Is Required for Tightly Regulated Remodeling of the Actin Cortical Network during Cytokinesis. *Developmental cell* 13(4):554-565.
[181] Ando T & Skolnick J (2010) Crowding and hydrodynamic interactions likely dominate in vivo macromolecular motion. *Proceedings of the National Academy of Sciences* 107(43):18457-18462.
[182] Gittes F, Mickey B, Nettleton J, & Howard J (1993) Flexural rigidity of microtubules and actin filaments measured from thermal fluctuations in shape. *The Journal of cell biology* 120(4):923-934.
[183] Zicha D, Dobbie IM, Holt MR, Monypenny J, Soong DYH, Gray C, & Dunn GA (2003) Rapid actin transport during cell protrusion. *Science* 300(5616):142-145.
[184] Pollard TD & Borisy GG (2003) Cellular motility driven by assembly and disassembly of actin filaments. *Cell* 112(4):453-465.
[185] De Gennes PG (1976) Dynamics of entangled polymer solutions (I&II). *Macromolecules* 9(4):587-598.
[186] Hawkins RJ, Piel M, Faure-Andre G, Lennon-Dumenil A, Joanny J, Prost J, & Voituriez R (2009) Pushing off the walls: a mechanism of cell motility in confinement. *Physical review letters* 102(5):58103.